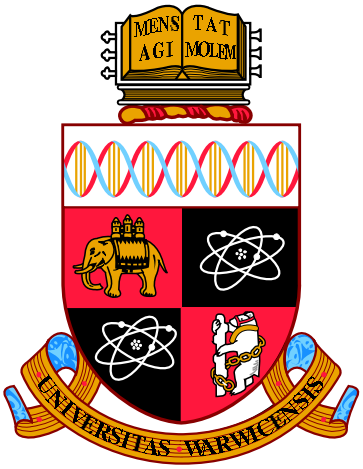

A measurement of the muon antineutrino inclusive charged-current cross-section using the T2K near detector

by

Callum Lister

Thesis

Submitted to the University of Warwick

for the degree of

Doctor of Philosophy

Department of Physics

July 2015

THE UNIVERSITY OF WARWICK

Contents

List of Tables

List of Figures

Acknowledgments

There are many people I would like to thank for the support I have received during my PhD. Firstly, I must thank my supervisors Dr Steven Boyd and Dr Gary Barker for giving me the opportunity to study for my doctorate at Warwick, and for their continued support throughout that period.

I would also like to thank the colleagues who supported me, both at Warwick and in Japan. These include Drs Andrew Bennieston, David Hadley, Phillip Litchfield, Daniel Scully and Leigh Whitehead.

Finally, I would like to thank all those not mentioned that I have worked closely with over the last four years.

Declarations

T2K is an experiment involving collaborators from across the world and as such the work presented in this thesis draws heavily on work done by a number of people. This declaration outlines the work undertaken by the author personally, and credits the work performed by colleagues. The material presented in this thesis has not been published or submitted for examination at any other institute.

Chapters 2 and 3 give an overview of neutrino physics and detail the T2K experiment and its role in this area. Information sources include published papers and theses and all sources are referenced appropriately.

Chapter 4 outlines the ND280 ECal at the CERN T9 testbeam. The collection of data at the testbeam site at CERN was conducted prior to the author joining the collaboration. However, calibration of the data collected for use in a second generation ECal PID algorithm was done entirely by the author. Performance evaluations and data/simulation comparisons were also original work, except for the energy resolution comparison which has been appropriately credited.

Chapters 5 and 6 are primarily the work of the author. The data used in the analyses were taken by the T2K ND280 and were processed using software produced with contributions from a number of members of the collaboration. Some intermediary studies from collaborators are used in obtaining the final results, and these are referenced appropriately.

Abstract

The T2K (Tokai-to-Kamioka) experiment is a long baseline neutrino oscillation experiment built, primarily, to measure the neutrino mixing angle θ_{13}. To determine this parameter with minimal uncertainty requires a good understanding of the initial neutrino flux in the beam and precise measurements of neutrino interactions with matter. For this reason, T2K employs a near detector placed 280 m downstream of the neutrino production point, the ND280.

Using data taken by the ND280 between November 2010 and April 2013 (5.73×10^{20} protons on target), a flux-integrated muon antineutrino charged-current inclusive cross-section measurement per nucleon using the carbon target of the ND280 FGD1 is reported, including a description of the event selection and the systematic uncertainty evaluation. The final result is:

$$\langle \sigma_{\bar{\nu}_\mu} \rangle_\Phi = (2.72 \pm 0.03(\text{stat.})^{+0.28}_{-0.34}(\text{flux}) \pm 0.14(\text{int.}) \pm 0.14(\text{det.})) \times 10^{-39} \frac{\text{cm}^2}{\text{nucleon}}$$

at a mean muon antineutrino energy of 1 GeV.

The uncertainty on this measurement is dominated by neutrino flux uncertainties. A possible method of improving the precision with which the flux is known is presented, which indicates that at the end of the expected T2K data-taking period, this uncertainty can be reduced from 12.4% to 5.8%.

Abbreviations

ADC Analogue-to-digital converter

CC Charged-current

CCQE Charged-current quasi-elastic

CVC Conserved vector current

ECal Electromagnetic calorimeter

EM Electromagnetic

FGD Fine-grained detector

FV Fiducial volume

NH Normal hierarchy

IH Inverse hierarchy

INGRID Interactive neutrino grid; the on-axis near detector

LArTPC Liquid argon time projection chamber

MEU MIP-equivalent units

MIP Minimally ionising particle

MPPC Multi-pixel photon counter

MPV Most probable value

MSW effect Mikheyev-Smirnov-Wolfenstein effect of oscillations in matter

MVA Multivariate analysis

NC Neutral-current

ND280 Near detector at 280m from neutrino source; the off-axis near detector

OOFV Out-of-fiducial-volume

PEU Photon equivalent units

P0D π^0 detector

PMNS Pontecorvo-Maki-Nakagawa-Sakata (matrix)

PID Particle identification

PMT Photo-multiplier tube

POT Protons on target

RFG Relativistic Fermi Gas

SF Spectral Function

SMRD Side muon range detector

SNO Sudbury Neutrino Observatory

TPC Time projection chamber

TOF Time-of-flight

WLS Wavelength-shifting

Chapter 1

Introduction

Neutrino physics has developed enormously over the course of the last century. The elusive particles were postulated to exist in 1930, and since then their properties have been studied in depth by many experiments across the world.

Meanwhile, the Large Hadron Collider (LHC) at CERN has, in recent years, been verifying more and more fully the Standard Model of Particle Physics, culminating in the discovery of the Higgs boson in 2012. But neutrino physicists had already revealed physics not covered by the Standard Model. The mixing of neutrino flavours is an important discovery that may explain one of the biggest mysteries in particle physics today. The phenomenon of $\mathcal{CP}$ violation, which may account for the matter-antimatter asymmetry in the observable universe, has already been confirmed in the quark sector at the LHC. However, additional physics beyond the Standard Model is required to explain the observed asymmetry. $\mathcal{CP}$ violation in the mixing of neutrinos is an attractive candidate.

Neutrino oscillation experiments can probe $\mathcal{CP}$ violation in the lepton sector by looking at the asymmetry between neutrino and antineutrino oscillations, but oscillation measurements cannot be made without precise knowledge of the interactions through which their characteristics can be studied. Although this has sparked a renewed interest in studying neutrino interactions, antineutrino cross-sections particularly are still especially poorly constrained. The aim of this thesis is to contribute to the progress being made in understanding these cross-sections by presenting a measurement of the flux-integrated muon antineutrino charged-current inclusive cross-section at a mean energy of 1 GeV, where currently no published measurements exist.

A brief history of neutrino physics, its theoretical basis within (and beyond) the Standard Model, and the current state and future plans of this field will be described in Chapter 2. The T2K experiment, built to investigate the phenomenon of neutrino oscillations, will be described in detail in Chapter 3. In Chapter 4, the performance of the downstream electromagnetic calorimeter of the T2K off-axis near detector, which was taken to a testbeam site to be analysed, will be described, before reporting the main analysis in Chapter 5, which makes use of this subdetector. Finally, a study which investigates a possible future improvement to this measurement will be detailed in Chapter 6.

Chapter 2

Neutrino Physics

2.1 Neutrinos in the Standard Model of particle physics

The Standard Model of Particle Physics describes how the universe is governed through the interaction of fields and their particle manifestations. The model includes descriptions of the electromagnetic (EM), weak and strong forces[1] in terms of the exchange of bosons, along with 13 other particles: six quarks, six leptons and the Higgs boson, as shown in Figure 2.1. The Standard Model is extremely well verified; indeed, even more so since the discovery of the Higgs boson in 2012 [1][2].

As carriers of the colour charge, the six quarks experience the strong interaction. They also carry weak isospin and electric charge, and are divided into three generations of an up- and down-type quark, such that each generation differs only in the mass of its particles. Each up-type quark carries an electric charge of $+\frac{2}{3}$, a down-type quark carrying $-\frac{1}{3}$.

The remaining six fermions, the leptons, are also divided into three generations that differ only in the mass of their contained particles. As opposed to the quarks, the leptons do not experience the strong force, but do carry weak isospin, and a subset also carry electric charge: the down-type particles carry the electric charge of -1; the up-type particles are the electrically neutral neutrinos.

[1] The extremely weak gravitational force is not included in this model. Inclusion of gravity in a quantum field theory is a major area of research in theoretical physics.

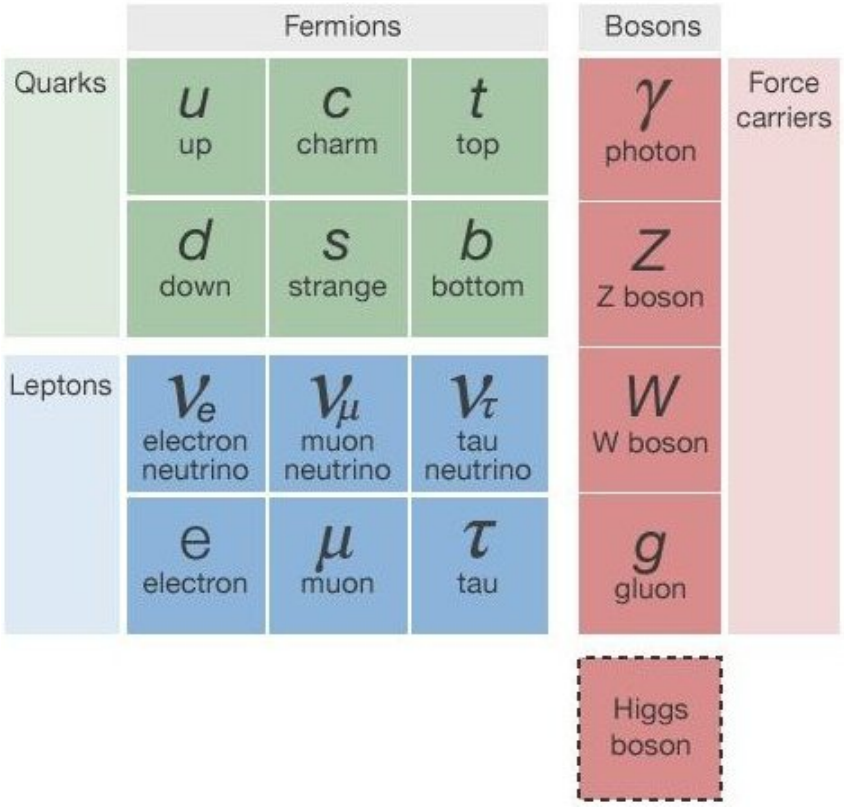

Figure 2.1: Particle content of the Standard Model. Image from [3].

2.2 History

2.2.1 The discovery of the neutrino

After the discovery of radioactivity in the late 19th century, the phenomenon was investigated in depth. The β-decay experiments of James Chadwick in 1914 gave some surprising results: the total energy of the final state particles known at the time, the proton and electron, was not equal to the energy of the decaying neutron, and in fact differed from experiment to experiment [4]. Either energy was not conserved on an event-by-event basis at the particle level, a possibility proposed by Niels Bohr, or there existed another particle that had to be electrically neutral and highly penetrating to carry off the excess energy unseen.

Wolfgang Pauli opted for the latter solution in his open letter of 1930 [5]. At the time, he named the undetected particle the neutron, but it is known today as the neutrino (*little neutral one*).

The existence of the neutrino was confirmed 26 years later at an experiment in South Carolina. An underground detector was built, which provided 12 m of shielding from cosmic rays, to detect the large flux of neutrinos from the Savannah River nuclear reactor. As we know today, the neutrino interaction cross-section is extremely small.[2] This meant that even with these advantages the signal rate was tiny, and the background rate was four times higher. The experiment was looking for a signal originating from the inverse β-decay reaction within the water target of the detector, producing a positron and a neutron. The annihilation of the positron would produce a back-to-back pair of photons, and the absorption of the neutron by cadmium chloride dissolved in the water would yield a further photon within approximately 5×10^{-6} s. With three tanks of liquid scintillator interleaved with two tanks of water, photo-multiplier tubes could be used to detect the flashes of visible light from these photons. The experiment had many challenges, but in 1956 Cowan and Reines had sufficient evidence for the existence of the neutrino [7], with an interaction cross-section measured to be in reasonable agreement with the theoretical limit set by Bethe and Peierls in 1934 [6]; a discovery that earned Reines a Nobel Prize in 1995.[3]

In 1962, the discovery that more than one flavour of neutrino probably existed was made [8]. An experiment at the Brookhaven National Laboratory in the U.S.A. was studying the interactions of neutrinos produced in the decay of charged pions,

$$\pi^{\pm} \rightarrow \mu^{\pm} + (\nu/\bar{\nu}). \tag{2.1}$$

It was noted that the interactions always produced muons and hence the neutrinos were "very likely different from the neutrinos involved in β-decay" [8]. This was the discovery of the muon neutrino.

Finally, the tau neutrino was discovered. Although its existence was assumed since the discovery of the tau lepton in 1975 [9], it is interesting to note that the tau neutrino was not formally discovered until 2000, in a study conducted by the DONuT[4] collaboration [10].

[2] As was indicated by calculations by H. Bethe and R. Peierls in 1934 [6].
[3] Cowan, unfortunately, had died in 1974.
[4] Direct Observation of the Nu Tau.

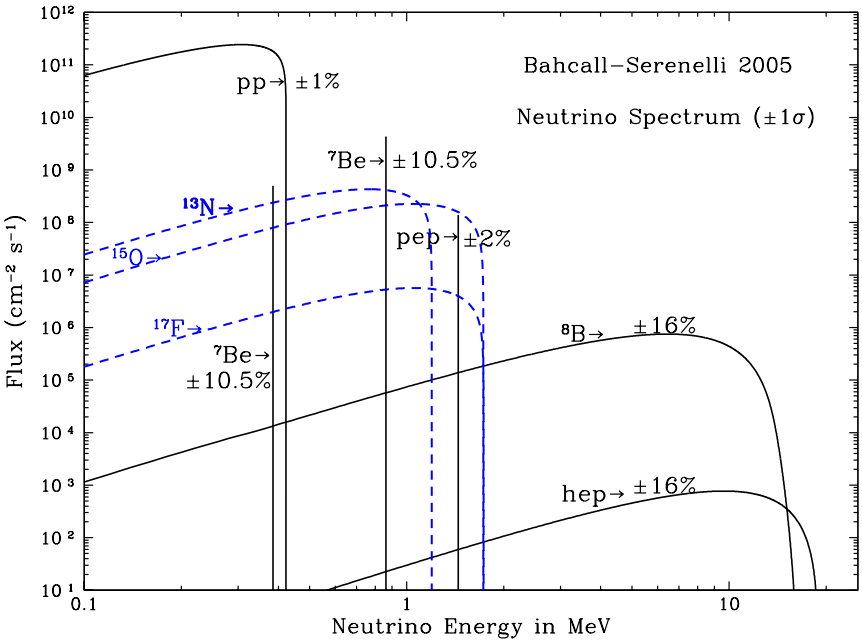

Figure 2.2: Neutrino flux as a function of energy, predicted by the standard solar model of neutrinos. Solid black lines show the flux of neutrinos originating from the proton-proton chain reaction. Dashed blue lines indicate that the neutrinos originate from a branch of the carbon-nitrogen-oxygen cycle. Image reproduced from [11].

2.2.2 The discovery of neutrino oscillations

The solar neutrino problem

In 1965, Raymond Davis Jr had begun running an experiment in the Homestake gold mine, South Dakota. The Standard Solar Model of the time [12] predicted a large flux of electron neutrinos originating from fusion processes in the Sun (Figure 2.2), and the purpose of the Homestake experiment was to verify this model. It ran continuously for 24 years, during which time the average capture rate of solar neutrinos was compared to that predicted by the Standard Solar Model. The results were not as expected: the theoretical prediction gave a capture rate of 8.1 ± 1.2 SNU,[5] but Davis' result was 2.56 ± 0.25 SNU, more than a factor of three lower. This was the genesis of the solar neutrino problem.

[5]The SNU, or Solar Neutrino Unit, is defined as 10^{-36} neutrino interactions per target atom per second.

The Homestake experiment's method was simple. The detector initially consisted of tetrachloroethylene such that the target nucleus was Chlorine-37, and Argon-37 atoms would be produced after the capture of electron neutrinos:

$$\nu_e + {}^{37}\mathrm{Cl} \rightarrow e^- + {}^{37}\mathrm{Ar}. \tag{2.2}$$

The argon was periodically extracted from the detector and the number of radioactive Argon-37 atoms measured. From this, a measurement could be made of the number of electron neutrinos that had interacted with the target [13]. The downside of the method was that no directional information about the neutrinos being detected could be given, and due to this and the surprising discrepancy between theory and experiment, many people believed that Davis' group were not detecting solar neutrinos at all.

This doubt was removed in 1989, when the Kamiokande-II collaboration published their solar neutrino results using a 2140 ton ring imaging Čerenkov neutrino detector situated in the Mozumi mine in Japan [14]. The main method used in this experiment to infer the presence of an incoming electron neutrino was to detect final state electrons emitted from the water target after a weak interaction scattering process. The great advantage of this detection method is that in looking at the final state electron one can discern the general direction of the incoming neutrino. Even with scattering effects, the precision to which this direction could be discerned was enough to show that the neutrinos were indeed coming from the Sun. Kamiokande-II also measured the electron neutrino capture rate; their result was approximately half that expected from theory [14].

The Sudbury Neutrino Observatory (SNO), situated in Creighton Mine, Ontario, solved the solar neutrino problem in 2002, by providing direct evidence for the oscillation of neutrinos travelling from the Sun [15]. Another Čerenkov detector, the success of this experiment was in its use of heavy water rather than natural water as used in Kamiokande-II, allowing sensitivity to all neutrino flavours.

The energy spectrum of solar neutrinos goes up to approximately 20 MeV (Figure 2.2), which is high enough to produce electrons in the charged-current (CC) weak interaction, but not high enough to produce muons or tau leptons. This meant that only electron neutrinos could be detected, so another detection method having

a lower energy threshold was required. Deuterium, contained in heavy water, has a binding energy of approximately 2 MeV. Any incoming neutrino of sufficient energy can break this nucleus apart, and so there was no longer a reliance on CC interactions; by measuring the final state neutron, SNO could measure the total incoming neutrino flux from the Sun. SNO also measured the individual electron neutrino flux by looking at electrons produced in the pure CC weak interaction:

$$\nu_e + d \rightarrow p + p + e^-. \tag{2.3}$$

By comparing the two measurements the combined muon and tau neutrino flux could also be inferred.

The results from SNO gave the combined muon and tau neutrino flux as being twice as large as the flux of the electron neutrino, but the total flux from all three neutrino types as consistent with the Standard Solar Model. This result, along with the known fact that the Sun only produces neutrinos of the electron flavour, implied that two thirds of the solar neutrinos had changed in flavour, or oscillated, prior to being detected on Earth.

The atmospheric neutrino anomaly

Atmospheric neutrinos are produced primarily in the decay of pions coming from the interaction of cosmic rays in the Earth's atmosphere. Charged pions almost always[6] decay to a muon and an accompanying muon (anti-)neutrino, with the muon subsequently decaying as follows:

$$\pi^+ \rightarrow \mu^+ + \nu_\mu, \qquad \mu^+ \rightarrow e^+ + \nu_e + \bar{\nu}_\mu, \tag{2.4}$$

$$\pi^- \rightarrow \mu^- + \bar{\nu}_\mu, \qquad \mu^- \rightarrow e^- + \bar{\nu}_e + \nu_\mu. \tag{2.5}$$

Feynman diagrams for the case shown in (2.4) are given in Figure 2.3.

The ratio of the flux of muon neutrinos to electron neutrinos is therefore predicted to be approximately 2:1, but in 1988 Kamiokande-II measured a value of approximately

[6] With a branching ratio of 99.99%; see Table 3.2.

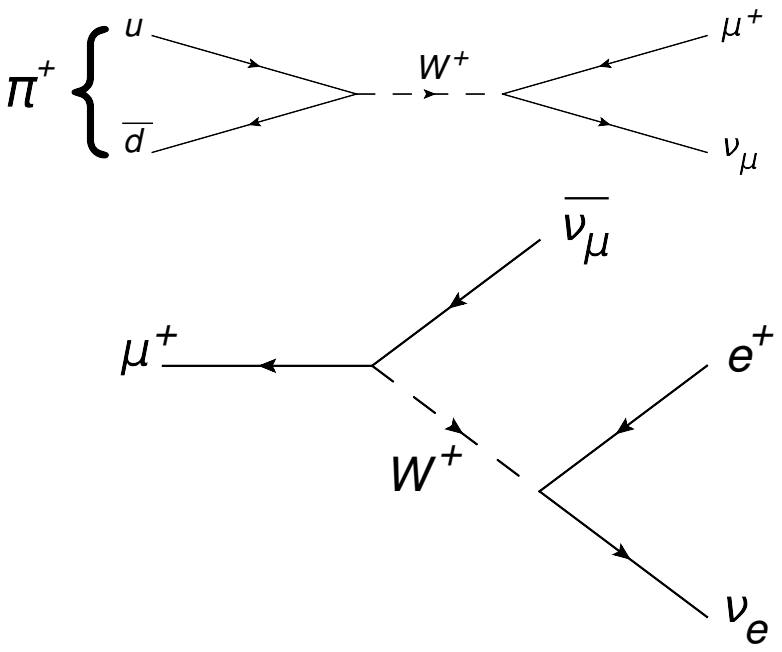

Figure 2.3: Feynman diagrams depicting (top) positive pion decay, and (bottom) the subsequent decay of the positive muon.

two thirds of that expected [16]. At a similar time and over the following years, other experiments measured values consistent with this [17] [18].

Looking at the direction from which the neutrinos were originating provided useful information that helped lead to the solution of the atmospheric neutrino anomaly. As, for all practical purposes, neutrinos only interact via the weak nuclear force, they are very unlikely to interact with Earth; trillions pass right through it every second, and so whether the incoming neutrino was coming through the Earth into the detector from below, or straight down from the atmosphere above the detector, the neutrino flux should remain roughly constant. But the ability to plot the flux of the neutrinos as a function of this zenith angle showed that there was in fact a dependence. Figure 2.4 shows the results of a study published in 1998 by the Super-Kamiokande (SK) collaboration, the descendant of Kamiokande-II (see Section 3.3.2 for details of SK). The ν_e flux agreed with prediction, as did the ν_μ flux of those neutrinos originating in the atmosphere above the detector, but the ν_μ flux of those coming through the Earth was as low as half that expected [19].

The dependence was arising due, not to the Earth directly, but to the difference in the distance travelled; neutrinos from above were travelling only about 15 km before hitting the detector, whereas neutrinos from below were travelling up to 13000 km.

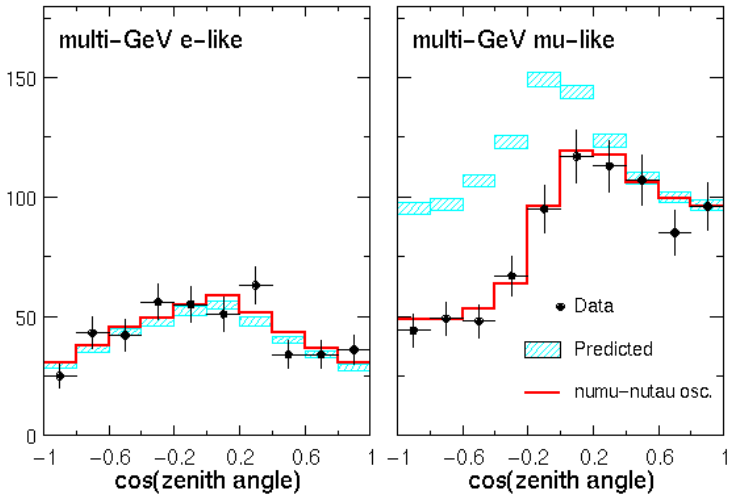

Figure 2.4: Zenith angle distribution for (left) electron-like events (i.e. those that appear to originate from electron neutrinos) and (right) muon-like events. The hashed boxes give the predicted distributions based on no neutrino oscillations. The data (black markers) agree with the prediction for electron-like events, and for the muon-like events with positive zenith angle (i.e. events from above the detector), but a clear deficit is seen for events coming through the Earth, agreeing with the solid histogram prediction for ν_μ to ν_τ oscillations. Image modified from [20].

These latter were able to oscillate to other flavours on their journey through the Earth. Moreover, the oscillating neutrino flavour could also be inferred: the ν_μ component was disappearing but the ν_e component was not increasing; the ν_μ must have mainly oscillated to ν_τ.

The phenomenon of neutrino oscillation is the first evidence of physics beyond the Standard Model and a precise knowledge of their oscillatory behaviour is one of the leading goals of particle physics today.

2.3 Neutrino oscillation theory

The existence of neutrino oscillations implies that the three known neutrino flavours created in CC weak interactions with matter are superpositions of underlying mass eigenstates by which neutrinos propagate through space [21],

$$|\nu_\alpha\rangle = \sum_i U^*_{\alpha i} |\nu_i\rangle \,, \tag{2.6}$$

where $|\nu_\alpha\rangle$ are the neutrino flavour, or weak, eigenstates with $\alpha = e, \mu, \tau$ and $|\nu_i\rangle$ the mass eigenstates with $i = 1, 2, 3$. The $U^*_{\alpha i}$ are elements of a 3×3 unitary[7] matrix that parameterises this mixing; the Pontecorvo-Maki-Nakagawa-Sakata, or PMNS, matrix, which can be written as the product of three matrices emphasising the application to different mixing sectors:

$$U = \underbrace{\begin{pmatrix} 1 & 0 & 0 \\ 0 & c_{23} & s_{23} \\ 0 & -s_{23} & c_{23} \end{pmatrix}}_{\text{atmospheric}} \underbrace{\begin{pmatrix} c_{13} & 0 & s_{13}\mathrm{e}^{-\mathrm{i}\delta_{CP}} \\ 0 & 1 & 0 \\ -s_{13}\mathrm{e}^{\mathrm{i}\delta_{CP}} & 0 & c_{13} \end{pmatrix}}_{\text{reactor/long baseline}} \underbrace{\begin{pmatrix} c_{12} & s_{12} & 0 \\ -s_{12} & c_{12} & 0 \\ 0 & 0 & 1 \end{pmatrix}}_{\text{solar}}, \quad (2.7)$$

where $s_{ij} = \sin\theta_{ij}$, $c_{ij} = \cos\theta_{ij}$, and δ_{CP} is a complex phase that will be discussed later.[8] Expressed as a single matrix, this is:

$$U = \begin{pmatrix} c_{13}c_{12} & c_{13}s_{12} & s_{13}\mathrm{e}^{-\mathrm{i}\delta_{CP}} \\ -c_{23}s_{12} - s_{13}c_{12}s_{23}\mathrm{e}^{\mathrm{i}\delta_{CP}} & c_{23}c_{12} - s_{13}s_{12}s_{23}\mathrm{e}^{\mathrm{i}\delta_{CP}} & c_{13}s_{23} \\ s_{23}s_{12} - s_{13}c_{12}c_{23}\mathrm{e}^{\mathrm{i}\delta_{CP}} & -s_{23}c_{12} - s_{13}s_{12}c_{23}\mathrm{e}^{\mathrm{i}\delta_{CP}} & c_{13}c_{23} \end{pmatrix}. \quad (2.8)$$

Given the relationship in Equation (2.6), it is possible to formalise the probability that a neutrino created in a certain flavour eigenstate $|\nu_\alpha\rangle$ at position ($\boldsymbol{x} = \mathbf{0}$) is detected later at position ($\boldsymbol{x} = \mathbf{L}$) to be in a different flavour eigenstate, $|\nu_\beta\rangle$.

If a neutrino mass eigenstate is a plane wave solution of the time-dependent Schrödinger equation, the state will evolve as follows:

$$|\nu_i(\boldsymbol{x}, t)\rangle = \mathrm{e}^{-\mathrm{i}\phi_i} |\nu_i(\mathbf{0}, 0)\rangle, \quad (2.9)$$

where the phase $\phi_i = E_i t - \boldsymbol{p}_i.\boldsymbol{x}$ contains all the information of the evolution. Inserting this into Equation (2.6), the neutrino flavour eigenstate evolves as:

[7] The unitary nature of the PMNS matrix follows from the assumption that only the three known neutrino flavours exist.

[8] Here we assume that neutrinos are Dirac particles (see Section 2.4.5). In the case of Majorana neutrinos, two more phases exist. These are inaccessible to oscillation experiments and will not be discussed further.

$$|\nu_\beta(\boldsymbol{x},t)\rangle = \sum_i U^*_{\beta i} \mathrm{e}^{-\mathrm{i}\phi_i} |\nu_i(\mathbf{0},0)\rangle\,. \tag{2.10}$$

In quantum mechanics the probability amplitude of a transition of state is given by the overlap of the two state-vectors in Hilbert space. In the case of the pure neutrino state $|\nu_\alpha(\mathbf{0},0)\rangle$ evolving into $|\nu_\beta(\boldsymbol{x},t)\rangle$, the probability amplitude is:

$$\langle \nu_\beta(\boldsymbol{x},t) | \nu_\alpha(\mathbf{0},0)\rangle = \sum_i U_{\beta i} \mathrm{e}^{\mathrm{i}\phi_i} \langle \nu_i(\mathbf{0},0) | \nu_\alpha(\mathbf{0},0)\rangle\,, \tag{2.11}$$

where we have used the fact that $\langle\nu_\beta(\boldsymbol{x},t)|$ is the complex conjugate of Equation (2.10). $|\nu_\alpha(\mathbf{0},0)\rangle$ can be expanded out into the mass eigenstates using Equation (2.6) to give:

$$\langle \nu_\beta(\boldsymbol{x},t) | \nu_\alpha(\mathbf{0},0)\rangle = \sum_i \sum_j U_{\beta i} U^*_{\alpha j} \mathrm{e}^{\mathrm{i}\phi_i} \langle \nu_i(\mathbf{0},0) | \nu_j(\mathbf{0},0)\rangle\,. \tag{2.12}$$

The mass eigenstates are orthonormal, so the overlap is trivially evaluated:

$$\langle \nu_i(\mathbf{0},0) | \nu_j(\mathbf{0},0)\rangle = \begin{cases} 1 & \text{if } i=j, \\ 0 & \text{otherwise.} \end{cases} \tag{2.13}$$

This simplifies Equation (2.12) to:

$$\langle \nu_\beta(\boldsymbol{x},t) | \nu_\alpha(\mathbf{0},0)\rangle = \sum_i U_{\beta i} U^*_{\alpha i} \mathrm{e}^{\mathrm{i}\phi_i}. \tag{2.14}$$

Further assumptions are now made to simplify the calculation.[9] Firstly, it is assumed that all three mass eigenstates propagate with the same momenta, and then that the

[9] It must be noted, however, that these assumptions in no way affect the result; a full wavepacket treatment reaches the same conclusion, as is shown in [21].

mass eigenvalues $m_i \ll E_i$ so that the average energy, E, can be used. The Taylor expansion of the momentum can now be neglected after the second term:

$$p_i = p = \sqrt{E^2 - m_i^2} \approx E\left(1 - \frac{m_i^2}{2E^2}\right). \tag{2.15}$$

In addition, the relativistic approximation that the distance from the source to the detector is approximately equal to the travel time (in natural units), $x = t = L$, is imposed, and we can use:

$$\phi_i = EL - EL\left(1 - \frac{m_i^2}{2E^2}\right) = \frac{m_i^2 L}{2E} \tag{2.16}$$

in Equation (2.14):

$$\langle \nu_\beta(L, L) | \nu_\alpha(0, 0) \rangle = \sum_i U_{\beta i} U_{\alpha i}^* \mathrm{e}^{\mathrm{i}\frac{m_i^2 L}{2E}}. \tag{2.17}$$

The oscillation probability itself is found by taking the squared magnitude of the probability amplitude:

$$\begin{aligned} P(\nu_\alpha \to \nu_\beta) &\equiv |\langle \nu_\beta(L, L) | \nu_\alpha(0, 0) \rangle|^2 \\ &= \sum_i U_{\beta i} U_{\alpha i}^* \mathrm{e}^{\mathrm{i}\frac{m_i^2 L}{2E}} \sum_j U_{\beta j}^* U_{\alpha j} \mathrm{e}^{-\mathrm{i}\frac{m_j^2 L}{2E}}. \end{aligned} \tag{2.18}$$

Defining $\Delta m_{ij}^2 = m_i^2 - m_j^2$, this can be separated into two terms:

$$P(\nu_\alpha \to \nu_\beta) = \sum_i \sum_j U_{\beta i} U_{\alpha i}^* U_{\beta j}^* U_{\alpha j} + \sum_i \sum_j U_{\beta i} U_{\alpha i}^* U_{\beta j}^* U_{\alpha j} \left(\mathrm{e}^{-\mathrm{i}\frac{\Delta m_{ij}^2 L}{2E}} - 1\right). \tag{2.19}$$

The first term is equal to $\delta_{\alpha\beta}$ by unitarity. Any terms with values of $i = j$ disappear as Δm_{ij}^2 in the phase becomes zero. Finally, terms in which $i < j$, are the complex

conjugate of the corresponding term in which $j < i$, and hence this can be written as twice their real part, removing the corresponding terms:

$$P\left(\nu_\alpha \to \nu_\beta\right) = \delta_{\alpha\beta} + 2\sum_{i<j} \mathfrak{Re}\left[U_{\beta i}U^*_{\alpha i}U^*_{\beta j}U_{\alpha j}\left(\mathrm{e}^{-\mathrm{i}\frac{\Delta m^2_{ij}L}{2E}} - 1\right)\right]. \tag{2.20}$$

The real and imaginary parts of the exponential factors can be separated, yielding finally:

$$\begin{aligned} P\left(\nu_\alpha \to \nu_\beta\right) \quad &= \delta_{\alpha\beta} - 4\sum_{i<j} \mathfrak{Re}[U_{\beta i}U^*_{\alpha i}U^*_{\beta j}U_{\alpha j}]\sin^2\left(\frac{\Delta m^2_{ij}L}{4E}\right) \\ &\quad +2\sum_{i<j} \mathfrak{Im}[U_{\beta i}U^*_{\alpha i}U^*_{\beta j}U_{\alpha j}]\sin\left(\frac{\Delta m^2_{ij}L}{2E}\right). \end{aligned} \tag{2.21}$$

For antineutrinos, the calculation should begin with the complex conjugate of (2.6). The existence of δ_{CP} in the PMNS matrix therefore results in the third term in Equation (2.21) containing a change of sign between neutrinos and antineutrinos. If δ_{CP} is not such that this imaginary component vanishes, the difference in oscillation probability that results could solve one of the fundamental mysteries of the universe, as will be discussed in Section 2.4.2.

2.3.1 Matter effects

The theory of neutrino oscillations can be complicated by the effect of neutrino interactions with the matter they are traversing. Neutral-current (NC) scattering interactions are accessible to all three known neutrino flavours in the same way, but this is not the case for CC interactions. The existence of electrons in matter makes possible the scattering of electron neutrinos via the exchange of a W boson, which cannot happen with the other neutrino flavours due to lepton family number conservation. In consequence, in matter there is a different effective mass splitting to that in a vacuum, as the electron neutrino effective mass increases without a corresponding increase in the other neutrino masses, resulting in a change in the oscillation probability. In illustrating this effect, known as the Mikheyev-Smirnov-Wolfenstein (MSW) effect [22] [23], it is usual to consider only the effect on a simpler

two-flavour scenario. In a two-flavour scenario, the mixing matrix is simply a two-dimensional rotation matrix [24]:

$$U_{2-\text{flav.}} \equiv \begin{pmatrix} \cos\theta & \sin\theta \\ -\sin\theta & \cos\theta \end{pmatrix}. \tag{2.22}$$

Inserting this into Equation (2.21) gives the oscillation probability in a vacuum:

$$P_{2-\text{flav.}}\left(\nu_\mu \to \nu_e\right) = \sin^2 2\theta \sin^2\left(1.27\Delta m^2 \frac{L}{E}\right). \tag{2.23}$$

In matter, the oscillation probability is modified to [25]:

$$P^{\text{M}}_{2-\text{flav.}}\left(\nu_\mu \to \nu_e\right) = \sin^2 2\theta_{\text{M}} \sin^2\left(1.27\Delta m^2_{\text{M}} \frac{L}{E}\right), \tag{2.24}$$

where the effective parameters are related to the vacuum parameters in the following way:

$$\begin{aligned} \sin^2\left(2\theta_{\text{M}}\right) &\equiv \frac{\sin^2 2\theta}{\sin^2 2\theta + \left(\cos 2\theta - x_\nu\right)^2}, \\ \Delta m^2_{\text{M}} &\equiv \Delta m^2 \sqrt{\sin^2 2\theta + \left(\cos 2\theta - x_\nu\right)^2}, \end{aligned}$$

where

$$x_\nu \equiv \frac{2\sqrt{2}\,\text{G}_F\, N_e\, E}{\Delta m^2}. \tag{2.25}$$

G_F is the Fermi constant, and N_e is the electron number density. It can be seen from Equations (2.25) that, as expected, an electron number density of zero results in the original vacuum oscillation probability equation.

Additionally it should be noted that, in going from neutrinos to antineutrinos, $x_\nu \to -x_\nu$, so antineutrinos will oscillate differently to neutrinos in an experiment through

matter, whether the PMNS matrix has complex parameters or not, complicating the search for underlying neutrino-antineutrino differences.

2.4 The future of neutrino physics

Having described the history and theory of neutrino oscillations, in this section the current knowledge of the parameters governing this phenomenon are reviewed. A selection of as yet unanswered questions in the field of neutrino physics are then detailed, before a discussion of some of the experiments that are likely to make a contribution in the near future.

2.4.1 Current knowledge of oscillation parameters

In the three-neutrino framework, seven parameters are required to describe oscillations: the three mixing angles between the flavour and mass eigenstates, $\theta_{12},\ \theta_{13},\ \theta_{23}$; the $\mathcal{CP}$-violating phase, δ_{CP}; two squared mass differences, which can be defined to be $\delta m^2 = m_2^2 - m_1^2 > 0$ and the much larger[10] $\Delta m^2 = m_3^2 - (m_1^2 + m_2^2)/2$; and finally, the sign of Δm^2 [26] [27]. Of these, five are now known with reasonable precision, whilst δ_{CP} and the sign of Δm^2 are not.[11]

At the time of T2K's proposal, θ_{13} was also unknown; one of T2K's primary design purposes was to establish the value. Since that time, evidence for a non-zero value has been firmly established; a global fit to the current data excludes $\sin^2\theta_{13} = 0$ at 10.2σ [28]. Effort is now focussing on precisely measuring θ_{13}. At the time of writing, the highest precision measurements come from the reactor experiments, Daya Bay, Double Chooz and RENO, which search for the disappearance of electron antineutrinos, and from the long-baseline accelerator experiments MINOS and T2K, which alternatively search for the appearance of electron neutrinos in a muon neutrino beam. Before discussing the other known parameters in the context of a global fit to the available data, a short section introducing the experiments that contributed to our current knowledge of θ_{13} will be given.

[10] Δm^2, the splitting between the third mass eigenstate and the average of the other two is often used currently. This is because the uncertainty on the large mass splitting is larger than the smaller mass splitting itself. See Table 2.1.

[11] The θ_{23} octant is also unknown at present.

Daya Bay

The Daya Bay experiment [29] in China consists of six functionally-identical reactors grouped into three pairs, with inverse β-decay interactions in six detectors,[12] ranging in distance from 350 m to 2000 m from the reactors, used to measure the oscillated electron antineutrino flux. The prompt scintillation of the positron and the later release of several photons from the captured neutron forms the electron antineutrino signature. For this purpose, each detector is composed of three nested volumes: the innermost volume contains 20 tons of gadolinium-doped liquid scintillator and acts as the antineutrino target. Surrounding this is 20 tons of pure liquid scintillator that acts to detect the escaping photons from the neutron capture and finally, the 37 ton mineral oil outer volume is used to veto external radiation.

The latest Daya Bay result saw 28909 signal candidate events in 139 days of data taking [30]; a deficit of 5.6% to that expected assuming no oscillations. A rate-only analysis gives a best fit value of:

$$\sin^2 2\theta_{13} = 0.089 \pm 0.010(\text{stat.}) \pm 0.005(\text{syst.}).$$

Double Chooz

Double Chooz is a two-reactor, two-detector experiment based in France. For the result obtained from the 228 live-day running period, however, the near detector was unused [31]. The far detector is located equidistant from the two nuclear reactors, at a baseline of 1050 m and has a 10 m^3 fiducial volume.

Expecting to see 8937 signal candidate events in the absence of oscillations, Double Chooz only saw 8249. This deficit, interpreted as the disappearance of the antineutrinos, gives a best fit value of [31]:

$$\sin^2 2\theta_{13} = 0.109 \pm 0.030(\text{stat.}) \pm 0.025(\text{syst.}). \tag{2.26}$$

[12] Two more detectors are soon to be added.

RENO

The six reactors utilised by the RENO[13] experiment [32] in South Korea are situated in a line spanning 1.3 km, with approximately equal spacing between each pair. Two detectors, the near detector at a distance of 294 m and the far detector at a distance of 1383 m from the centre of the reactor line, are used to measure the electron antineutrino flux. These each contain 16 ton of gadolinium-doped scintillator as the antineutrino target, and are both substantially shielded from cosmic ray backgrounds with 120 m and 450 m of rock overburden respectively.

RENO reported a rate-only analysis using data from 229 days of running, in which the far detector collected 17102 signal candidates, yielding a best fit value of [32]:

$$\sin^2 2\theta_{13} = 0.113 \pm 0.013(\text{stat.}) \pm 0.019(\text{syst.}). \tag{2.27}$$

MINOS

MINOS[14] was a 735 km baseline neutrino oscillation experiment in the USA that used the NuMI[15] beamline at Fermilab for a ν_μ or $\bar{\nu}_\mu$ beam of 3 GeV peak energy. At 1.04 km from the neutrino production point, the near detector measured the initial composition of the beam, and the far detector, a 3.3 kiloton fiducial mass tracking calorimeter, measured the beam composition after the full baseline, in order to infer the oscillation of the neutrinos along the way. The neutrino flavour undergoing a CC interaction could be inferred by the presence of a lengthy muon track in the case of ν_μ or an electromagnetic shower for ν_e interactions. Charged particle curvature induced by magnetic fields also meant that muon charge signs could be determined, and hence ν_μ could be distinguished from $\bar{\nu}_\mu$.

Using their full data sample, MINOS reported a combined fit to θ_{13} and θ_{23} assuming that $\theta_{23} < \frac{\pi}{4}$ and $\delta_{CP} = 0$. They did this under NH and IH assumptions and their best fit values were [33]:

$$2\sin^2(2\theta_{13})\sin^2(\theta_{23}) = 0.051^{+0.038}_{-0.030}(\text{NH});\;\; 0.093^{+0.054}_{-0.049}(\text{IH}). \tag{2.28}$$

[13] Reactor Experiment for Neutrino Oscillations.
[14] Main Injector Neutrino Oscillation Search.
[15] Neutrinos at the Main Injector.

Parameter	Best fit	1σ range
$\sin^2\theta_{12}/10^{-1}$	3.08	2.91–3.25
$\sin^2\theta_{13}/10^{-2}$ (NH)	2.34	2.16–2.56
$\sin^2\theta_{13}/10^{-2}$ (IH)	2.39	2.18–2.60
$\sin^2\theta_{23}/10^{-1}$ (NH)	4.25	3.98–4.54
$\sin^2\theta_{23}/10^{-1}$ (IH)	4.37	4.08–4.96 $\oplus$ 5.31–6.10
δ_{CP}/π (NH)	1.39	1.12–1.72
δ_{CP}/π (IH)	1.35	0.96–1.59
$\delta m^2/10^{-5}\,\mathrm{eV}^2$	7.54	7.32–7.80
$\Delta m^2/10^{-3}\,\mathrm{eV}^2$ (NH)	2.44	2.38–2.52
$\Delta m^2/10^{-3}\,\mathrm{eV}^2$ (IH)	2.40	2.33–2.47

Table 2.1: Global fits to neutrino oscillation parameters using data up to that published in 2013. In this table, NH stands for normal hierarchy, and IH stands for inverted hierarchy (see Section 2.4.3). Table reproduced from [26].

T2K

The long-baseline accelerator experiment in Japan, T2K [34], will be discussed in greater depth in Chapter 3. The reader is referred to that chapter for an in-depth review of the experiment; here the current best results are noted.

In a normal mass hierarchy scenario (see Section 2.4.3) in which $|\Delta m^2_{32}| = 2.4 \times 10^{-3}\,\mathrm{eV}^2$, θ_{23} is maximal and δ_{CP} is zero, the best fit value is [35]:

$$\sin^2 2\theta_{13} = 0.140^{+0.038}_{-0.032}. \tag{2.29}$$

The other oscillation parameters are also being more and more precisely measured by these and other experiments around the world. These measurements are being used in global fits [26] [27]; the results of these fits are summarised in Table 2.1.

Table 2.1 shows that the value of the parameter δ_{CP} has so far been constrained only minimally. Further constraints on this parameter have now become the primary goal of many new oscillation experiments as a non-zero value would allow the possibility of $\mathcal{CP}$ violation in the lepton sector, which could explain one of the biggest mysteries

in particle physics today.

2.4.2 $\mathcal{CP}$ violation

The visible universe is overwhelmingly dominated by matter. It is thought, however, that immediately after the Big Bang equal amounts of matter and antimatter were created. These two facts lead to the conclusion that matter and antimatter must behave differently in their interactions. Indeed, Sakharov, in 1967 [36], noted down the required conditions for a matter-antimatter asymmetry to exist:

- Existence of baryon and lepton number violating processes;
- Interaction outside of thermal equilibrium;
- Existence of $\mathcal{C}$ and $\mathcal{CP}$ violating processes.

The final condition introduces $\mathcal{C}$, and $\mathcal{CP}$, violation. $\mathcal{C}$ is the charge conjugation operator, the application of which swaps a particle for its antiparticle. The parity operator, $\mathcal{P}$**,** reverses the sign of all three spatial components of a particle's position, and $\mathcal{CP}$ is simply the operator that combines both of these operations.

The violation of $\mathcal{CP}$-symmetry has been observed already in quark mixing, but this is insufficient to account for the baryon asymmetry in the visible universe [37]. However, if the $\mathcal{CP}$-violating parameter in the PMNS matrix, δ_{CP}, is non-zero, $\mathcal{CP}$ violation in neutrino mixing may be able to explain this asymmetry through the process of leptogenesis [38].

Neutrino oscillation experiments have the ability to probe δ_{CP} by studying the normalised difference in oscillation probabilities for neutrinos and antineutrinos, known as the $\mathcal{CP}$ asymmetry:

$$\mathcal{A}_{\mathcal{CP}}(E_\nu) = \frac{P(\nu_\mu \to \nu_e) - \bar{P}(\bar{\nu}_\mu \to \bar{\nu}_e)}{P(\nu_\mu \to \nu_e) + \bar{P}(\bar{\nu}_\mu \to \bar{\nu}_e)}. \tag{2.30}$$

Experiments can only study neutrino oscillations through the observable particles produced in neutrino interactions with matter, so a measurement of this asymmetry is dependent on precise knowledge of neutrino and antineutrino cross-sections. Whether $\mathcal{CP}$ violation in the lepton sector can explain the baryon asymmetry observed in the universe is the most important unanswered question in neutrino physics today, so knowledge of these cross-sections is essential.

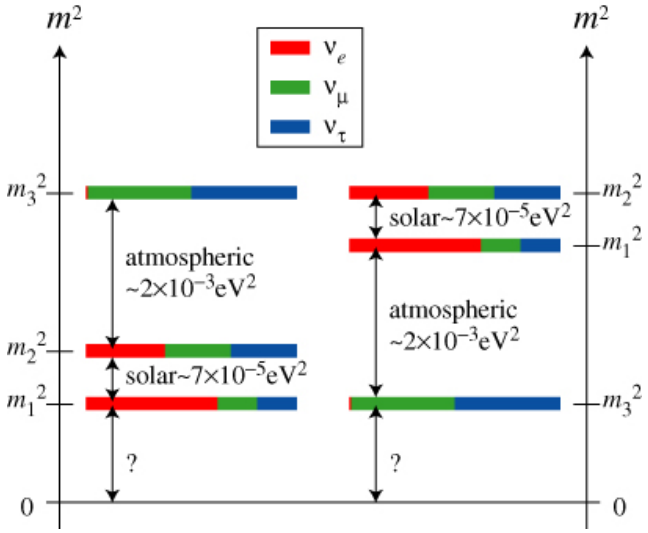

Figure 2.5: Possible neutrino mass hierarchies: the normal hierarchy (left) and the inverted hierarchy (right). Colours show the flavour eigenstate composition of the mass eigenstates, as determined by neutrino oscillation experiments. Figure reproduced from [39].

2.4.3 Neutrino mass hierarchy

We know from the existence of neutrino oscillations that, of the three known neutrino mass eigenstates, at least two mass values must be non-zero. The mass difference between states ν_1 and ν_2 is known through solar neutrino oscillations, but the sign of the much larger difference[16] between ν_3 and ν_1 ($\approx \nu_2$) is not; that is, the ν_3 could have the largest mass (normal hierarchy, NH) or the smallest (inverted hierarchy, IH), as shown in Figure 2.5.

The mass ordering of these eigenstates is an important quantity that has consequences for neutrino oscillations in matter. Any long-baseline experiment that aims to make a precision measurement of δ_{CP} therefore requires knowledge of the mass hierarchy so that effects due to this can be separated from effects due to the $\mathcal{CP}$-violating phase.

Determination of the neutrino mass hierarchy using combined data from T2K and NOνA (see Section 2.4.7) may or may not be possible, depending on the true value of δ_{CP} [40]. If this is not possible, future long-baseline, or other neutrino experiments will be required to make the measurement in order for δ_{CP} to be determined.

[16]The absolute value of which has been measured using atmospheric neutrinos.

2.4.4 Absolute neutrino mass

It is natural also to try to make a measurement of the absolute neutrino mass. There are thought to be approximately 336 relic[17] neutrinos/cm^3 in the universe, so the neutrino mass values can play quite a large role in the overall mass balance [41]. Long-baseline neutrino experiments are only ever sensitive to the mass splittings, so other methods are required to measure the absolute values. The current best limits come from the Mainz [41] and Troitzk [42] experiments,[18] which study the β-decay of tritium. These experiments look in great detail at the electron energy spectrum produced in the decay:

$$^3\mathrm{H} \rightarrow {}^3\mathrm{He}^+ + e^- + \bar{\nu}_e. \tag{2.31}$$

The endpoint distortion of the electron spectrum due to the 'missing' energy required for the neutrino mass is used to make the measurement, and from this the Mainz and Troitzk experiments have set limits of [41]:

$$m_{\bar{\nu}_e} < 2.3\,\mathrm{eV}\ (95\%\ \mathrm{C.L.}) \tag{2.32}$$

and [42]:

$$m_{\bar{\nu}_e} < 2.2\,\mathrm{eV}\ (95\%\ \mathrm{C.L.}) \tag{2.33}$$

respectively.

The two experiments have now reached their sensitivity limits, but a further tritium β-decay experiment is due to begin taking data in late 2015. The KArlsruhe TRItium Neutrino (KATRIN) experiment is expected to obtain a sensitivity down to 0.2 eV at the 90% confidence level after 5 years of running [43].

[17] Often called the cosmic neutrino background, these particles are relics of the Big Bang.

[18] It is the effective mass of the electron neutrino eigenstate that is specifically measured in these experiments; a weighted mean of the three mass eigenstates.

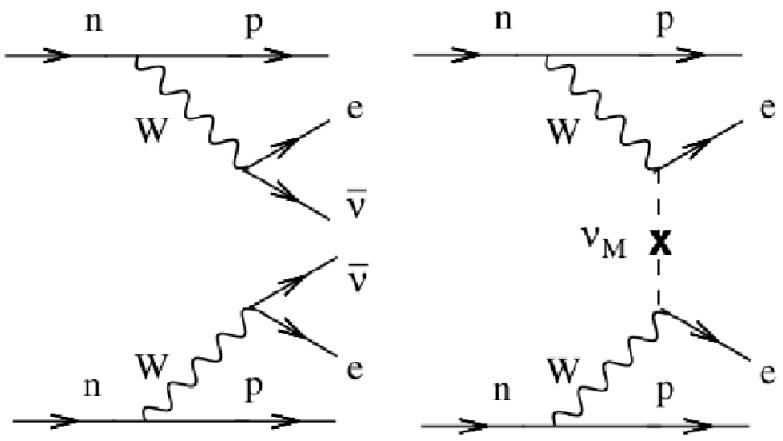

Figure 2.6: Feynman diagrams for (left) $2\nu\beta\beta$ and (right) $0\nu\beta\beta$. Image from [44].

2.4.5 Majorana or Dirac nature of neutrinos

The fact that neutrino masses are so small compared to the other fermions in the Standard Model is an interesting observation, as it suggests that their origin is perhaps different to the coupling to the Higgs field experienced by other fermions. One such alternative is that neutral fermion fields also couple directly to their charge conjugate, implying that neutrinos are identical to their antiparticles. Neutrinos of this nature are called Majorana fermions (as opposed to Dirac fermions, where, for example, $\nu \neq \bar{\nu}$) after this possibility was put forward in 1937 by Ettore Majorana [45].

The Majorana nature of neutrinos can be established by searching for a process called neutrinoless double β-decay. Neutrons in the nucleus are able to decay into a proton, emitting an electron and electron antineutrino, a process known as β-decay. If neutrinos are Majorana particles, however, then two simultaneous decays could result in the virtual neutrino emitted in one process being absorbed in the other. This is neutrinoless double β-decay, $0\nu\beta\beta$. The Feynman diagrams for $2\nu\beta\beta$ and $0\nu\beta\beta$ are shown in Figure 2.6.

Neutrinoless double β-decay has not yet been observed. Results from phase I of the GERDA experiment [46] using ^{76}Ge give the lower limit on the half-life:

$$T_{1/2}^{0\nu\beta\beta} > 2.1 \times 10^{25}\,\text{yr (90\% C.L.)}.$$

The neutrinoless double β-decay half-life due to the exchange of a light Majorana neutrino can be related to, $m^{\beta\beta}$, the effective Majorana mass of the electron neutrino [47]:

$$\left(T_{1/2}^{0\nu\beta\beta}\right)^{-1} = G^{0\nu\beta\beta}|M^{0\nu\beta\beta}|^2 m_{\beta\beta}^2, \tag{2.34}$$

where $G^{0\nu}$ is the phase space and $M^{0\nu\beta\beta}$ is the transition element for the process. Using equation (2.34), the limit obtained by the GERDA collaboration gives the range for the upper limit on the effective electron neutrino mass as $0.2 - 0.4\,\text{eV}$ [46].

Studies have also been conducted using ^{136}Xe. The best current limit comes from the EXO-200 collaboration [48]:

$$T_{1/2}^{0\nu\beta\beta} > 1.1 \times 10^{25}\,\text{yr (90\% C.L.)}.$$

2.4.6 Sterile neutrinos

In the 1970s, experiments at the CERN Large Electron Positron Collider (LEP) made very precise measurements of the invisible decay width of the Z boson [49]. This indicated that there are three types of active neutrino with masses less than half that of the Z. Reinforcing this, studies from the Planck spacecraft in 2013 [50] give results consistent with the existence of just three light, weakly-coupling neutrinos, though this data does not rule out the possibility of four.[19]

However, there have been hints that at least one extra neutrino exists from oscillation experiments. The hints suggest that the extra neutrino mass would be small enough that, if the particle coupled to the weak force, it could be produced in pairs by the decay of the Z boson. We know that this cannot be the case, so these neutrinos would have to be 'sterile'. Here the indications for the existence of sterile neutrinos are briefly described.

[19] The data give a value of the relativistic degrees of freedom, which can be considered as the effective number of neutrino types, $N_{\text{eff}} = 3.30 \pm 0.27$

The LSND anomaly

The Liquid Scintillator Neutrino Detector (LSND) was an accelerator-based short baseline experiment searching for $\bar{\nu}_e$ appearance in a predominantly $\bar{\nu}_\mu$ beam. An excess of ν_e-like events were seen at low energy, which could be interpreted as an oscillation probability of $0.264 \pm 0.067 \pm 0.045$ [51]. Additionally, a study of ν_e in the beam from in flight pion decay also found an excess consistent with the same oscillation probability [52]. A fit to the data gives a favoured mass splitting region from $0.2 - 2.0\,\mathrm{eV}^2$ [53]. This is incompatible with the current known mass splittings by at least two orders of magnitude, pointing to the possible existence of an as yet undiscovered neutrino.

The gallium anomaly

The GALLEX and SAGE solar neutrino experiments have both seen deficits in the number of electron neutrinos detected when calibrating their detectors. The experiments inserted radioactive sources that decayed by electron capture into their detectors, and the electron neutrinos emitted in this process were detected by the reaction $\nu_e + {}^{71}\mathrm{Ga} \rightarrow {}^{71}\mathrm{Ge} + e^-$. The combined deficit of both experiments amounts to 2.7σ [54], with a natural explanation originating in very short baseline oscillations, which would occur at this distance from a new mass splitting $\Delta\mathrm{m}^2 \geq 0.1\,\mathrm{eV}^2$ [53].

The reactor antineutrino anomaly

Many nuclear reactor experiments have also seen a deficit in $\bar{\nu}_e$ over a very short baseline. In a reactor experiment, the outgoing flux of electron antineutrinos from nuclear fission within the reactor core must be modelled very precisely. Although all slightly low, each experiment agreed with this model in the standard three neutrino framework, until late 2010. In preparation for the initiation of the Double Chooz experiment, these models were checked, and updated. The reevaluated flux was increased by a few percent, and in consequence all reactor neutrino experiments show a deficit at a near 3σ significance, which could again be explained by oscillations to sterile neutrinos with a new mass splitting $\Delta\mathrm{m}^2 > 0.2\,\mathrm{eV}^2$ (99%) [53].

2.4.7 New and upcoming experiments

Although great progress has been made in neutrino physics, it has been shown that there are still many important questions left unsolved. In this section a selection of recently commissioned or upcoming experiments that aim to play a role in answering these questions are reviewed.

NOνA

NOνA[20] [55] is an 810 km baseline, 2 GeV peak neutrino energy oscillation experiment taking advantage of the existing NuMI beamline at Fermilab, that saw its first far detector neutrinos from the accelerator in February 2014. The near detector at 240 m from the neutrino source, and the far detector, are both liquid scintillator cell tracking calorimeters, enabling excellent reconstruction capabilities.

Studies indicate that after approximately 12 years of running, NOνA can establish $\mathcal{CP}$ violation at the 95% C.L. for 20% of δ_{CP} values. This increases to 45% coverage in 24 years of running [56].

NOνA's long baseline also gives it good sensitivity to the neutrino mass hierarchy through matter effects. However, depending on the value of δ_{CP}, ambiguities may arise between MSW effects and true $\mathcal{CP}$-violating effects. The T2K experiment's electron neutrino appearance data set, on the other hand, depends very little on the mass hierarchy, and so it has been put forward that this could potentially be used to increase the sensitivity to the mass hierarchy through a combined fit. For δ_{CP} in the favourable half-plane ($-180° \leq \delta_{CP} \leq 0°$), NO$\nu$A should be able to determine the hierarchy at the 90% C.L. However, this would not be the case for true δ_{CP} values in the unfavourable half-plane. T2K data should be able to increase this sensitivity so that a 90% C.L. determination can be made for all values [57].

MINOS+

MINOS+ [58] is a continued exposure of the near and far detectors of the original MINOS experiment to the new NuMI beamline setting adapted for NOνA. The NuMI beam resumed delivery of neutrinos in 2013, and the intention is for a three year data-taking period, resulting in more than twice the number of total events collected by MINOS over the first five years.

[20] NuMI Off-axis ν_e Appearance Experiment.

MINOS+, being on-axis, is expected to highly complement the new off-axis NOνA experiment. It will be especially useful in its search for sterile neutrinos, with the ability to cover over three orders of magnitude of mass splitting between the sterile and known neutrinos [59].

Hyper-Kamiokande

Hyper-Kamiokande (HK) is a proposed next-generation detector to SK: a ring imaging water Čerenkov detector with a fiducial mass a factor of 25 times larger than its predecessor. This would be situated approximately 8 km south of SK, for a similar baseline to T2K.

It is expected that after 5 years of running with a 1.66 MW J-PARC beam, δ_{CP} can be constrained within 18° for all true values, if $\sin^2\theta_{13} > 0.03$ and the mass hierarchy is known. The fact that a larger θ_{13} has now been established increases the sensitivity. Moreover, this larger value of θ_{13} allows sensitivity to the mass hierarchy; it is expected that a greater than 3σ determination can be made for 46% of possible δ_{CP} values after 10 years of collecting atmospheric neutrino data [60].

LBNE

LBNE[21] plans to use a 34 kton fiducial mass liquid argon time projection chamber (LArTPC) as its far detector, sited in the location of the former Homestake gold mines in South Dakota, a distance of 1300 km from the neutrino source at Fermilab [61].[22] This detector will provide excellent position resolution and particle identification. The beam energy spectrum is planned to cover the first two oscillation maxima at 1300 km, at 2.5 GeV and 0.8 GeV, and hence the far detector will be on-axis.

At the time of writing, the near detector design is still under study. The detector should allow the study of interactions on the same target nucleus as the far detector in order that systematic uncertainties can be cancelled, it should be magnetised in order to distinguish neutrinos from antineutrinos, and should also be capable of distinguishing electrons from muons.

LBNE's large baseline will give high sensitivity to the neutrino mass hierarchy; preliminary studies indicate that the hierarchy can be discerned at 3σ significance,

[21] Long-Baseline Neutrino Experiment.
[22] After an initial phase which will see a 10 kton LArTPC as the far detector.

irrespective of the value of δ_{CP}, within 10 years of operation. Additionally, it is thought that the value of δ_{CP} may be pinpointed to $\pm 20°$–$30°$ (depending on its value) after this period of time [61].

2.5 Neutrino interactions

In the previous section, a selection of experiments that are likely to make contributions to the unanswered questions in the field of neutrino physics have been discussed. In order to study the neutrinos themselves, these experiments have to track the observable particles created at the interaction point. Therefore, any conclusions about neutrino processes require a good knowledge of how neutrinos interact with matter. In this section, the theory and current status of neutrino interaction physics is described.

2.5.1 Neutrino interaction theory

Of the three fundamental forces that play a role at subatomic scales, only the weak nuclear force is experienced by neutrinos. Therefore, neutrinos interact only through the exchange of the weak force carriers, the $W^{\pm}$ and Z bosons. In particle physics terms, these bosons are very massive, and hence the weak interaction gets its name from being very short-range, acting over approximately 10^{-18} m. In the case of a neutral-current (NC) interaction, a Z boson is exchanged, and a neutrino of the same flavour emerges in the final state. In a charged-current (CC) interaction, however, an electrically charged W boson is exchanged. In this case a charged lepton of the same flavour as the incoming neutrino emerges in the final state. These processes are depicted in Figure 2.7.

In 1956 T.D. Lee and C.N. Yang suggested that the weak interaction did not conserve parity [62]; that is, that a weakly-interacting system in which all particle coordinates were reversed would progress in a different way to the original system. The following year an experiment on the decays of Cobalt atoms [63] showed that this violation did exist; indeed, it was in fact maximal. A theory of the weak interaction has to take this violation into account, and this can be done by linearly combining vector and axial-vector components in the interaction currents [5]:[23]

[23]Note that here we assume the process involves only non-composite particles.

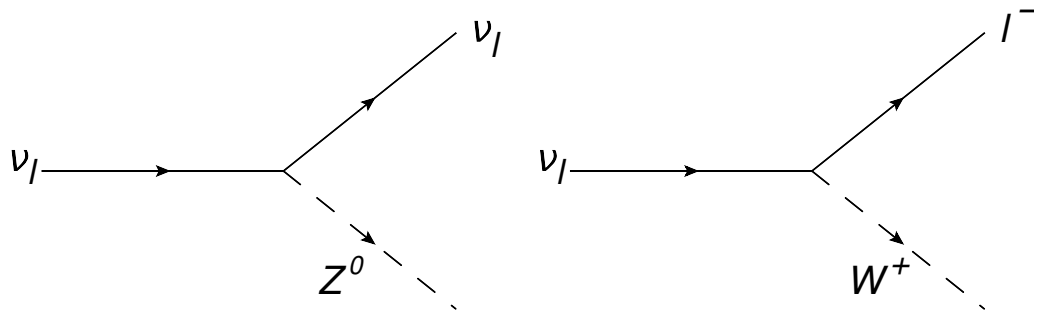

(a) (b)

Figure 2.7: Feynman diagrams depicting (a) a neutral-current neutrino interaction vertex, and (b) a charged-current neutrino interaction vertex.

Particle	c_V	c_A
Neutrino	$\frac{1}{2}$	$\frac{1}{2}$
Charged lepton	$-\frac{1}{2} + 2\sin^2\theta_{\mathrm{W}}$	$-\frac{1}{2}$
Up-type quark	$\frac{1}{2} - \frac{4}{3}\sin^2\theta_{\mathrm{W}}$	$\frac{1}{2}$
Down-type quark	$-\frac{1}{2} + \frac{2}{3}\sin^2\theta_{\mathrm{W}}$	$-\frac{1}{2}$

Table 2.2: Neutral-current vector and axial-vector vertex factor coefficients.

$$J^{\mathrm{CC},\mu} \equiv \bar{u}\frac{-\mathrm{i}g_W}{2\sqrt{2}}\left(\gamma^\mu - \gamma^\mu\gamma^5\right)u, \tag{2.35}$$

$$J^{\mathrm{NC},\mu} \equiv \bar{u}\frac{-\mathrm{i}g_Z}{2\sqrt{2}}\left(c_V\gamma^\mu - c_A\gamma^\mu\gamma^5\right)u. \tag{2.36}$$

In the above, the Dirac gamma matrix γ^μ represents a vector coupling and the product $\gamma^\mu\gamma^5$ an axial-vector coupling. Factors u and $\bar{u}$ are Dirac spinors describing the particles themselves, g_W and g_Z are numbers representing the coupling strengths and c_V and c_A are particle-dependent coefficients. As can be seen in Table 2.2, these coefficients are determined by the Weinberg angle, θ_{W}, a fundamental parameter that cannot be calculated but is measured precisely: $\sin^2\theta_{\mathrm{W}} = 0.23146(12)$ [64].

These currents represent the interaction vertex of the weak bosons with the fermions: νl in the case of the CC and $\nu\nu$ or ll in the NC case. In order to form the interaction amplitude, the propagation of the boson between interaction vertices must be included; this is contained in the propagator term:

$$\frac{-\mathrm{i}\left(g_{\mu\nu} - q_\mu q_\nu / M^2c^2\right)}{q^2 - M^2c^2}, \tag{2.37}$$

where $g^{\mu\nu}$ is the Minkowski metric, M is the boson mass and q^2 is the squared four-momentum transfer. At values of $q^2 \ll M^2c^2$, which is in practice most often the case, the propagator can be simplified to:

$$\frac{-\mathrm{i}g_{\mu\nu}}{M^2c^2}. \tag{2.38}$$

Putting these components together gives the transition amplitude, $\mathcal{M}$, between the initial and final state.

Cross sections

An interaction cross-section is a measure of the probability of interaction of an incoming particle with a target, defined as follows:

$$\sigma \equiv \frac{N}{\phi T}, \tag{2.39}$$

where N is the number of interactions in the target material, ϕ is the flux (the rate of incoming particles per unit area), and T is the number of targets for which the interaction can occur. The cross-section is a quantity that an experimentalist can measure, and is therefore often targeted for prediction within models so that the theory can be tested. In addition to the interaction amplitude described above, the theoretical prediction of a cross-section also demands the density of final states, which describes the kinematics of the interacting particles.

At neutrino energies of $\approx 1\,\mathrm{GeV}$, the neutrino wavelength is on the order of 10^{-15} metres, and neutrino interactions are dominated by those with individual nucleons. Unlike purely leptonic interactions, matrix amplitudes for interactions with nucleons cannot be calculated entirely analytically due to strong interaction effects in composite particles. Additionally, the other nucleons in the nucleus cannot be

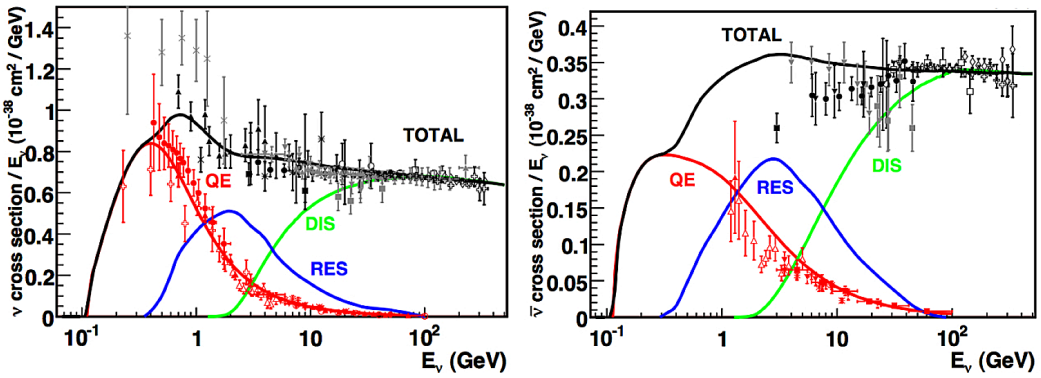

Figure 2.8: Total neutrino (left) and antineutrino (right) charged-current cross-sections per nucleon (for an isoscalar target) divided by neutrino energy and plotted as a function of energy. Taken from [66].

ignored[24] so that models of the nucleus are required. On the other hand, this nuclear environment allows the possibility of several underlying interaction processes that are not possible in purely leptonic interactions, giving a far richer physics program. Below, the main interactions at accelerator-based experiment energies [65] are summarised.

(Quasi-)elastic scattering: At neutrino energies up to $\approx$ 1GeV, the largest contributing interaction is elastic scattering:

$$\begin{aligned} \nu_\alpha n &\to \nu_\alpha n, \qquad \nu_\alpha p \to \nu_\alpha p, \\ \bar{\nu}_\alpha n &\to \bar{\nu}_\alpha n, \qquad \bar{\nu}_\alpha p \to \bar{\nu}_\alpha p, \end{aligned} \tag{2.40}$$

or quasi-elastic (QE) in the case of W boson exchange:

$$\nu_\alpha n \to l_\alpha^- p, \qquad \bar{\nu}_\alpha p \to l_\alpha^+ n. \tag{2.41}$$

This can be seen for CC interactions in Figure 2.8. In these events, the neutrino scatters off a target nucleon, releasing one (or more) nucleons in the final state. In the NC elastic scattering case, a neutrino is included in the final state. As shown in

[24] In modern neutrino experiments the need for high event rates, amongst other constraints, means that Hydrogen is not used as the target mass.

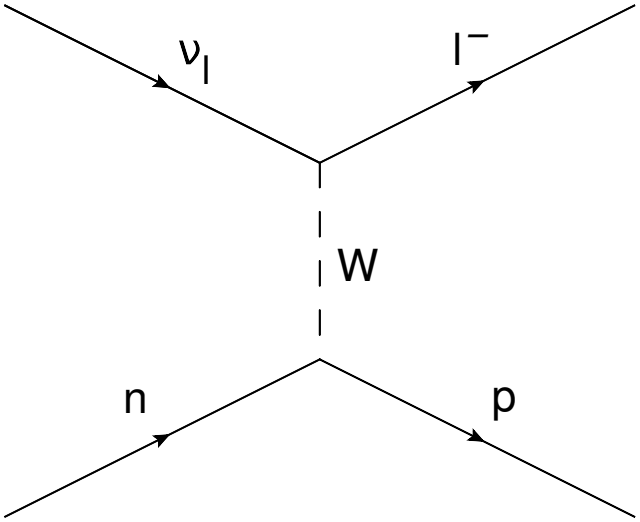

Figure 2.9: Charged-current quasi-elastic scattering Feynman diagram.

Figure 2.9, the final state in a CC interaction includes instead a charged lepton, so these are termed quasi-elastic due to the energy required to create the mass of the lepton.

Resonance production: As neutrino energies increase up to and beyond 1 GeV, the production of a baryonic resonant state (RES) from the excitation of the target nucleon becomes possible. The decay of this resonance can produce a variety of final state nucleons and mesons in the NC:

$$\begin{aligned} \nu_\alpha p &\to \nu_\alpha p \pi^0, \qquad \nu_\alpha p \to \nu_\alpha n \pi^+, \\ \nu_\alpha n &\to \nu_\alpha n \pi^0, \qquad \nu_\alpha n \to \nu_\alpha p \pi^-, \end{aligned} \tag{2.42}$$

and CC channels:

$$\nu_\alpha p \to l_\alpha^- p \pi^+, \qquad \nu_\alpha n \to l_\alpha^- n \pi^+, \qquad \nu_\alpha n \to l_\alpha^- p \pi^0. \tag{2.43}$$

Deep inelastic scattering: Above a neutrino energy of approximately 5 GeV (slightly higher in antineutrino interactions, as can be seen from Figure 2.8), deep inelastic scattering (DIS) begins to dominate. At this energy, the neutrino wavelength is so short that the quark constituents of an individual nucleon can be re-

solved. High momentum transfer results in the breaking up of the nucleon and the creation of a shower of particles as its constituent quarks hadronise.

Neutrino generators use models for these interactions that require tuning to real physics data; parameters found in the vector and axial-vector currents that describe vertex interactions with composite particles cannot be calculated. These parameters are the vector (of which there are two), axial-vector, and pseudoscalar nucleon 'form factors', which are functions of the squared four-momentum transferred in the interaction. Due to the 'conserved vector current' (CVC) hypothesis, which states that the vector weak charge is not affected by the strong interaction, and hence that electromagnetic form factors are linked to the weak vector form factors, electron scattering results can be used to extract values of the former [65]. The other form factors are then dependent on the interaction being studied, and the model used to describe it.

For charged-current quasi-elastic (CCQE) scattering for example, the Llewellyn-Smith model is commonly used [67]. The most obscure form factor in this CCQE model is the axial-vector form factor, which can only be measured by neutrinos. It is assumed that this has a dipole form depending on two subsidiary parameters:

$$F_A(Q^2) = \frac{F_A(0)}{\left(1 + Q^2/{M_A}^2\right)^2}. \tag{2.44}$$

The value of the axial-vector form factor at the zero four-momentum transfer limit, $F_A(0)$, has been very precisely measured using the β-decay of neutrons [64], so that the final parameter to be constrained was the 'axial mass', M_A. The average value of this parameter, from initial experiments on a deuterium target, was measured to be consistent with 1 GeV [68]. However, the nuclear effects that arise when using heavier target nuclei can alter the measured value of the parameter, and more recent experiments using carbon have proved inconsistent by up to 30% [69]. In addition to accurate interaction modelling, this highlights the need for good nuclear modelling in neutrino interaction studies.

2.5.2 Nuclear modelling

Up to now, the model adopted by many neutrino interaction generators, including the NEUT [70] generator used by T2K, is the Relativistic Fermi Gas Model

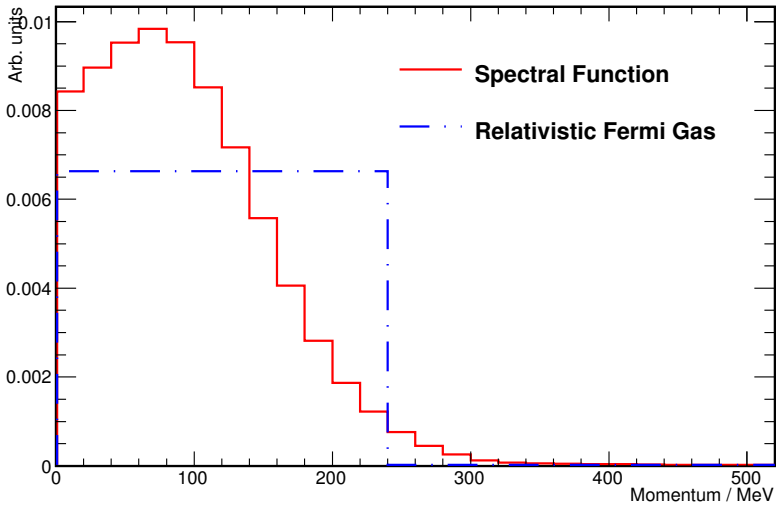

Figure 2.10: Nucleon momentum distributions in the Relativistic Fermi Gas model with a Fermi momentum of 220 MeV, and the Spectral Function model showing the high momentum tail due to nucleon-nucleon correlations. Figure from [71].

(RFG), but improved models of the nucleus are being studied. In this section the RFG model and a class of nuclear model called 'spectral functions' (SF) are briefly explained.

The relativistic Fermi gas model

This models the nucleons as a non-interacting Fermi gas, where particles occupy the lowest possible nuclear energy levels up to the Fermi energy. In recent years, the crude step-function nucleon momentum distribution (Figure 2.10) and the non-interacting nucleon assumption[25] has been found to be too simple to accurately model the nucleus, due in part to evidence from electron scattering data [72], and other models have been put forward.

Spectral functions

The term 'spectral function' refers to a model in which the momentum-energy distribution of nucleons within a nucleus, including the effect of the known existence of short-range (≈ 1 fm) correlations between them, is taken into account. The SF

[25] Often called the Impulse Approximation.

nucleon momentum distribution showing the high momentum tail resulting from short-range nucleon correlations is shown in Figure 2.10.

SF models more accurately represent the nuclear environment [73], and these have recently been added to the neutrino interaction generators used by T2K, with the intention that new productions of the T2K simulation will use them as the default.

2.5.3 Current understanding of neutrino cross sections

With the discovery of neutrino oscillations and the possibility that $\mathcal{CP}$ violation in the lepton sector can account for the baryon asymmetry observed in the universe, precise knowledge of neutrino interaction cross-sections on nuclear targets has been of paramount importance. This has become especially the case in the subsequent 'second-generation' era of precision parameter measurements in neutrino oscillation experiments, so in recent years there has been a renewed interest in measuring these cross-sections. However, currently the data is still sparse. The total[26] CC cross-section world data as of 2013 is contained in Figure 2.11. In particular, the paucity of antineutrino data at low energy is clear. Since that time, there have been further measurements by the ArgoNeuT experiment [74], but there are still no published total CC antineutrino cross-section measurements at energies as low as those available to T2K. With this in mind, Chapter 5 of this thesis presents a measurement of the flux-integrated $\bar{\nu}_\mu$ total CC cross-section, using a carbon-based target within the T2K near detector, which will be described in the next chapter.

[26] A total, or inclusive, charged-current cross-section measurement is one in which the final state particles accompanying the outgoing charged lepton are of no consequence. As can be seen from Figure 2.8, this total cross-section is the sum of the cross-sections of the exclusive final states described in Section 2.5.1.

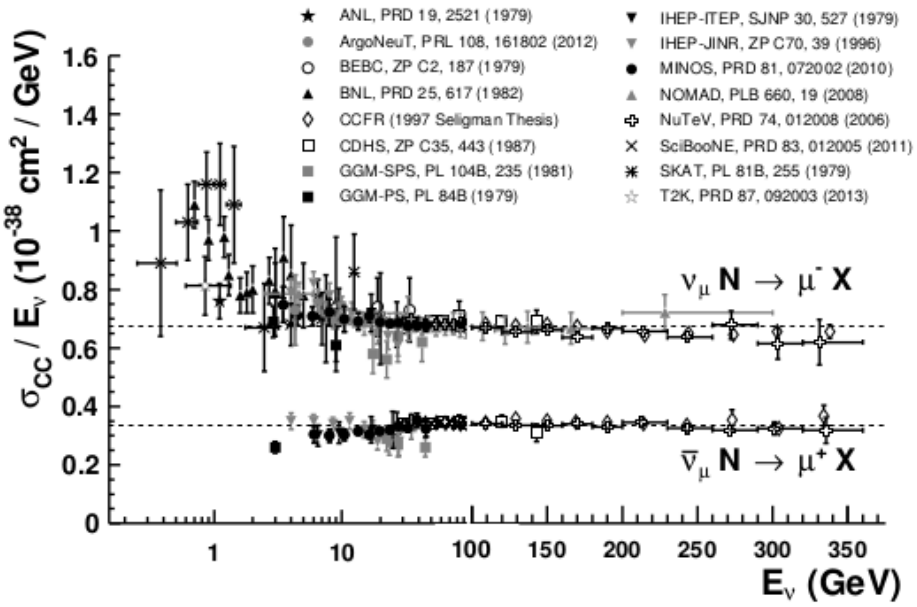

Figure 2.11: Total neutrino and antineutrino charged-current cross-sections per nucleon (for an isoscalar target) divided by neutrino energy and plotted as a function of energy. Figure from [64].

Chapter 3

The T2K Experiment

3.1 Introduction and motivation

T2K was proposed after the atmospheric neutrino anomaly had been explained by non-zero neutrino masses and the phenomenon of neutrino oscillations. The neutrino oscillation parameters were being studied, but greater precision was needed, and so a second generation of neutrino oscillation experiments were required.

T2K [34] is a long-baseline neutrino oscillation experiment built primarily to make a measurement of θ_{13}, the least constrained leptonic mixing angle at that point in time. The experiment, a sketch of the main components of which are shown in Figure 3.1, consists of a neutrino beamline that is generated at the J-PARC facility on the East coast of the Japanese island of Honshu, and fired 295 km across the country to be

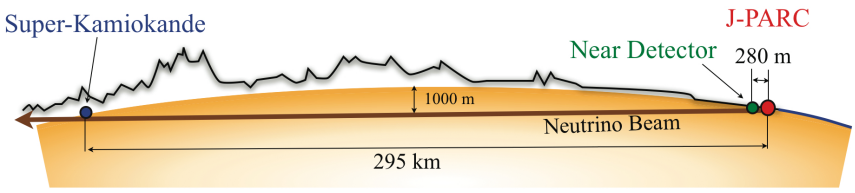

Figure 3.1: The main components of the T2K experiment. Image reproduced from [34].

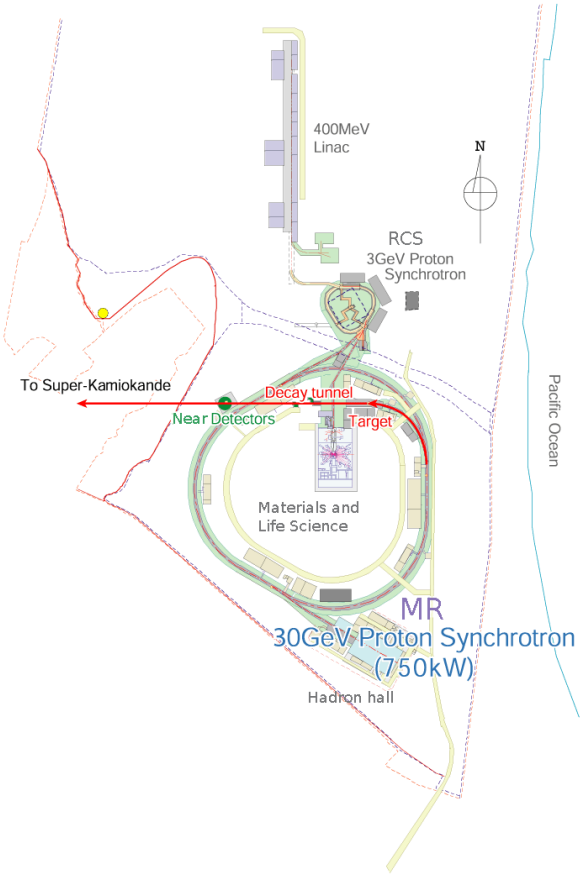

Figure 3.2: The J-PARC facility. Image modified from [75].

detected at the Super-Kamiokande far detector. Near the neutrino production point is a suite of near detectors, the ND280 and INGRID, which characterise the beam and give the opportunity to measure neutrino-nucleon cross-sections on a variety of targets: carbon, brass, water, lead and iron. These cross-sections are vital for the precision measurements of oscillation parameters, and the world data for these are currently very sparse.

3.2 J-PARC

The T2K muon neutrino beam is generated at the Japan Proton Accelerator Research Complex (J-PARC) in Tokai-mura on the Pacific coast of Japan; a schematic of the facility is shown in Figure 3.2.

3.2.1 Proton accelerator

Production of the neutrino beam begins with the acceleration of negative hydrogen ions to a kinetic energy of 400 MeV in the linear accelerator (LINAC) at the north side of the complex, before being stripped of electrons by charge-stripping foils at the 3 GeV rapid cycle proton synchrotron (RCS) injector. Approximately 5% of the protons are fed into the main ring (MR), a 30 GeV proton synchrotron, where they circulate at a frequency of 0.3 Hz, in eight separate bunches,[1] until full energy is reached. The rest of the protons from the RCS are used for other experiments at J-PARC in the Materials and Life Science experimental facility. The specifications of the proton accelerator components are given in Table 3.1.

3.2.2 T2K neutrino beamline

In order to direct the final neutrino beam towards the T2K far detector, protons for T2K are extracted on the inside of the MR as shown in Figure 3.2. They then enter the target station shown in Figure 3.3. Within the target station, the protons impact on the 914 mm long,[2] rod-shaped graphite target. These particle collisions produce pions and kaons, which will subsequently decay according to the decay channels listed in Table 3.2 (and their charge conjugates).

	LINAC	RCS	MR
Beam particles	H-	p	p
Extraction energy (GeV)	0.4	3	30
LINAC peak current (mA)	50	-	-
Particles per pulse / 10^{13}	-	8.3	33
Design beam power (MW)	-	1.0	0.75
Harmonic number	-	2	9
Repetition rate (Hz)	50	25	~ 0.3
Ring circumference (m)	-	348.33	1567.5
Extraction scheme	-	fast	fast & slow

Table 3.1: J-PARC accelerator specifications. From [76].

[1] Six bunches in T2K's first running period.
[2] Corresponding to 1.9 interaction lengths.

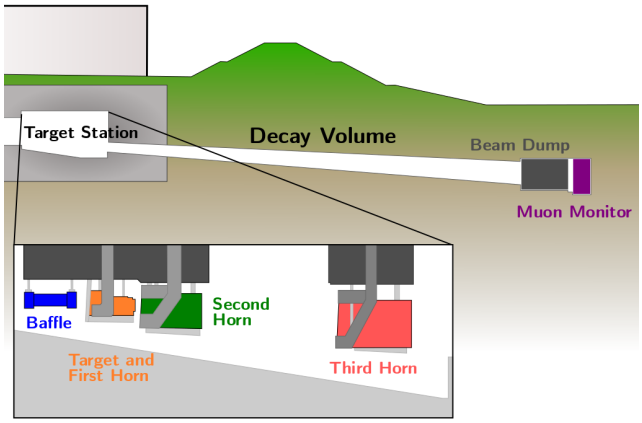

Figure 3.3: T2K neutrino beamline. From [77].

As the positive mesons will predominantly produce neutrinos, and the negative mesons predominantly antineutrinos, a particle or anti-particle beam can be created by focussing the relevant mesons and deflecting those of the wrong sign. This is done using three magnetic focussing horns, through each of which a current of approximately 250 kA flows. To protect the first horn from a misaligned or unfocussed proton beam, immediately upstream is a 0.3 m wide graphite block called the baffle.

The focussed mesons enter the 96 m long helium-filled decay volume. Beyond this,

Decay mode	Branching ratio (%)
$\pi^+ \to \mu^+ \nu_\mu$	99.99
$K^+ \to \mu^+ \nu_\mu$	63.55
$K^+ \to \pi^+ \pi^0$	20.66
$K^+ \to \pi^+ \pi^+ \pi^-$	5.59
$K^+ \to \pi^0 e^+ \nu_e$	5.07
$K^0_L \to \pi^- e^+ \nu_e$	40.55
$K^0_L \to \pi^- \mu^+ \nu_\mu$	27.04
$\mu^+ \to e^+ \nu_e \bar{\nu}_\mu$	≈ 100

Table 3.2: Pion and kaon branching ratios. Decays with branching ratios below 5% have been suppressed. Numbers from [64].

the graphite beam dump stops all muons with energies under 5 GeV that come from the decay of the mesons, leaving a beam of neutrinos. Energetic muons that are not stopped by the beam dump are detected by the muon monitor located immediately behind it and used to determine the neutrino beam direction. A muon neutrino beam generated in this way contains a contamination of muon antineutrinos and electron neutrinos due to the decay of kaons, as listed in Table 3.2, and also to the fact that some through-going wrong-sign mesons will not be deflected significantly by the horns. The T2K neutrino beam contains approximately 6% muon antineutrinos and approximately 1% electron neutrinos. Figure 3.4(a) illustrates this with the predicted energy spectra of the neutrino flavour components at the off-axis near detector. Figures 3.4(b) and 3.4(c) show the contributions to the ν_μ and $\bar{\nu}_\mu$ fluxes respectively from the meson and muon parents listed in Table 3.2. Due to these contaminations, an important step in maximising the sensitivity of an accelerator-based neutrino oscillation experiment is to characterise as accurately as possible the initial neutrino flavour composition and energy of the neutrino beam, in order that the change in the neutrino spectrum due to neutrino oscillations can be precisely measured. T2K makes use of a near detector suite for this purpose, which will be described, along with the far detector, in the next section.

3.3 Detectors

3.3.1 Off-axis design

Rather than having the central beam axis pointed directly through the near and far detectors, T2K is the first experiment in the world to have two of these detectors slightly off-axis. As shown in Table 3.2, the muon neutrino beam is produced primarily by the two-body decay of mesons; for mesons of a definite energy, the energy of the neutrinos can therefore be derived analytically from two-body kinematics. Neglecting the neutrino mass:

$$E_\nu = \frac{m_M^2 - m_\mu^2}{2(E_M - p_M \cos\theta)}. \tag{3.1}$$

In Equation (3.1), M denotes the parent meson, m is the mass of the particle, E is the energy and p its momentum. The angle θ is the off-axis angle. Figure 3.5(a) shows the effect of changing θ in pion decay. As the angle increases, the neutrino

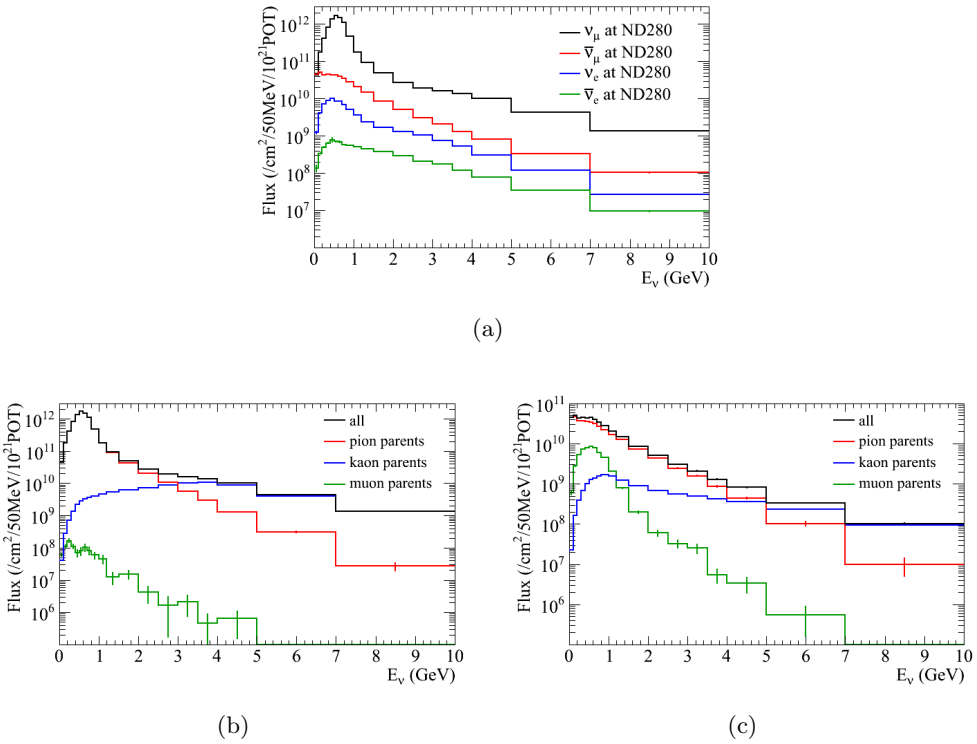

(a)

(b)

(c)

Figure 3.4: (a) Flux by neutrino flavour at ND280; (b), ν_μ flux by parent at ND280; (c), $\bar{\nu}_\mu$ flux by parent at ND280. Images from [78].

energy is reduced, and there is much less dependence of the neutrino energy on the pion momentum. This indicates that a larger off-axis angle produces a lower-energy, more monoenergetic beam. The T2K off-axis angle of $\sim 2.5°$, given the 295 km baseline, ensures that the mean muon neutrino energy is such that the oscillation probability at SK is maximised, i.e. the muon neutrino survival probability is minimised, as can be seen in Figure 3.5(b).

Removing higher-energy neutrinos has another advantage to neutrino oscillation experiments, where the 'golden channel' is the CCQE interaction (see Section 2.5.1). As this is another two-body interaction, the energy of the incoming neutrino can also be derived in this case from the kinematics. However, if a CCQE interaction is assumed when, in fact, further particles have been produced but have gone undetected, the reconstruction will underestimate the neutrino energy, distorting the oscillation probability as a function of energy.

The largest background to the ν_e appearance CCQE signal at Super-Kamiokande is from NC single neutral pion production from baryonic resonance, a process that

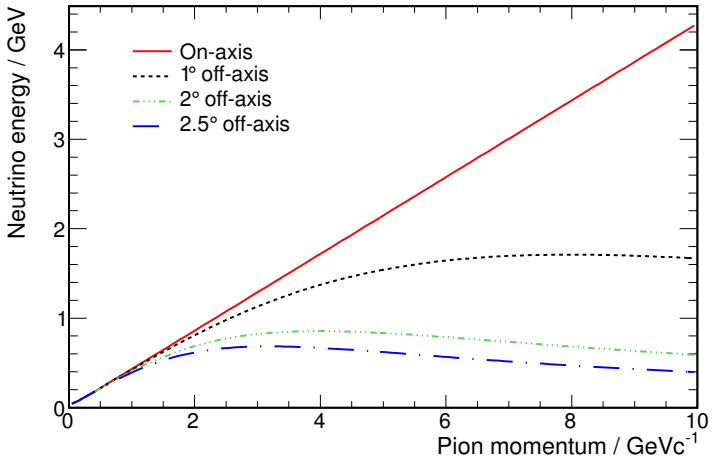

(a)

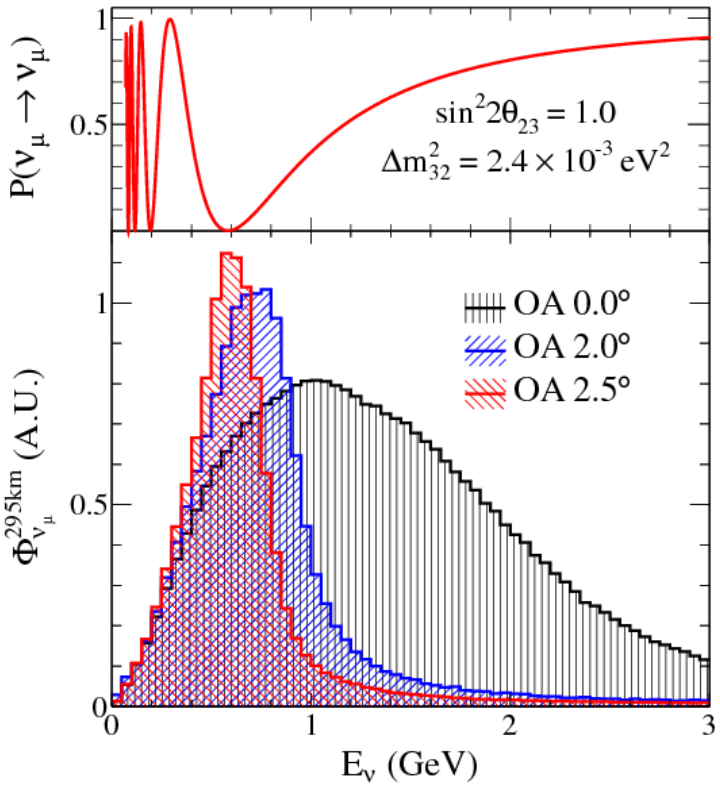

(b)

Figure 3.5: (a) Beam neutrino energy as a function of pion momentum and assuming four different off-axis angles; (b) Effect on the muon neutrino flux at Super-Kamiokande of changing the off-axis angle, and the muon neutrino survival probability as a function of energy. From [79].

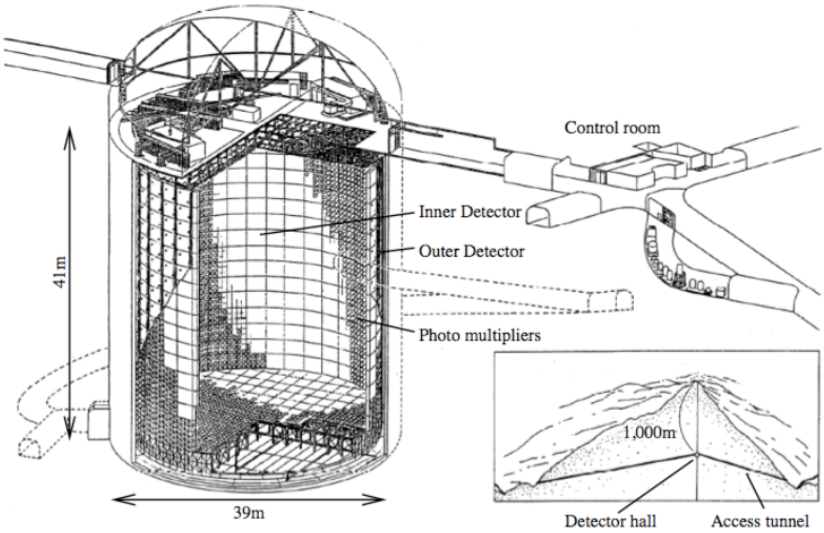

Figure 3.6: The T2K far detector, Super-Kamiokande. From [34].

becomes possible at higher energies (see Section 2.5). Removing higher-energy neutrinos, then, reduces this dominant background along with other backgrounds from resonance and DIS interactions.

3.3.2 Super-Kamiokande

Super-Kamiokande (SK) is the T2K far detector (Figure 3.6). With a 50 kiloton mass[3] and a cylindrical volume extending 41 m in height and 39 m in diameter, it is the world's largest land-based water Čerenkov detector, and is located within the mines under Mt. Ikenoyama near Kamioka, 295 km from the neutrino source, and approximately 2.5° off-axis.

SK is separated into independent inner and outer detectors by the insertion of a stainless steel structure. From this structure 11,129 high-gain photo-multiplier tubes (PMTs) of 0.5 m diameter face in to the 36.2 m height and 33.8 m diameter inner detector, giving a 40% coverage. The inner detector collects the primary beam neutrino sample. On the structure's exterior surface, a further 1,885 PMTs face out through the outer detector, which extends a further 2 m in the radial and axial directions. The outer detector was originally designed as a veto for cosmic ray muons, for which an almost 100% rejection efficiency can be achieved, but it is also used to study beam neutrino events that exit the inner detector.

[3] 22.5 kiloton fiducial mass.

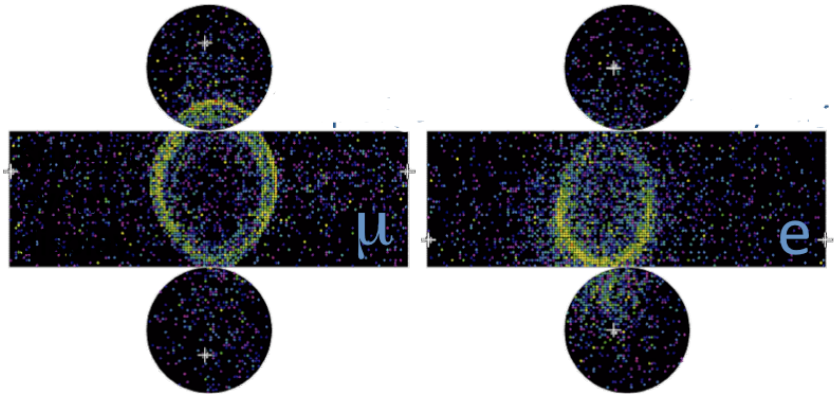

Figure 3.7: Muon (left) and electron (right) event displays at Super-Kamiokande. Images from [80].

SK can distinguish between electrons and muons, and hence the neutrinos producing these particles via the CC weak interaction, by studying the sharpness of the Čerenkov rings formed when the particle travels faster than the speed of light in the water of the detector; electrons generate less sharp rings as they electromagnetically shower in the water and their secondary particles contribute to the Čerenkov light (Figure 3.7). Importantly, neutral pions can often also be separated from the leptons by looking for two coincident electron-like rings, which would originate from the decay of the primary particle. Unfortunately however, the size of SK means that the use of a magnetic field is not possible. Consequently, neutrinos cannot be distinguished from antineutrinos at the far detector.

3.3.3 ND280

The T2K near detector, ND280, is located 280 m from the proton target and in the direction of the far detector. The ND280 is used to measure the initial flux component of the various neutrino flavours in the beam, and is also valuable for making neutrino-nucleon cross-section measurements at beam energies $\sim 1\,\text{GeV}$. Such measurements are important both within the T2K experiment for reducing the systematic error on the oscillation analyses originating in cross-section model uncertainties, and in the neutrino community in general; world neutrino cross-section data at these energies are currently very sparse, and are a requirement for any oscillation analysis.

The ND280 is a hybrid detector; its subdetectors are shown in Figure 3.8. The detector is split into two major regions: at the most upstream end is the π^0 detec-

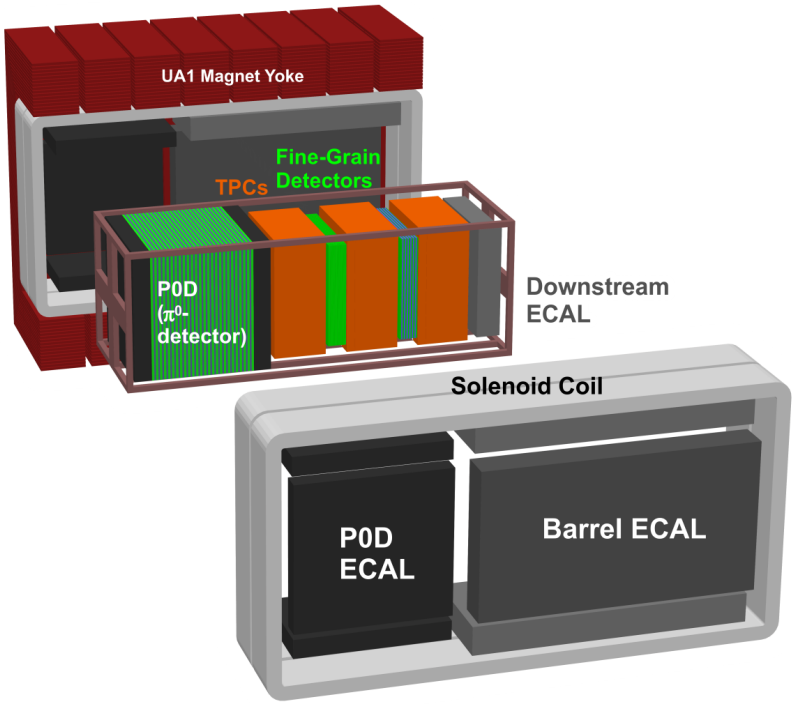

Figure 3.8: The T2K off-axis near detector, ND280. The T2K neutrino beam enters from the left of the diagram. From [34].

tor (P0D) and then immediately downstream lies the tracker, containing the two fine-grained detectors (FGDs) and the three time projection chambers (TPCs). Surrounding these regions are the electromagnetic calorimeter (ECal) modules, which are themselves encompassed by the UA1 magnet. Within the magnet yoke is the side muon range detector (SMRD).

The P0D, FGDs, and ECal modules are scintillating bar detectors, and are all read out via the same mechanism.

Scintillator bar readout

Each extruded scintillator bar contains a wavelength-shifting (WLS) fibre along its length. Scintillation light that travels along the fibre is read out at the end of the bar by a photosensor (Figure 3.9), the multi-pixel photon counter (MPPC).

A customised MPPC has been developed by Hamamatsu Photonics for the T2K experiment. Each MPPC is an array of 667 avalanche-photodiodes with an area of

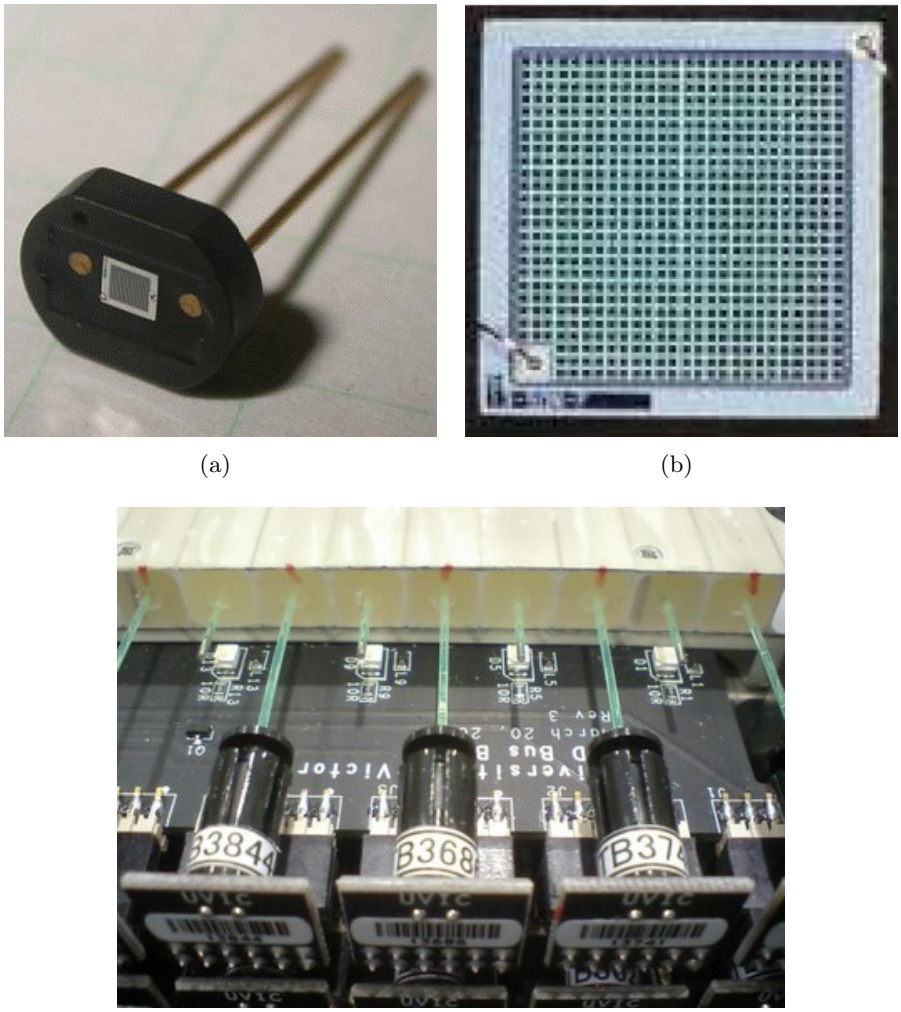

(a) (b)

(c)

Figure 3.9: (a) Photograph of the Hamamatsu multi-pixel photon counter (MPPC) used in the T2K experiment; (b), zoom of the active area of an MPPC; (c), MPPCs connected to wavelength-shifting fibres on a fine-grained detector. From [34].

$0.05\,\text{mm} \times 0.05\,\text{mm}$; a photon incident on the active pixel area creates an avalanche of electrons with a gain on the order of 10^6. The MPPCs were required to be built with the ability to operate in a 0.2 T magnetic field. Additionally, the fact that approximately 64,000 are needed necessitated that the MPPCs were developed with the requirements of low cost and high reliability.

π^0 Detector

At the most upstream end of the ND280 lies the π^0 Detector, or P0D, which is built with the primary purpose of constraining the major background to the ν_e appearance signal at SK:

$$\nu_\mu + N \rightarrow \nu_\mu + N + \pi^0 + X.$$

This scintillating bar detector is interleaved with 30 mm thick pockets that can be filled with water and drained for neutrino interaction studies on both water and air targets (Figure 3.10). This allows the neutral current π^0 production interaction, above, to be studied on the same target as that found at SK. Also interleaved between the scintillator bars are 1.5 mm thick brass sheets as a dense material to cause photons from the π^0 to shower, ensuring the possibility of reconstruction.

The scintillator bars themselves are triangular in cross-section in order to give a better positional resolution, with a 30 mm base and 15 mm height. The plastic bars are coated with TiO_2 and are extruded with a central hole running longitudinally in which a WLS fibre sits to transport the collected scintillation light to the MPPCs.

Fine-grained detectors

The two FGDs are also scintillating bar detectors (Figure 3.11). These detectors provide the target mass of the tracker region, each containing approximately 1 ton of target material. The upstream FGD, referred to as FGD1, provides the carbon target of its scintillator bars, and the downstream FGD, or FGD2, also contains six water targets, allowing direct comparison of interactions on carbon and oxygen. In addition, the scintillator bars provide high resolution tracking such that particles exiting an interaction vertex can be distinguished easily. Each scintillator is composed of plastic coated with TiO_2, 1843 mm in length and with a square cross-section of 9.6 mm $\times$ 9.6 mm. The WLS fibre threaded through the centre of each scintillator is attached to an MPPC at one end only, the other end being mirrored to minimise light loss.

FGD1 contains 30 layers of 192 of these scintillator bars, with layers alternating between horizontally and vertically orientated bars. FGD2 consists of 20 layers in total; the six 25 mm thick water targets are sandwiched between seven pairs of scintillator layers.

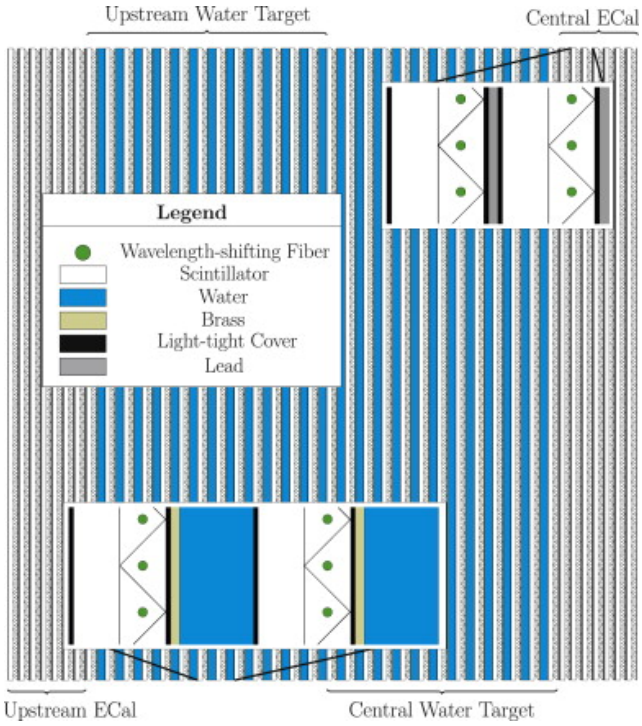

Figure 3.10: Schematic of the π^0 detector. From [34].

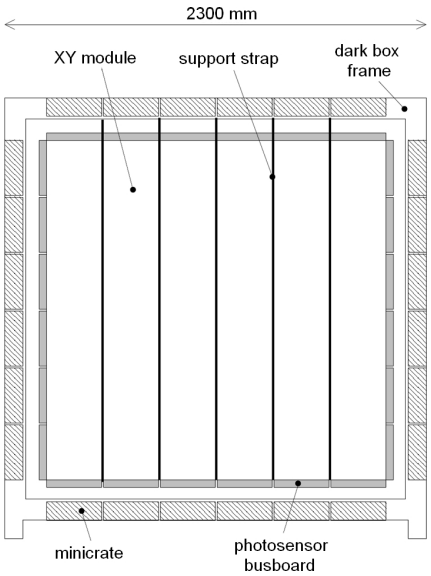

Figure 3.11: Cross-section of a fine-grained detector. From [81].

Time projection chambers

The three TPCs provide three-dimensional particle tracking with high precision. The particle curvature induced by the 0.2 T magnetic field allows momentum- and charge-measuring capability. Using the momentum calculation and the ionisation energy deposited, the energy loss of the particle can also be inferred. Comparing this to that expected from various particle types (Figure 3.12), it is possible to distinguish muons and pions from electrons and, at T2K's central neutrino energies, protons.

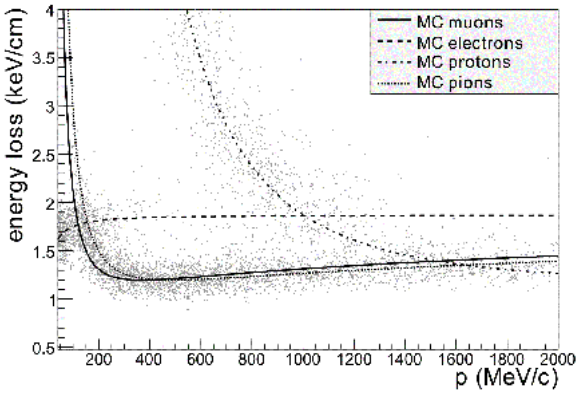

Figure 3.12: Particle energy loss as a function of momentum. Each point shows real data measurements by a single TPC of the energy loss and momentum of positively charged particles produced in neutrino interactions. The expected relationships for muons, positrons, protons, and pions are shown by the curves. From [34].

The 3000 l TPC volumes are filled mainly with gaseous argon. Traversing charged particles ionise the gas, and the liberated electrons drift towards the readout plane in the highly-uniform electric field. The three-dimensional nature of the readout is achieved by considering the drift times of the ionisation electrons as well as their position on the readout planes. A photograph and cutaway drawing of one of the TPCs are shown in Figure 3.13.

Electromagnetic calorimeters

The ECal consists of 13 separate modules: six barrel and six P0D ECal modules, which are mounted within the UA1 magnet, and the downstream ECal (DsECal), which is located at the most downstream end of the detector. This gives ECal coverage across the whole inner region of the ND280, for the detection and energy

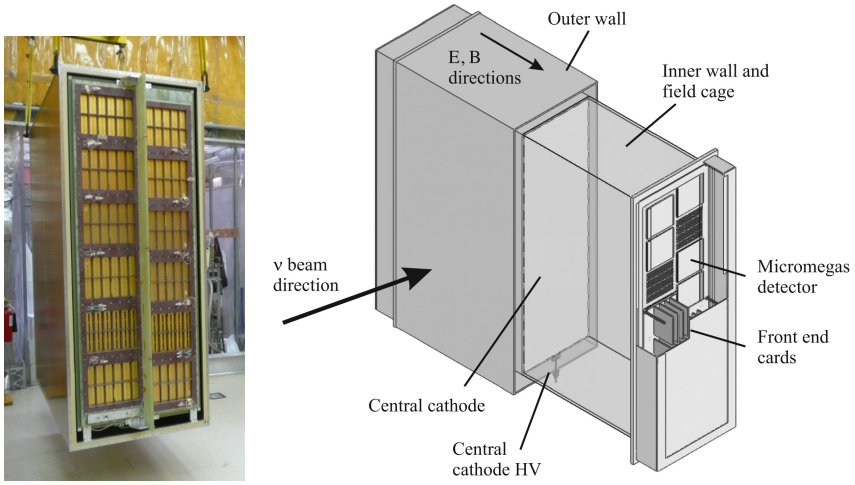

(a) (b)

Figure 3.13: (a) Photograph of one of the TPCs, and (b) cutaway drawing of the main aspects of the TPC design. From [34].

measurement of escaping photons from π^0 decay in particular, but also providing particle identification additional to that provided by the TPCs. The ECal can distinguish showering charged pions from muons, for example.

The sampling calorimeter modules are composed of 1.75 mm[4] thick lead sheets interspersed with layers of polystyrene[5] scintillator bars (Figure 3.14). Each layer of scintillator bars is rotated by 90° with respect to the previous layer. This provides two orthogonal 'views', which can be combined with hit times to enable three-dimensional reconstruction. Each scintillator bar has a 40 mm × 1 mm cross-section and is extruded with a 2 mm × 3 mm elliptical hole running longitudinally for the insertion of a WLS fibre.[6] The longer bars are read out at both ends. Shorter bars can be efficiently read out with an MPPC at only one end with the other end being mirrored to minimise light loss. Module specific readout, bar dimension, layer and orientation information is summarised in Table 3.3.

Magnet

The ND280 subdetectors are surrounded by the reused CERN UA1/NOMAD magnet, as is shown in Figure 3.15; the 0.2 T horizontally-orientated dipole field gen-

[4] 4 mm thick in the P0D ECal.

[5] Doped with 1% PPO (2,5-DiPhenyloxazole) and 0.03% POPOP (1,4-Bis(5-phenyl-2-oxazolyl)benzene) by weight.

[6] Kuraray Y-11(200)M, CS-35J.

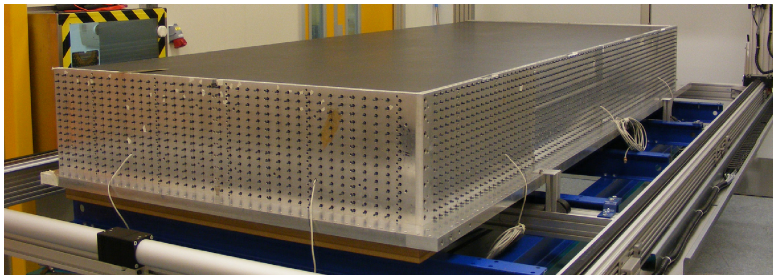

(a)

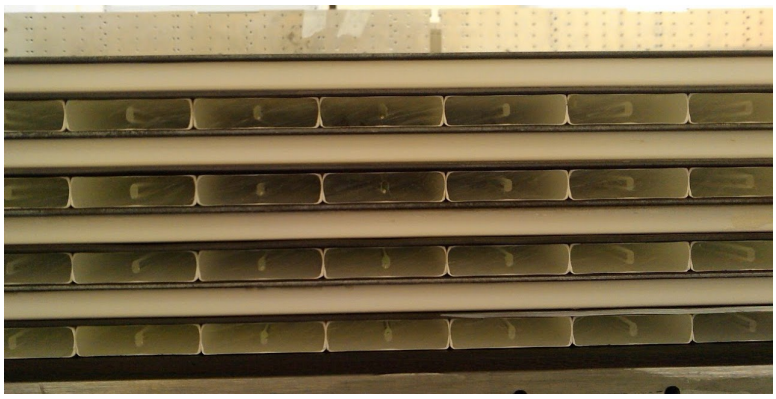

(b)

Figure 3.14: (a) Photograph of one of the top barrel ECal modules during construction. From [82]; and (b) ECal bar ends showing the inserted WLS fibres. From [34].

Module	View	Layers	Bars / layer	Bar length (m)	Double-ended readout?
P0D side	YX	6	69	2.34	N
P0D top/bottom	XY	6	38	2.34	N
Barrel side	YX	15	57	3.84	Y
	ZX	16	96	2.28	N
Barrel top/bottom	XY	15	38	3.84	Y
	ZY	16	96	1.52	N
DsECal	XZ	17	50	2.00	Y
	YZ	17	50	2.00	Y

Table 3.3: ECal module specific readout, bar dimension, layer and orientation information.

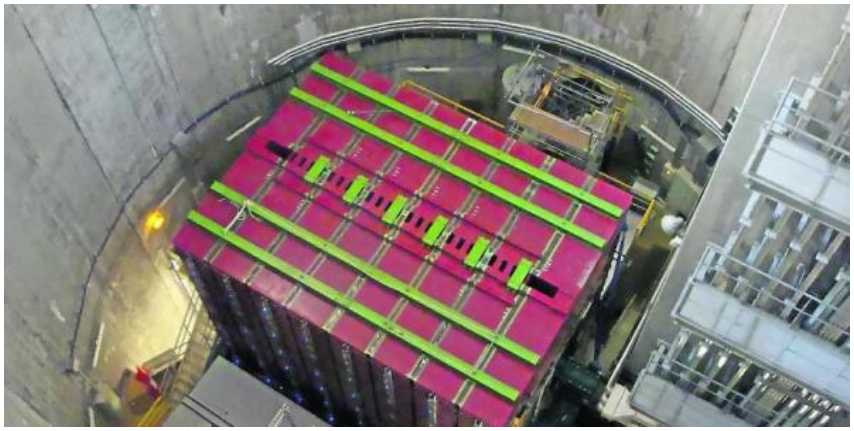

Figure 3.15: Photograph of the ND280 with the magnet closed.

erated makes possible charge and momentum measurements from the curvature of tracks.

The 850 ton, 7.6 m × 5.5 m × 6.1 m magnet requires a current of 2.9 kA which passes through its aluminium coils. These coils are composed of bars with a square cross-section of side 54.5 mm, and a central hole of 23 mm diameter such that they can be water-cooled to approximately room temperature.

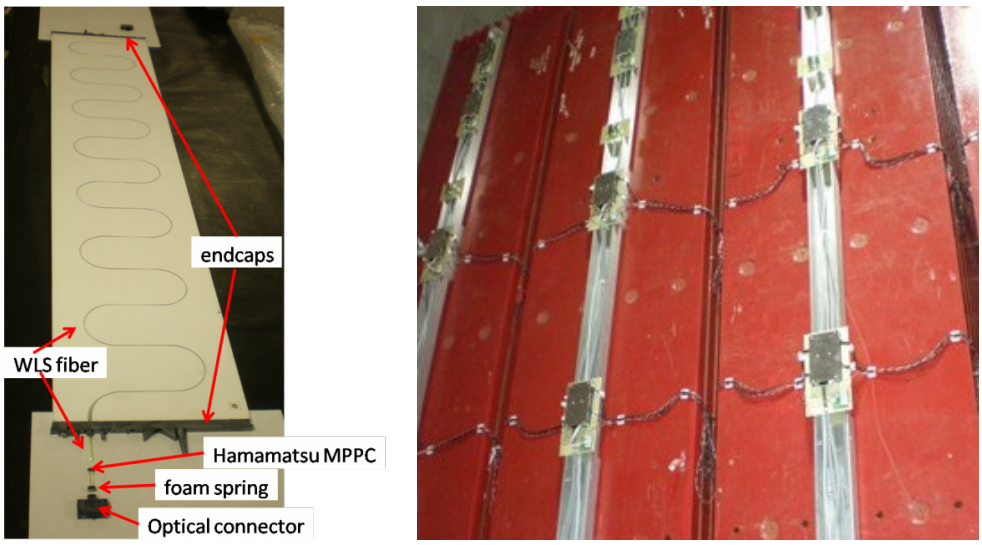

(a) (b)

Figure 3.16: (a) Photograph of an SMRD panel showing the S-shaped WLS fibre and connection to Hamamatsu MPPC. Image from [34]; and (b), some SMRD panels in situ. It can be seen that the panels fit within the magnet flux return yokes. Image from [83].

Side muon range detector

The SMRD instrumentation is inserted within the UA1 magnet flux return yokes (Figure 3.16(b)), and is designed to veto beam-induced neutrino interaction events entering the ND280 from the walls of the near detector complex and to identify high-angle muons from beam interactions within. Location within the magnet allows muon energy measurements, as significant ionisation energy loss occurs when traversing the iron yokes. The SMRD is also used as the main trigger for cosmic event recording within the ND280.

The instrumentation is composed of 440 scintillating panels 875 mm in length and with varying widths. However, the width of each panel is such that a WLS fibre inserted through the centre would collect insufficient light; instead a 2.55 m long WLS fibre follows an S-shaped groove along the length of each, as can be seen in Figure 3.16(a).

The scintillator panels are arranged into eight sets on each side of the magnet. The sets running along the top and bottom of the magnet each consist of three scintillator layers. The first five along the sides also contain three layers, whilst the most downstream three contain 4, 6 and 6 layers respectively. This design maximises

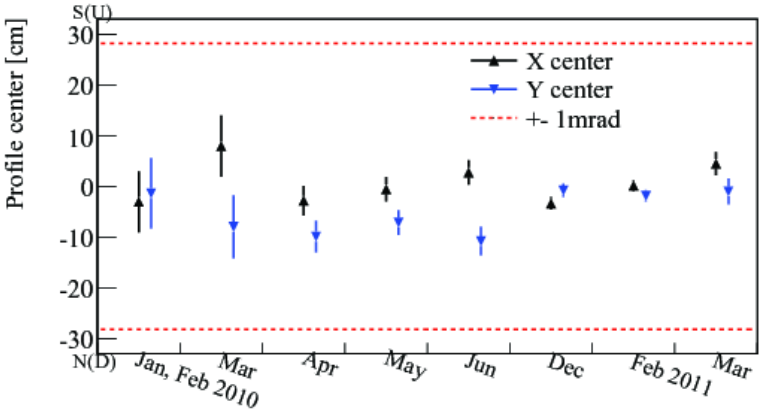

Figure 3.17: Beam stability in the vertical and horizontal directions as measured by INGRID during T2K runs 1 and 2. From [84].

the instrumentation in the area with the highest population of muons from beam interactions within the ND280 target volume.

3.3.4 INGRID

The Interactive Neutrino GRID (INGRID) is the T2K on-axis near detector, located within the same complex as the ND280. The detector is composed of 14 iron-scintillator modules arranged in a cross shape such that the central module is directly along the beam axis (defined as the direction of the primary proton beamline), and two additional modules resting upon the horizontal 'arms' of the cross (Figure 3.18(a)). Iron targets at this distance of 280 m from the neutrino source ensure sufficiently high neutrino interaction rates for the beam intensity to be monitored on a daily basis, and the large extent of the detector ($\sim 10\,\text{m} \times \sim 10\,\text{m}$), owing to the optimised shape, allows the beam direction and spread to also be monitored. Furthermore, the two modules in diagonal positions allow monitoring of the axial symmetry of the beam. Constant monitoring of these attributes of the beam is essential; as shown previously in Figure 3.5(b) the energy spectrum seen in the off-axis detectors changes considerably for a small change in angle. Figure 3.17 shows an example of the monitoring of the beam direction performed by INGRID. The beam direction can be seen to be stable across the first T2K running period to within $\pm 10\,\text{cm}$.

An INGRID module consists of nine layers of iron plate sandwiched between eleven

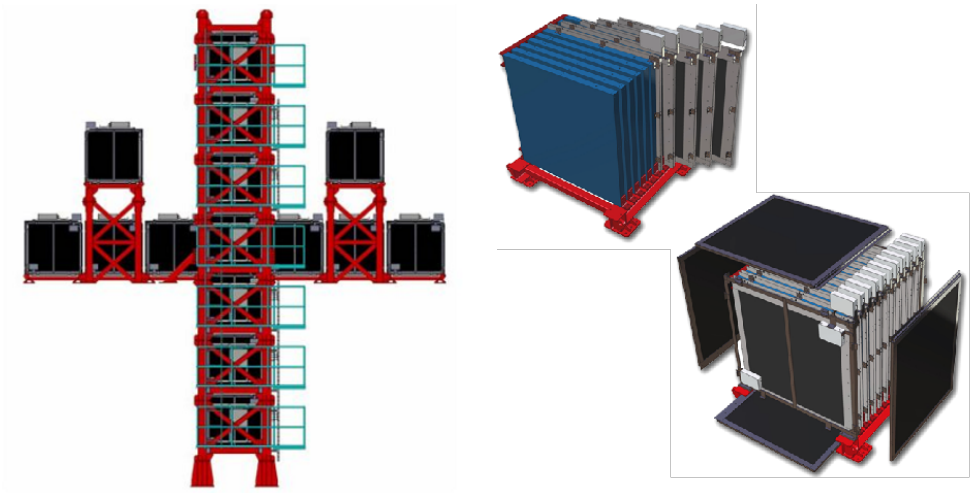

(a) (b)

Figure 3.18: (a) The T2K on-axis near detector, INGRID. In the figure, the T2K beam is orientated such that it enters the page with the central module directly along the beam axis; (b) An example of an INGRID module. The top image shows the iron plates and polystyrene scintillator planes, and the bottom image shows the encasing veto planes. From [34].

polystyrene[7] scintillator planes. In addition to this, there is a scintillator plane surrounding each module to be used as a veto of interactions originating externally. A module contains 7.1 tons of iron target, with each target layer extending 1.24 m in the x- and y-directions, and 65 mm in the beam direction. The scintillator planes are composed of 24 bars in the horizontal direction, followed by a further 24 in the vertical direction. Each of these bars has a 10 mm × 50 mm cross-section, through the centre of which 1 mm diameter WLS fibres transport the scintillation light to MPPCs, in much the same manner as the ND280.

Whilst increasing the event rate sufficiently for daily monitoring, the thick iron plates have the disadvantage of allowing only muons to penetrate to the scintillator and be reconstructed, meaning that INGRID could not initially distinguish CCQE from other CC interactions. For this reason, an extra module, with no iron planes and smaller scintillator bars, was added to the central crossing point of the existing detector. Its smaller bars allow the reconstruction of recoil protons so that a separate CCQE measurement can be made.

[7]Doped with 1% PPO and 0.03% POPOP by weight.

Chapter 4

The ND280 Electromagnetic Calorimeter in the T9 Testbeam

The T2K near detector, ND280, utilises an ECal surrounding the inner P0D and tracker regions, as discussed in Chapter 3. The ECal is an important subdetector for many interactions to be studied at the near detector. Indeed, for the analysis described in Chapter 5, it will be shown that it is vital in selecting the interactions of interest in a sufficiently efficient and exclusive way.

It is therefore crucial that the ECal is well understood. For this purpose, in 2009 the DsECal was taken to the T9 testbeam at CERN, the European Organization for Nuclear Research, for calibration and performance studies.

4.1 The T9 Testbeam

The CERN T9 beamline [86] is a secondary beam created by the collision of protons from the CERN proton synchrotron. It provides a monochromatic beam whose momentum can be tuned within the range 0.3 GeV to 15 GeV. Bending magnets are used to concentrate the beam on a focal point within the experimental area and the current within these magnets can be reversed to provide particles of opposite charge. The positive polarity beam consists primarily of positrons, which dominate at momenta below 1.5 GeV, and an increasing component of charged pions and protons as momentum is increased. The negative polarity beam consists mainly of electrons and negative pions, again with the lepton dominating at momenta below 1.5 GeV. The beam composition is shown as a function of momentum in Figure 4.1.

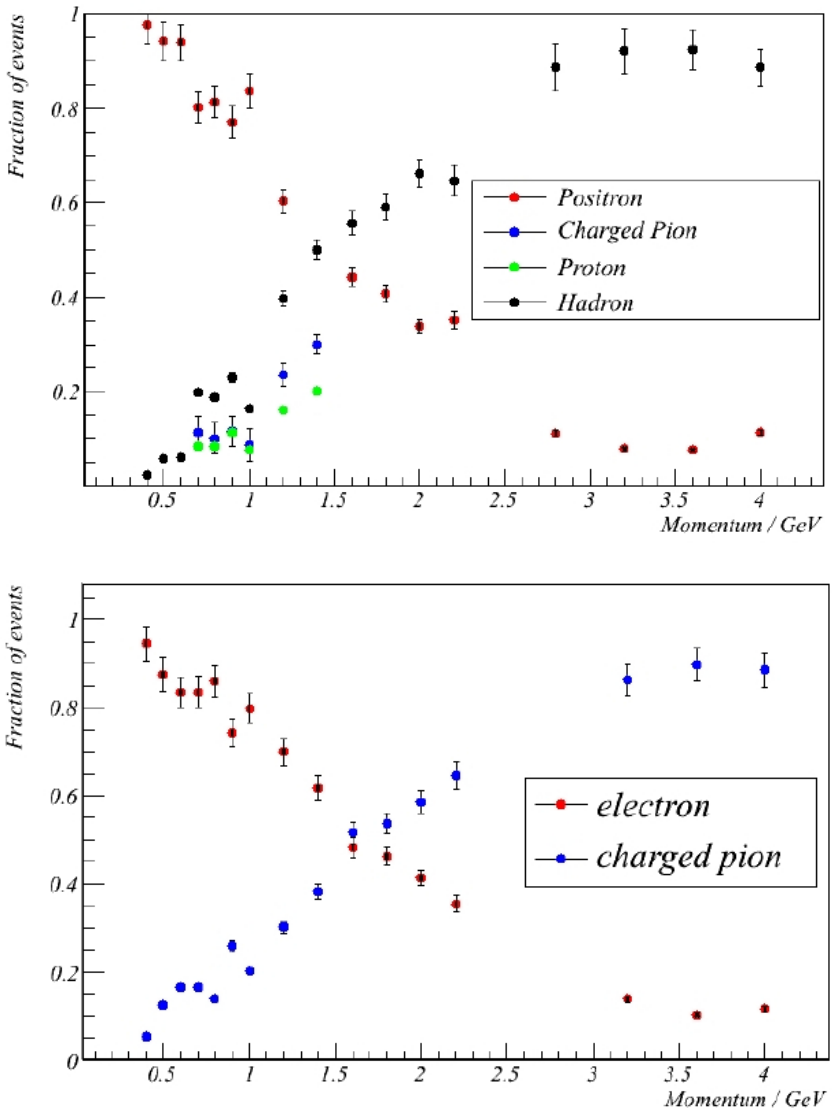

Figure 4.1: CERN T9 testbeam composition as a function of momentum in (top) positive and (bottom) negative polarity mode. Figure taken from [85].

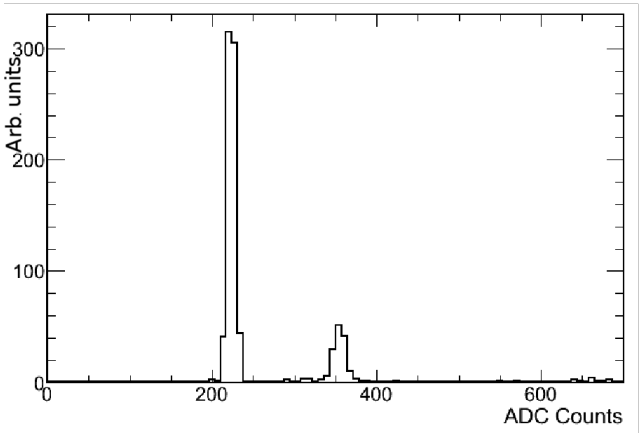

Figure 4.2: TOF signal for a positive polarity run at the testbeam. The larger peak is the signal from electrons/pions and the smaller peak is from protons.

Both polarities also contain a small fraction of muons from pion decay within the beam that are categorised as pions in the figure.

4.2 Particle identification

Three systems were used and combined in order to identify the testbeam particles independently of the DsECal: two CO_2-filled Čerenkov counters set at a pressure such that only electrons/positrons were above threshold, and a time-of-flight (TOF) detector with a 14 m flight distance. The Čerenkov counters were required to agree on the existence of a signal in order for a particle hypothesis to be accepted. Pions should not give a signal in the Čerenkov counters, but should look similar to electrons/positrons in the TOF detector as opposed to the more massive protons, allowing the separation of these hadrons.[1] The TOF signal for an example positive polarity run showing the electron/pion and proton peaks is shown in Figure 4.2. The muon contamination due to the decay of pions in the beam was indistinguishable from the pions themselves; studies suggest that this contamination may be approximately 10% at beam energies below 1 GeV but drops to less than 1% above 2 GeV [85]. The various particle identification combinations and the resulting particle hypotheses are given in Table 4.1.

Using these detectors, it has been estimated that the sample of hadrons is contaminated with electrons by less than 0.5%, and the electron sample is greater than 99%

[1] This is possible up to approximately 1.8 GeV. Above this momentum only an electron/hadron separation was possible.

pure [82].

4.3 Data taking

Due to transportation constraints, the detector was placed in the beam with the downstream end (in the J-PARC configuration) facing towards the incoming particles, meaning that a lead layer was the first to be encountered, as opposed to a scintillator when included as part of the ND280. The beam momentum of the runs ranged between 0.3 GeV and 5 GeV, providing data spanning the most useful energies for the T2K experiment, and the angle of incidence was varied between $0°-60°$ in the horizontal plane, on a run-by-run basis. In addition, beams of positive and negative polarity were used to broaden the number of particle varieties available.

Due to their MIP[2]-like nature, cosmic ray muons can be relatively easily simulated and are therefore very useful for charge calibration. For this reason, between beam spills the detector also registered cosmic ray muons in the upright position. Finally, the DsECal was laid on its front face (so that the majority of the flux again came through the downstream face) in the experimental hall in order to register a further sample of cosmic ray muons. The collection of cosmic data in an upright and flat position allowed for useful comparisons of charge deposit based on particle angle of incidence.

Beam polarity	TOF	Čerenkov 1	Čerenkov 2	Particle
-	EM	Yes	Yes	e^-
+	EM	Yes	Yes	e^+
-	EM	No	No	π^-
+	EM	No	No	π^+
+	Proton	No	No	p^+

Table 4.1: A list of the different particle identification combinations and the resulting particle hypotheses.

[2]Minimally ionising particle. Muons with energies in the cosmic ray region experience ionisation energy loss when traversing matter at a lower rate compared to other particles.

4.4 Calibration

An ECal should provide precise energy measurements, so good calibration procedures are required. The energy calibration process for the ND280 ECal works from the TFB electronics through to MPPC calibration and on to the scintillator bars. Firstly a subtraction of the electronics pedestal value from the registered ADC (analogue-to-digital converter) counts is made. This pedestal value, the number of ADC counts registered when no physics signal is present, varies due to changes in the surrounding temperature, so frequent pedestal measurements are necessary if the temperature fluctuates constantly. Additionally, temperature changes affect the MPPC gains so this must also be calibrated out. The MPPC gains are found by fitting the first non-pedestal peak in the noise spectra used in the pedestal subtraction, which gives the charge due to the firing of a single MPPC pixel. Finally, a calibration must be made to account for the individual differences in the scintillator bars and WLS fibres and their couplings to the electronics. As stated in the previous section, cosmic ray muons are useful for this stage of calibration. High statistics samples of cosmic ray muons are taken, and the hit charge distributions in each bar are recorded. Muon path-length differences through the scintillator and attenuation in the WLS fibres are corrected for and then all channels are normalised so that hits in all bars are registered at the same level. This is done by fitting a Landau-Gaussian function to the hit charge distribution. The Landau distribution describes the ionisation energy loss of particles traversing through matter [87], resembling a Gaussian with an extended upper tail to represent rare high energy-loss collisions. The Landau distribution is convolved with a Gaussian which describes the statistical smearing due to the finite resolution of the detector. The most probable value (MPV) of the underlying Landau distributions for every channel give the expected ionisation energy deposited by a MIP traversing the scintillator bar at a distance of 1 m from the sensor. The distributions are all scaled so that the MPVs appear at one, defining the MIP equivalent unit (MEU). The mean of the Landau-Gauss distribution can be sensitive to the rare high energy collisions, so the MPV, which is the modal energy loss, or peak of the distribution, is used as a more stable measure than the mean.[3]

[3]Indeed, the ideal Landau distribution has no defined mean.

Testbeam data calibration

During testbeam running, the ECal was cooled with a system that provided less efficient cooling than is provided at J-PARC. The large changes in temperature experienced at the site could not be fully overcome by this cooler and so the average temperature of the detector exhibited diurnal variation on the order of 2°C, resulting in a variation in average MPPC gain. Dedicated pedestal runs were taken at the tesbeam site, but, unlike when situated at J-PARC, no pedestal data were taken during physics running, and no noise spectra were measured. As opposed to the MPPC calibration described above, therefore, the temperature of the detector was measured using LM92 chips placed close to the MPPCs, and this measurement was used to conduct a simple linear MPPC gain correction. The gain for each run was calculated using the previous pedestal run, and corrected for by the rate of change of gain with temperature:

$$G = G_0 + \frac{\mathrm{d}G}{\mathrm{d}T} T_{\mathrm{diff}} \tag{4.1}$$

where G_0 is the gain of the previous pedestal run, T_{diff} is the temperature difference between the current run and the previous pedestal, and $\frac{\mathrm{d}G}{\mathrm{d}T}$ is the rate of change of gain with temperature, which was measured to be $-0.67 \pm 0.07/°\mathrm{C}$ [88]. In order for this correction to be more successful, pedestal runs were increased in frequency after some time, and the MIP response became more stable. Figure 4.3 shows the Landau MPV for muon hits during testbeam running and after the simple linear temperature correction. The vertical dashed line corresponds to the date when regular pedestal runs started to be taken.

In addition to the hit charge calibration, a correction is made to the hit times. The peak values of horizontally and vertically oriented hits are offset in time by values on the order of 10 ns but varying slightly between runs. The peak values were found for each run using a Gaussian fit and the vertically orientated bar hits were translated in time in order that the peak times matched. After this correction, the timing itself can be used to remove most contaminating hits. Due to the lack of overburden at the CERN testbeam experimental hall, the testbeam data was heavily contaminated with cosmic ray muons, resulting in a peak in the single hit charge distribution corresponding to ionisation energy deposits from the MIP-like particles, as can be seen in Figure 4.4. The majority of these contaminating hits can

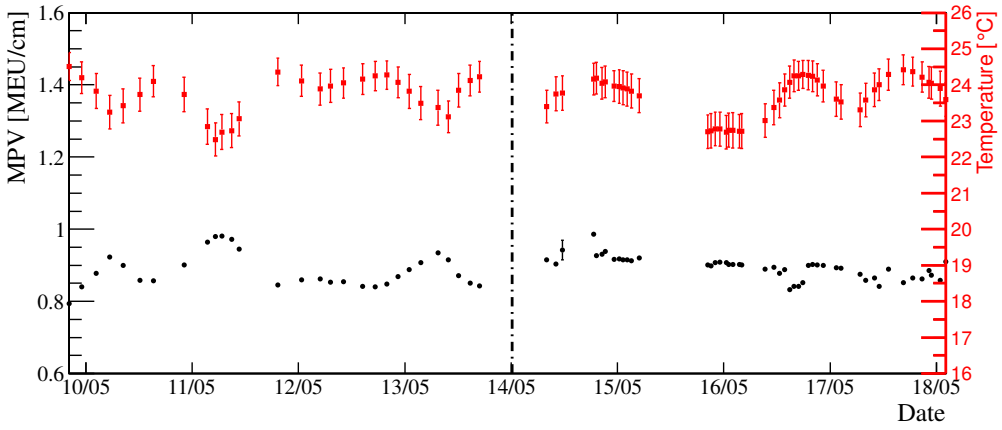

Figure 4.3: Average MPPC temperature during a selection of testbeam runs and Landau most probable values of hits from muons during that period. A simple linear temperature correction has been applied. The dashed vertical line corresponds to the date when regular pedestal runs began.

be removed by requiring the hits to be registered within a loose time window. The average cluster time with respect to the trigger was recorded and any hits further than $8\,\sigma$ from this average time were removed.

Finally, a discrepancy at low hit charges is removed. MPPCs, as with any photodiode, can fire without stimulation. This dark noise registers at low charge and the rate differs from chip to chip. Additionally, a chip to chip variation in gain is seen (even at stable temperatures), which means that the threshold for registering hits differs, effectively smearing the threshold at the lowest values where the noise hits reside. Figure 4.5 shows this effect in comparison to the near flat cut-off seen in the default simulation. A full simulation of the effect of these characteristics would require a chip-by-chip calibration, but the design did not allow access to individual chips. Instead, an artificial flat threshold was implemented in data and simulation at a value of 0.4 MEU.

4.4.1 Monte Carlo simulation

Calibrated real data was compared to Monte Carlo simulation in order to analyse the performance of the detector and the simulation itself. Due to the difference in surrounding conditions compared to that at the ND280 pit at J-PARC, a special simulation was required for this purpose, with features that varied for comparison to different testbeam runs.

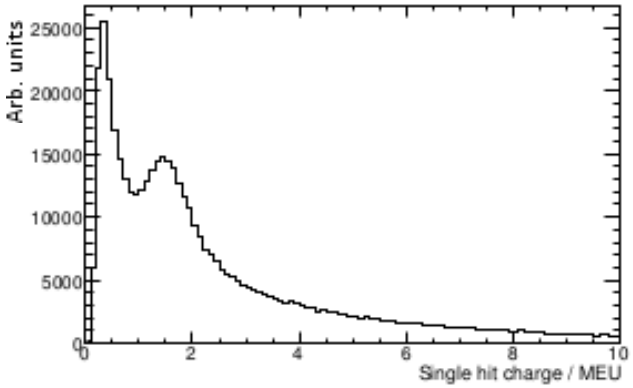

Figure 4.4: Single testbeam run hit charges, showing MIP peak from contaminating muons. After charge calibration the MIP peak would appear around 1 MEU.

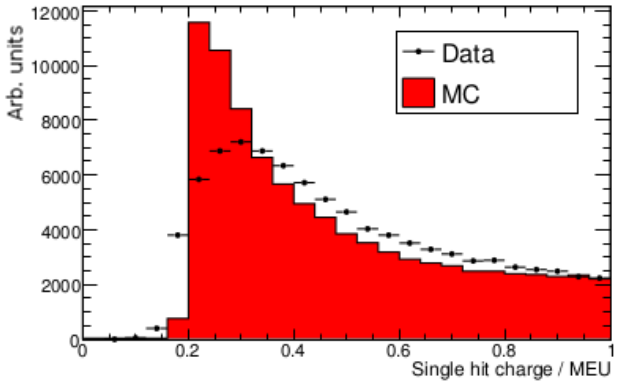

Figure 4.5: Single testbeam run hit charges. Varying chip thresholds in real data cause a smeared cut-off at the lowest charges, whereas a simple flat cut-off is simulated. Real and simulated data are normalised to area.

A representation of the DsECal geometry was constructed and GEANT [89] was used to simulate the passage of the particles through the detector. For each run, a simple cosmic simulation was processed, consisting of 10000 high energy muons fired at varying angles into the back face of the DsECal. In order for temperature effects to be eliminated as far as was possible at this stage, the temperature settings for the simulated MPPCs were set to their average temperature during the run, as recorded by the LM92 chips placed near them. This was done by fitting a Landau-Gaussian function to the hit charge distribution. The hit charges were scaled such that the MPVs of the underlying Landau distributions were the same as the MPVs in the interspill cosmic data.

A monochromatic 10000 event electron sample was then generated at the same

momentum as the central beam momentum in the real data run, and at the same angle of incidence to the back face of the detector. Again the simulated photosensor temperature was set to the temperature of the photosensors recorded by the LM92 chips. At this stage of processing, the artificial 0.4 MEU charge threshold discussed at the beginning of Section 4.4 was implemented prior to any attempt at clustering the hits by the reconstruction package, so that the data and simulation were as similar as possible. The output of this simulation was then compared with the real data to assess both the detector performance and to get a handle on how well the detector was simulated in this environment.

4.5 Performance

The ND280 ECal should aid in the reconstruction of many neutrino event types, including the events described in the analysis in the following chapter. Another particularly important example is the major background to the electron neutrino appearance oscillation analysis: neutral-current π^0 production (see Section 3.3.1). Events such as this require both good angular and energy resolution in the ECal; often the photons from the π^0 decay will convert in ECal modules on opposite sides of the detector. Good directional determination of the photons will result in a precise location for the interaction vertex, and good energy resolution will allow the reconstruction of a sharp π^0 invariant mass peak, identifying the interaction. When the DsECal is included as part of the ND280, most particles will enter at, or close to, normal incidence to the detector face; for this reason, the performance was determined for 0° particles where possible.

Basic distributions such as cluster charge and size characteristics are useful to ensure that the simulation is accurate in modelling the data at the lowest level. Figure 4.6 shows comparisons of the number of hits contained in a cluster and the number of layers hit by a cluster for electrons of energy 600 MeV (top) and 1 GeV (bottom). It can be seen that the agreemeent is, in general, very good, although a slightly lower tail is seen in the real data. This originates in events where clusters from a single particle are split into two due to the fact that hits with charges less than 0.4 MEU are removed to improve the threshold issue mentioned previously.

The angular resolution was determined for electrons with energies between 400 MeV and 2 GeV, and compared to that predicted in simulation, as shown in Figure 4.7. The resolution quoted is the width of a Gaussian fit to the reconstructed angle

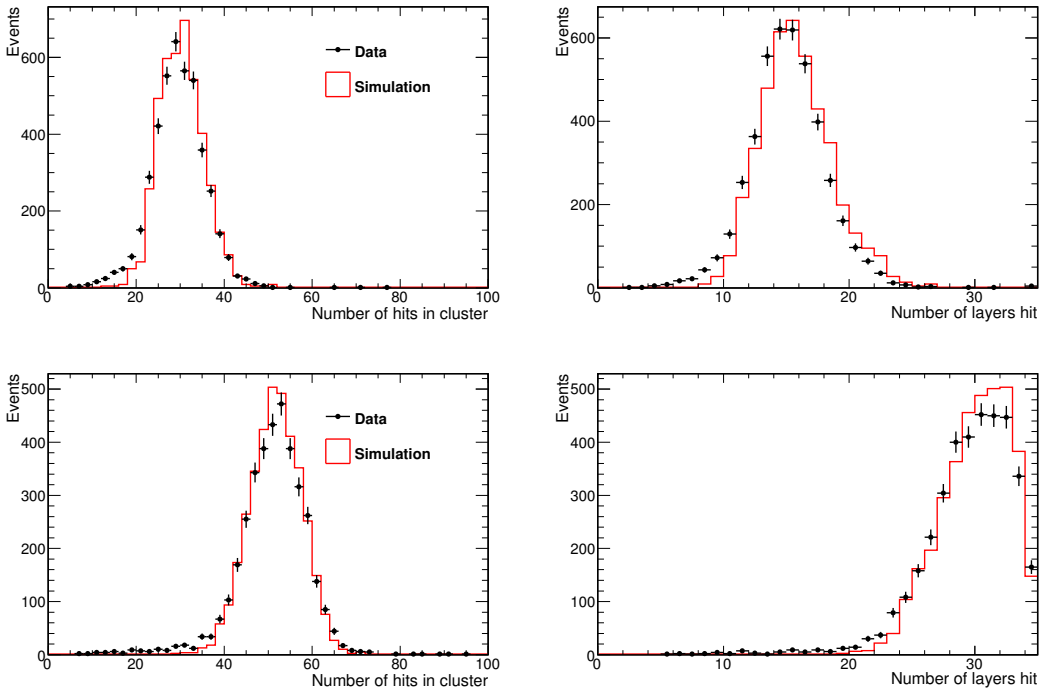

Figure 4.6: Real data and simulation comparisons of number of hits in a cluster and number of layers hit for (top) 600 MeV and (bottom) 1 GeV electrons.

distribution, where the angle is reconstructed using a principal components analysis method in the ND280 software package. Good angular resolution is observed ($\approx 4^\circ$ at 1 GeV) and there is excellent data-simulation agreement across the energy range analysed.

The energy resolution was determined using electrons incident at 30° to the back face of the DsECal. This is because, as stated in Section 4.4, it is at this stage that regular pedestal runs started to be taken, giving a more accurate energy resolution determination compared to what would be achievable as part of the ND280. The resolution was determined for electron energies between 300 MeV and 2 GeV by taking the width of a Gaussian fit to the energy distribution.

The electron energy resolution can be seen in Figure 4.8. A systematically wider resolution is seen in the data compared to the simulation, which can be explained by a number of contributing factors. The theoretical energy resolution of the CERN T9 testbeam is ±1.1% [90], whereas the simulated electrons are monochromatic. A study of the energy response of simulated electrons centred at 1 GeV with a 1.1% energy spread showed an approximately 1% larger width than for monochromatic

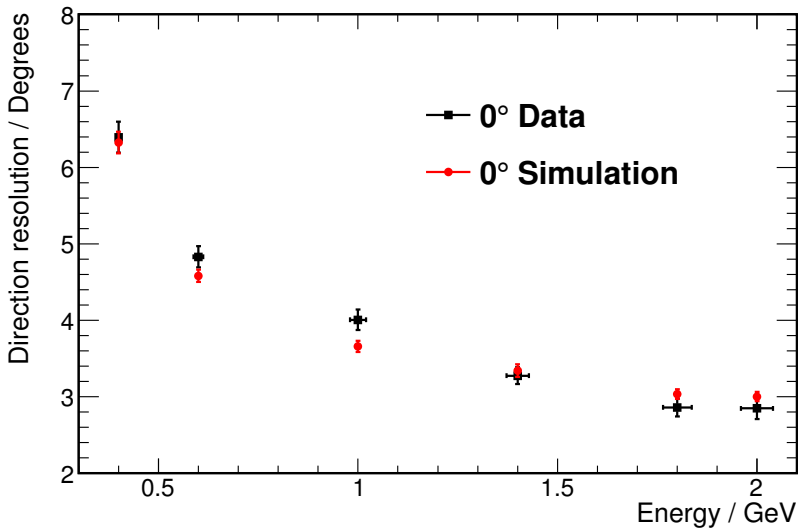

Figure 4.7: Angular resolution of electron showers in real data and simulation. The electrons are normally incident on the detector for a range of energy values.

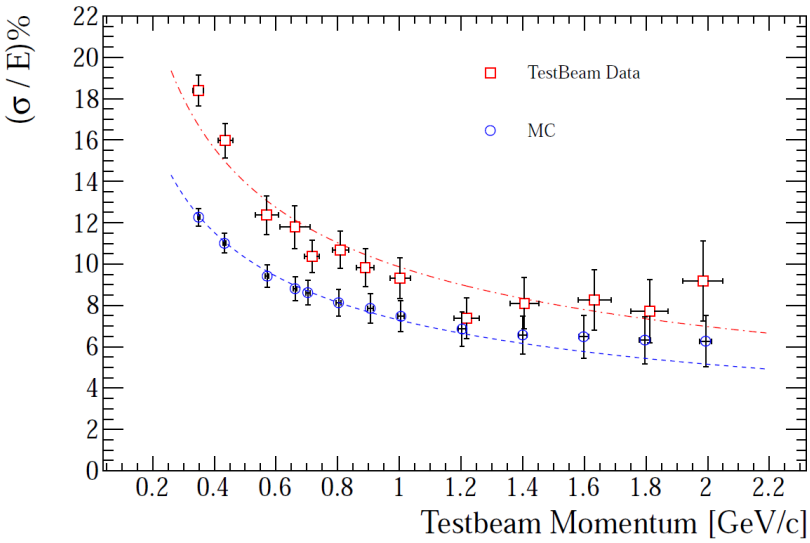

Figure 4.8: Energy resolution for electromagnetic showers, in real data and simulation. The dashed lines show a fit to a stochastic resolution model. Figure from [82].

electrons at this energy, suggesting that testbeam energy spread contributes to the wider resolution. However, the major contribution comes from the lack of modelling of individual sensor temperatures, as described in Section 4.4.

After various testbeam calibrations, the simulation of the detector generally models the detector response to electrons very well in cluster shape variables such as size and direction. However, due to imperfect cooling, the detector response varied with time, and the charge scale changes resulting from this cannot be calibrated out fully. This leads to an energy estimate that systematically differs between data and simulation. This difference is understood, however, and it can be concluded that the ECal can perform at a high level to make a significant and important contribution to the reconstruction of neutrino events at the near detector site.

Chapter 5

Muon Antineutrino Charged-Current Inclusive Cross-Section

5.1 Introduction

The T2K muon neutrino beam contains a contamination of approximately 6% muon antineutrinos (see Figure 5.1). As discussed in Section 2.5.3, although precise knowledge of neutrino-nucleon interactions is required for the study of $\mathcal{CP}$ violation at accelerator experiments, cross-section data, especially for antineutrinos, are very sparse at energies $\sim 1\,\text{GeV}$. The T2K experiment therefore provides the perfect opportunity to contribute to the measurements currently being made to more fully understand these interactions.

To this end, the objective of the analysis presented in this chapter is to measure the flux-integrated $\bar{\nu}_\mu$ CC inclusive cross-section on the FGD1 carbon-based target of the T2K ND280.

5.2 Data sets, Monte Carlo simulation, and software productions

The analysis shown here uses data collected during the T2K runs from November 2010 - March 2011 (T2K run 2), from March 2012 - June 2012 (T2K run 3b/c), and

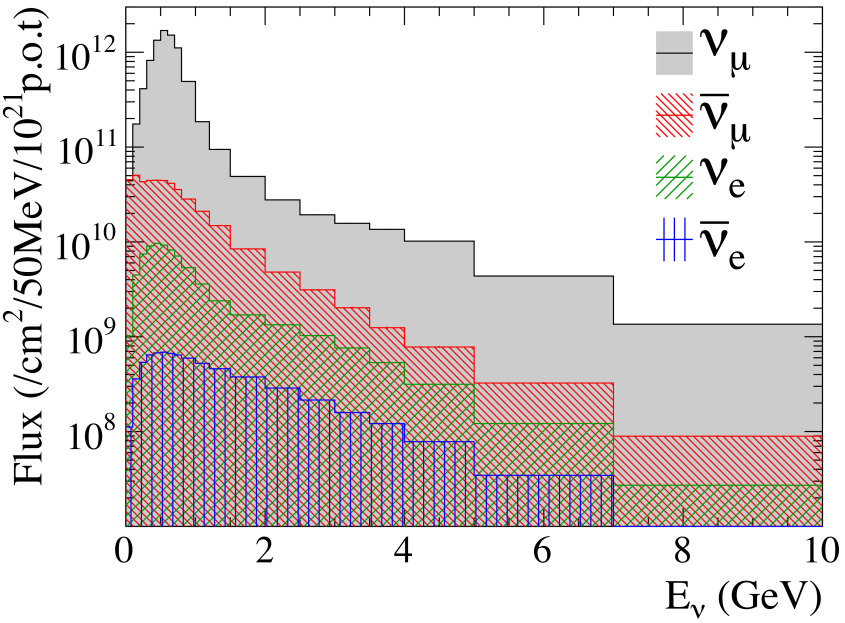

Figure 5.1: T2K combined run 1-4 flux prediction of neutrino flavours at ND280. Figure from [80].

from October 2012 - April 2013 (T2K run 4). Data from T2K run 1 was not used as the barrel ECal modules had not then been installed,[1] and run 3a was not used as the magnetic focussing horns were turned off during this period, resulting in a different neutrino flux.

The NEUT neutrino interaction generator [70] is used to produce the simulation of the full-spill beam data. Flux tuning files are used to reweight the nominal NEUT output to simulate more accurately the flux as it is during a specific run period. Individually tuned JNUBEAM simulations are provided for T2K run 2, run 3b, run 3c, and run 4 [91].

The output of this production is propagated through the detector simulation using GEANT [89], before processing through the electronic simulation. Both the real and simulated data then go through the same reconstruction chain within the ND280 offline software, before being processed through the package oaAnalysis, which stores the track-level global reconstruction quantities required. The selection of events is performed on the output of these files using the highland framework developed by T2K collaborators. Highland (high level analysis at the near detector) is a framework

[1] It will be shown later that information from the ECal modules is a major contributor to the effectiveness of this analysis.

T2K run	ND280 runs	Real data POT/10^{19}	Simulation POT/10^{19}	Sand sim. POT/10^{19}
Run 2(water)	6462–7663	4.31	43.1	8.65
Run 2(air)	7665–7754	3.57	35.7	7.15
Run 3b	8309–8453	2.26	22.6	4.55
Run 3c	8550–8753	13.72	137.2	27.50
Run 4(water)	8995–9422	16.52	193.4	33.15
Run 4(air)	9423–9722	16.95	14.13	34.00
Total:		57.33×10^{19}	573.3×10^{19}	115.0×10^{19}

Table 5.1: The number of protons on target of both real data, and NEUT full spill and sand simulation.

now used by most ND280 analyses; its use means that all analyses now use the same data quality criteria and protons on target (POT) counting on the data, as well as automatic corrections that can be applied at the final analysis level.

This analysis uses approximately 10 times as much simulated data as real data; the relevant numbers of POT are shown in Table 5.1. There were not enough simulated run 4(air) data to achieve the factor of 10, so additional run 4(water) simulated data were used to make up the difference.[2] In order to check that this substitution had a negligible effect on the analysis, the fraction of selected simulation events (that is, those passing all the requirements discussed later in Section 5.3) that originated in the P0D water/air target region was compared for two simulation setups: run 2 with water in the P0D, and run 2 with air in the P0D, as shown, with the simulated statistics, in Table 5.1. For run 2(water) the fraction of events, with binomial error, was observed to be $0.9 \pm 0.4\%$, and for run 2(air) this was $1.2 \pm 0.5\%$; numbers that are easily compatible within uncertainties.

The nominal beam simulation does not simulate the effect of beam neutrino interactions outside of the near detector. Such interactions can occur in the surrounding pit walls with the final state particle entering the instrumented area of the near detector. Therefore, in addition to the nominal magnet simulation, a dedicated 'sand muon' simulation has been produced [92], corresponding to 1.15×10^{21} POT of beam data. Whenever the beam simulation is studied, the sand muon sample is included and scaled to the correct POT.

[2] As explained in Section 3.3.3, the P0D has thick pockets that can be filled with water or air.

Unless otherwise stated, simulation statistics in all figures and tables have been normalised to the full run 2-4 good-quality[3] POT delivered to the ND280, where relevant.

5.3 $\bar{\nu}_\mu$ charged-current inclusive event selection

CC scattering of muon antineutrinos results in a positively charged muon in the final state, along with a recoiling nucleon and, perhaps, other final state particles. The lepton can be identified in the same manner as for negative muons, using the TPC particle identification (PID) algorithm. The tagging of negative muons from CC scattering of ν_μ has previously been a successful T2K analysis, so the $\bar{\nu}_\mu$ CC inclusive selection follows closely the neutrino one, with the charge selection reversed. However, the existence of different and larger backgrounds in the antineutrino sample forces the addition of further constraints on the selection.

As will be shown, the largest background in the $\bar{\nu}_\mu$ CC selection is from interactions producing a positive pion in the final state. These interactions will look very similar in the ND280 to the $\bar{\nu}_\mu$ signal. Pions at T2K's energies experience similar energy loss in the TPCs to muons, and so these subdetectors cannot be used to separate the two. The ECal modules surrounding the tracker region of the detector are, however, good for separating minimally ionising from showering particles, and so, for particles entering an ECal module, this component of the track can be used with some success in removing the pions (especially those that shower) from the muon signal. It is therefore required that the muon candidate track contain a component within one of the tracker ECal modules.

The aim of the analysis is to study interactions occurring in the FGD1 fiducial volume (FV) and the performance of the selection in separating signal from background is assessed on the basis of efficiency and purity. The efficiency, ϵ, and purity, π, of selection in the simulation are defined as follows:

[3] As defined in the following section.

$$\epsilon \equiv \frac{\text{selected true CC } \bar{\nu}_\mu \text{ interactions occurring within FGD1 FV}}{\text{all true CC } \bar{\nu}_\mu \text{ interactions occurring within FGD1 FV}},$$

$$\pi \equiv \frac{\text{selected true CC } \bar{\nu}_\mu \text{ interactions occurring within FGD1 FV}}{\text{all selected interactions}}. \tag{5.1}$$

For an event to be selected, it must pass all of the selection requirements:

- **Data quality:** The full spill must have both a good ND280 data quality and a good beam data quality flag. For the former, every subdetector within the ND280 must have been operational and taking data correctly. A good beam flag requires the beam to be at the correct intensity and in the correct direction, with stable running of the magnets.
- **Bunching:** The event is then divided into 8 bunches, and the selection proceeds with each bunch separately. The bunch width in the simulation was found to be ~ 7 ns and in the real data ~ 15 ns [93]. Any hit occurring within 4 bunch widths of the peak bunch time was associated to that bunch.
- **Track quality and fiducial criteria:** There must be at least one track with an FGD and good quality (> 18 vertical TPC clusters) TPC component, with the TPC component determining the track as having positive charge. In the case of a track that enters more than one TPC and therefore has multiple TPC components, the component closest to the start position of the track is used. The good quality requirement ensures that the TPC energy loss and curvature-based variables can be relied upon. Additionally, this track must be reconstructed as originating in the FGD1 FV, where the FV is as defined in [93]. If there is more than one such track in the bunch, the highest momentum of these as determined by the TPC component is selected as the muon candidate.
- **Backwards track rejection:** Nominally, a track's direction is assumed to be forward-going, or from within the tracker for clusters in the ECals. However, a track with components in both FGDs uses timing to discern the probable direction. In these cases, if the track's end position is further upstream than its start position, the event is rejected. This suggests that the track is originating upstream of FGD1.

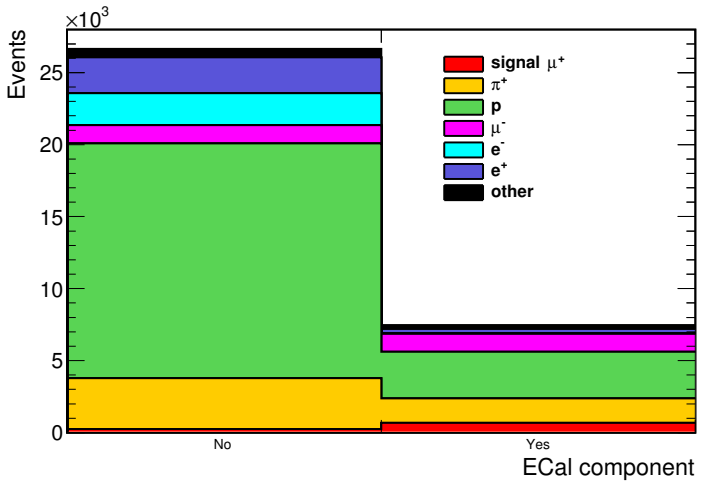

Figure 5.2: Existence of a barrel or DsECal component attached to the muon candidate before the TPC and ECal PID requirements.

- **TPC1 veto:** The start position of the track with the highest momentum, of all the tracks with TPC components in the bunch except the muon candidate, is compared with the start position of the selected muon candidate itself. If the former is more than 150 mm upstream of the latter, the event is rejected. This is an additional attempt to remove events that are originating in the P0D or the tracker ECal upstream of FGD1.

- **ECal component:** The track must have a component within one of the tracker ECal modules. A ν_μ beam interacting with a nuclear target will inevitably produce a large number of recoil protons (as well as many positive pions from resonant events). These protons are unlikely to travel far in the ND280, however, and so the majority of them should not reach the ECal surrounding the tracker region, whereas the positive muon signal, being MIP-like at these energies, will be likely to do so. Figure 5.2 shows the large background-reducing effect of this requirement on the selection. In addition to this, the ECal PID can then be used in an attempt to remove pions that the TPC PID cannot distinguish from the signal.

- **Single FGD1-TPC matched track** There must only be a single FGD1-TPC track in the current bunch, where the TPC component can in principle be within any TPC. This requirement removes the large background coming from ν_μ CC interactions, as can be seen in Figure 5.3. This is due to the fact that ν_μ CC interactions contain a proton as well as a muon in the final

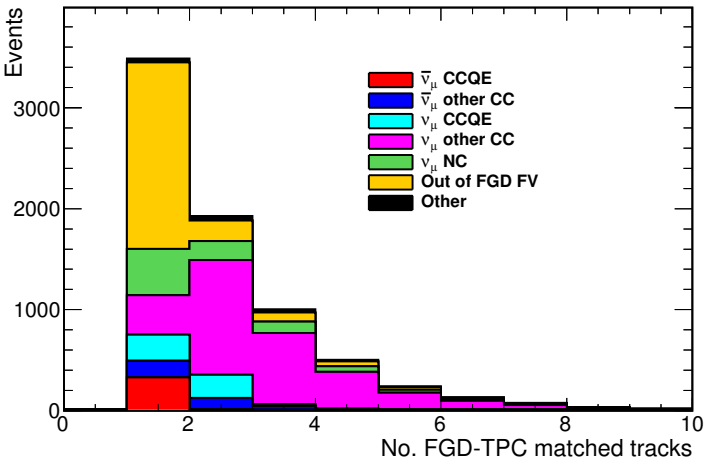

Figure 5.3: Number of matched TPC-FGD tracks in a bunch.

state, which are both visible if they traverse the TPC, whereas $\bar{\nu}_\mu$ interactions instead contain an invisible neutron.

- **TPC PID:** Likelihood functions are calculated for muon, pion and proton hypotheses based on the energy deposited by the track [93]. These are formed from pull distributions, which characterise the normalised difference in energy deposit per unit length from that expected by a particular particle, such that the distribution is Gaussian with a mean of zero and a width of one. The likelihood that a track corresponds to a particular particle, i, which can denote electron, muon, pion or proton hypotheses, is then:

$$L_i \equiv \frac{\mathrm{e}^{-Pull_i^2}}{\Sigma_l \mathrm{e}^{-Pull_l^2}} \tag{5.2}$$

where l runs over all the above possible particle hypotheses.

A feature of L_μ at this time in its development is that correctly reconstructed muon-like particles fall to the centre of the distribution. This can be seen in Figure 5.5 for the positive muons and the few forward-going negative muons that pass the previous criteria. The vast majority of the negative muons are, however, backward-going but misreconstructed as travelling in the forward direction, pushing their values to the upper end of the distribution and allowing them to be rejected using an upper cut on L_μ. Therefore the candidate track

is required to satisfy:

  - $0.1 < L_\mu < 0.7$.

  Additionally, candidate tracks of reconstructed momentum $< 500\,\text{MeV}$ are subject to the criterion:

  - $L_{\text{MIP}} \equiv \dfrac{L_\mu + L_\pi}{1 - L_p} > 0.9$.

- **ECal PID:** The ECal log-likelihood ratio cut for separating MIP-like particles from electromagnetically showering particles [94] must be passed by the selected track:

  - $\text{MIP-EM} \equiv \log\left(\dfrac{\text{Likelihood for being MIP-like}}{\text{Likelihood for being EM shower}}\right) < -10$.

Choice of TPC and ECal PID cuts

The TPC and ECal PID cut values were optimised in order to maximise the simulation prediction of the product of efficiency and purity with each cut in turn being treated as the final cut in the chain. A previous analysis [93] had already used specific cut values for the TPC PID, so these values were used initially whilst the ECal PID was optimised as the final cut. The optimisation of the ECal PID is shown in Figure 5.4; a value of -10 gives the highest figure of merit ($\epsilon \times \pi$).

The MIP-EM ECal PID cut value was then fixed at -10 to look at the optimisation of the TPC PID. Optimisation of the μ-likelihood variable gave values of 0.2 and 0.78, but the figure of merit is very flat in these areas (Figure 5.5). As the systematic uncertainties had already been studied previously at values of 0.1 and 0.7 in [93], it was decided that these values should continue to be used. This was similarly the case for the optimisation of the MIP-likelihood variable (Figure 5.6), which was done only for those events that had a global momentum of less than 500 MeV.

Performance and final sample composition

Table 5.2 shows the efficiency and purity after each successive cut. After the final cut of the selection, an efficiency of $(36.4 \pm 0.5)\%$ and a purity of $(56.1 \pm 0.6)\%$ can be achieved, based on the prediction of the simulation. The selection performance in bins of signal candidate momentum and polar angle is shown in Figure 5.7.

Cut	Efficiency (%)	Relative eff. (%)	Purity (%)	Purity (Sig./Tot.)
Track quality & fiducial	80.0±0.4	80.0±0.4	1.9±0.1	(935/49020)
Backwards track rejection	80.0±0.4	100.0±0.0	1.9±0.1	(935/48898)
TPC1 veto	78.5±0.4	98.1±0.4	2.7±0.1	(917/34129)
ECal component	58.1±0.5	74.0±0.4	9.1±0.1	(679/7480)
Single FGD-TPC track	42.1±0.5	72.5±0.4	14.0±0.2	(492/3505)
TPC PID	39.8±0.5	94.5±0.4	38.6±0.4	(465/1203)
ECal PID	36.4±0.5	91.6±0.4	56.1±0.6	(426/759)

Table 5.2: Purity and efficiency achieved after each successive cut in the $\bar{\nu}_\mu$ selection.

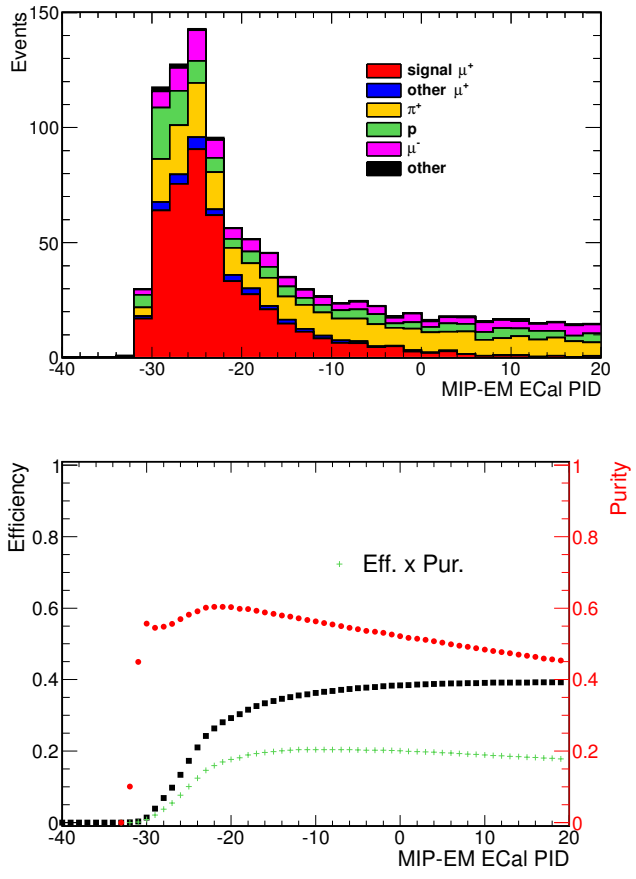

Figure 5.4: (Top) MIP-EM distribution of candidate events broken down by particle type, and (bottom) optimisation of MIP-EM variable. Black points show the efficiency, red the purity, and the figure of merit is shown in green.

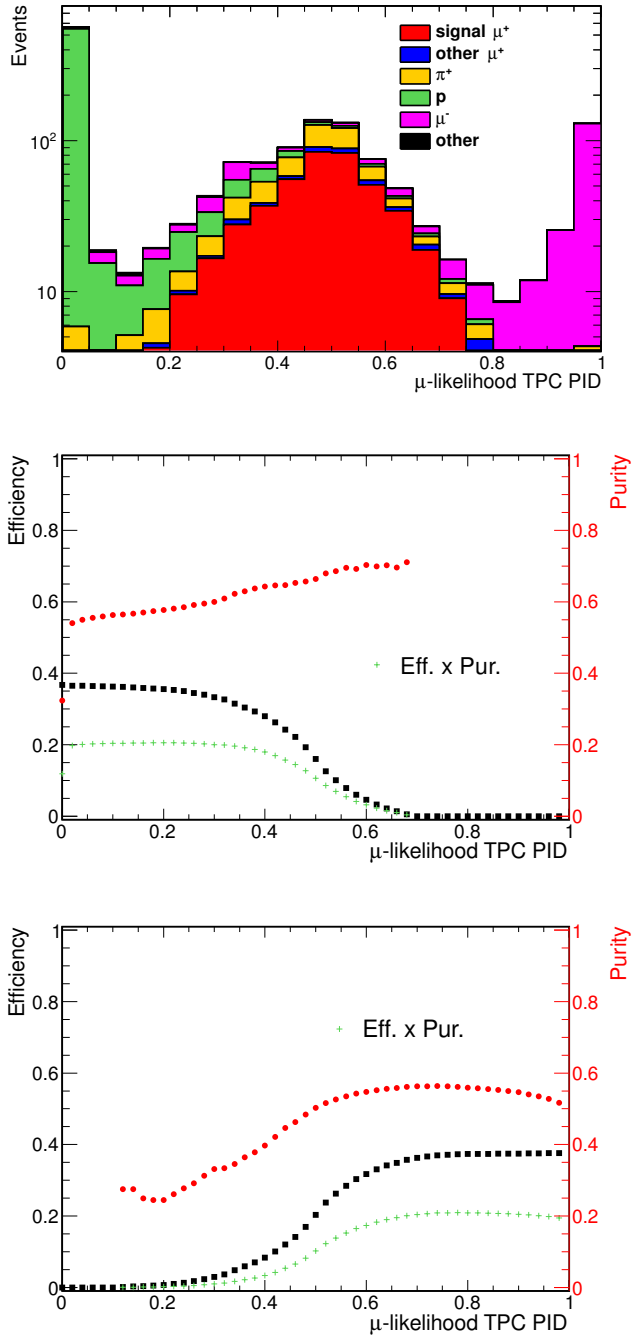

Figure 5.5: (Top) μ-likelihood distribution of candidate events broken down by particle type; (middle) optimisation of lower cut value. Black points show the efficiency, red the purity, and the figure of merit is shown in green. It can be seen that the upper cut value is in place, so that the purity becomes undefined above 0.7; (bottom) optimisation of upper cut value.

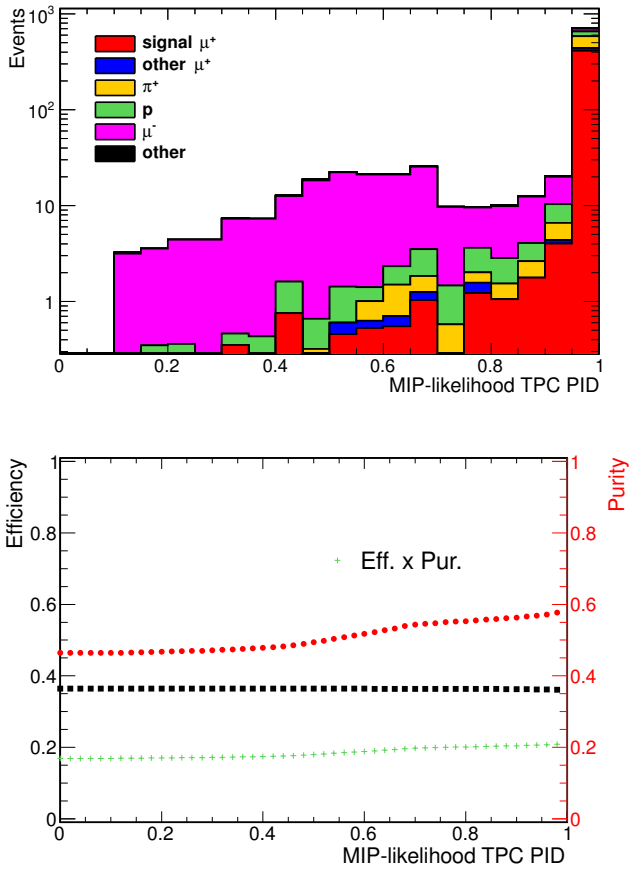

Figure 5.6: (Top) MIP-likelihood distribution of candidate events broken down by particle type, and (bottom) optimisation of MIP-likelihood variable. Black points show the efficiency, red the purity, and the figure of merit is shown in green.

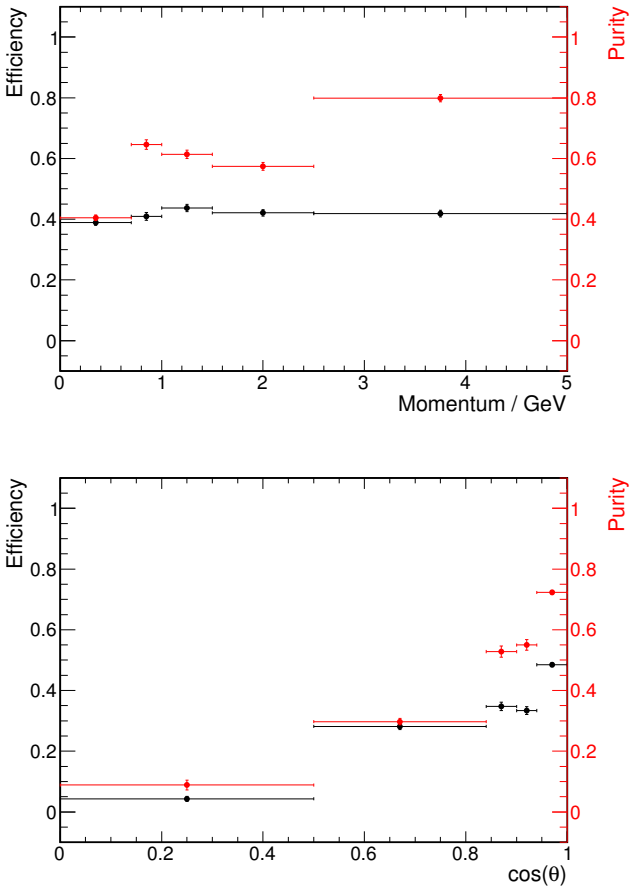

Figure 5.7: Efficiency (black) and purity (red) of selection, binned in (top) candidate muon momentum, and (bottom) candidate muon polar angle.

Figures 5.8 and 5.9 show the momentum and angular distributions of signal candidates in the simulation, broken down by particle and interaction. These compositions are also stated quantitatively in Tables 5.3 and 5.4. Of the signal, CCQE interactions comprise 68%. The background is dominated by positive pions and protons, and out-of-fiducial-volume (OOFV) events make a substantial contribution (17%). A breakdown of the OOFV background by failure mode and particle type is given later in Table 5.10. The distribution of selected events by neutrino energy is given in Figure 5.10.

Data simulation comparisons

Figure 5.11 shows comparisons of simulation with real data, normalised by POT, for the reconstructed momentum and polar angle of selected signal candidates. In general, excellent agreement is seen.

5.4 Systematic uncertainties

The systematic uncertainty on the cross-section measurement can be divided into the following categories:

- flux uncertainties;
- interaction modelling uncertainties;
- detector uncertainties;
- uncertainty on number of target nucleons;
- uncertainty due to simulation statistics.

The systematic uncertainty for each category is evaluated by modifying the simulation a large number of times and observing the effect on the extracted cross-section. After consideration of the biases and errors involved in extracting a cross-section, a study of which is reported in Appendix A.1, it was decided that the cross-section should be extracted in this analysis by correcting for the purity of the simulation sample (as opposed to the more often used background subtraction method), as shown in Equation (5.3) below:

Particle	Fraction
Signal μ^+	56%
Other μ^+	4%
π^+	20%
p	11%
μ^-	9%
π^-	$< 1\%$
Other	$< 1\%$

Table 5.3: Composition of final simulated data sample by particle type.

Interaction	Fraction
$\bar{\nu}_\mu$ CCQE	38%
$\bar{\nu}_\mu$ other CC	18%
$\bar{\nu}_\mu$ NC	$< 1\%$
ν_μ CCQE	4%
ν_μ other CC	13%
ν_μ NC	10%
Out of FGD FV	17%
Other	$< 1\%$

Table 5.4: Composition of final simulated data sample by interaction.

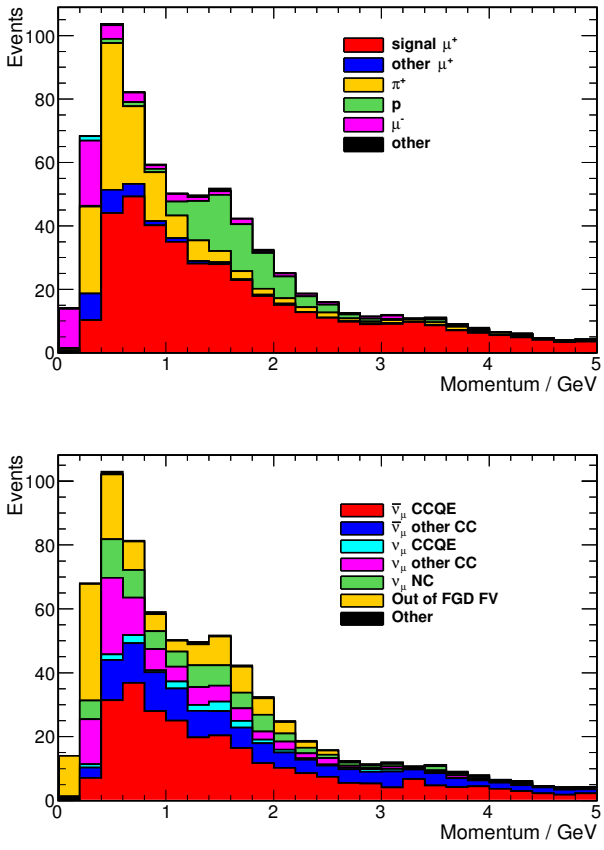

Figure 5.8: Reconstructed momentum distribution of selected signal candidates, broken down by (top) particle type, and (bottom) neutrino interaction.

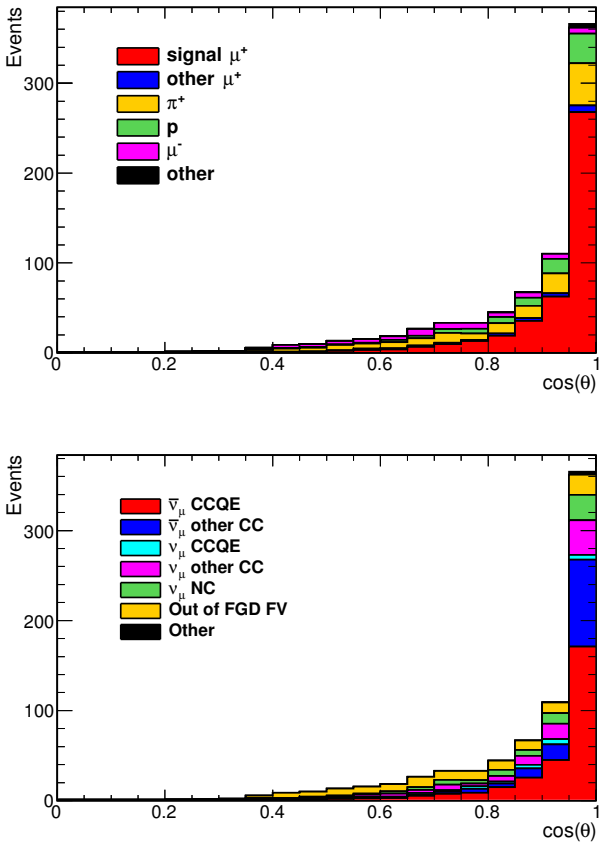

Figure 5.9: Reconstructed polar angle distribution of selected signal candidates, broken down by (top) particle type, and (bottom) neutrino interaction.

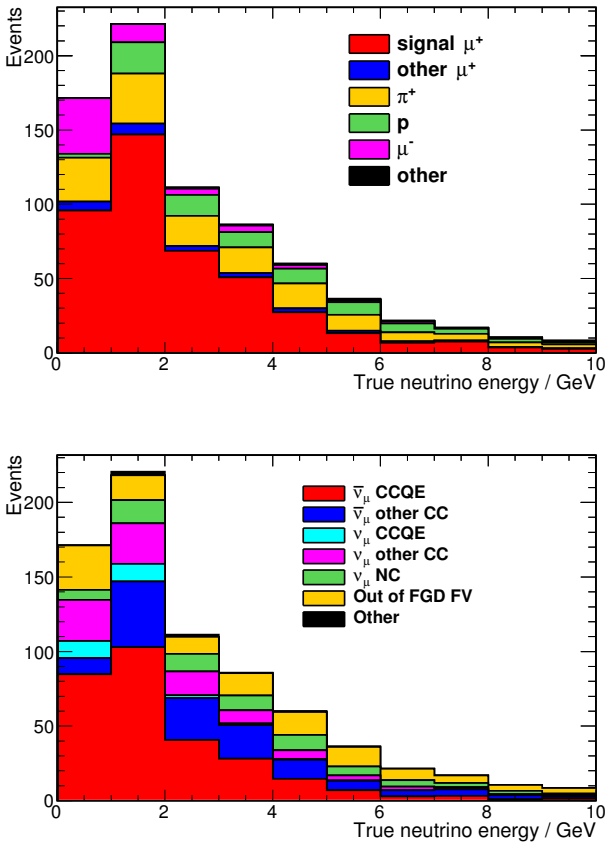

Figure 5.10: True energy of neutrino parent of selected signal candidates, broken down by (top) particle type, and (bottom) neutrino interaction.

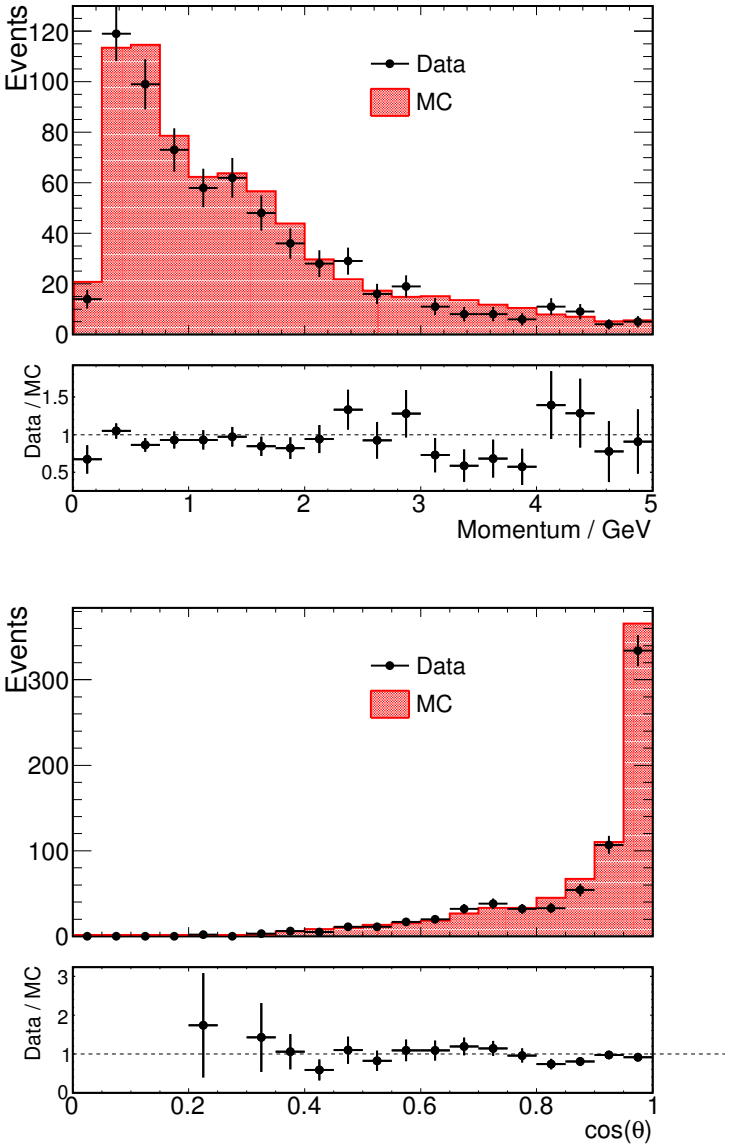

Figure 5.11: Data simulation comparison of (top) reconstructed momentum, and (bottom) polar angle of final selection samples.

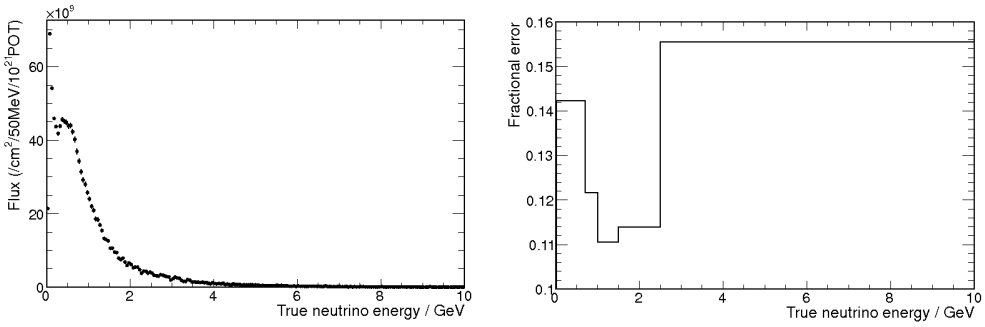

Figure 5.12: (Left) Tuned $\bar{\nu}_\mu$ flux spectrum prediction for the T2K run2 data-taking period, and (right) $\bar{\nu}_\mu$ flux fractional error prediction.

$$\sigma_{\text{sim}} = \frac{N_{\text{sim}}^{\text{obs}}\pi}{T\Phi\epsilon}. \tag{5.3}$$

For systematic studies, no real data are looked at, so $N_{\text{sim}}^{\text{obs}}$ is the total number of selected events in the nominal simulation. ϵ and π are the simulation efficiency and purity respectively, T is the number of target nucleons within the FGD1 FV and Φ is the average flux density predicted across its face.

Each modification, or 'throw', of the simulation reweights all selected events and all true $\bar{\nu}_\mu$ CC events,[4] affecting the purity and the efficiency of selection.

5.4.1 Flux uncertainties

The flux systematic uncertainty is evaluated by varying the shape and normalisation of the T2K flux prediction. This is done by varying different flux bin weights, where a separate bin is defined for each detector (near and far), neutrino flavour, and energy range. For the near detector, 25 bins are provided, with bin boundaries defined as:

- ν_μ: 0.0, 0.4, 0.5, 0.6, 0.7, 1.0, 1.5, 2.5, 3.5, 5.0, 7.0, 30.0 GeV;
- $\bar{\nu}_\mu$: 0.0, 0.7, 1.0, 1.5, 2.5, 30.0 GeV;
- ν_e: 0.0, 0.5, 0.7, 0.8, 1.5, 2.5, 4.0, 30.0 GeV;

[4]Some detector systematics do not conform to this reweighting style, and will be explained in detail in their appropriate subsection.

Source	ν_μ flux uncert. (%)	$\bar{\nu}_\mu$ flux uncert. (%)
Kaon production	1.0	1.8
Pion production	5.4	5.2
Proton beam	1.8	0.7
Off-axis angle	2.3	1.3
Horn angular alignment	0.5	1.0
Horn field asymmetry	0.4	0.9
Production cross-section	6.9	4.2
Horn absolute current	1.1	0.8
Target alignment	0.4	2.2
Secondary nucleon production	6.9	10.3

Table 5.5: Sources of uncertainty contributing to the total flux uncertainty, as studied in [95], [78].

- $\bar{\nu}_e$: 0.0, 2.5, 30.0 GeV.

These bins are correlated and this information is encoded within the flux covariance matrix provided by the T2K Beam group [95]. The matrix incorporates the different sources of the flux uncertainty, which are summarised, for ν_μ and $\bar{\nu}_\mu$, in Table 5.5. The square root of the diagonal components of this matrix give the fractional error in each bin; the projection of this for the $\bar{\nu}_\mu$ flux is shown in Figure 5.12.

A 25-dimensional Gaussian is generated with correlations set by the covariance matrix. For each of the 10000 throws, a dataset is generated according to this Gaussian, and these points are used to reweight every selected event and every true $\bar{\nu}_\mu$ CC event. The flux weights themselves are also saved and used, in order to calculate the total simulated $\bar{\nu}_\mu$ flux of that throw. The flux, the efficiency and purity of the modified simulation are then used to extract the fractional change in the cross-section measurement:

$$\frac{\Delta\sigma}{\sigma} \equiv \frac{\sigma_{\text{sim,nom}} - \sigma_{\text{sim,i}}}{\sigma_{\text{sim,nom}}} \tag{5.4}$$

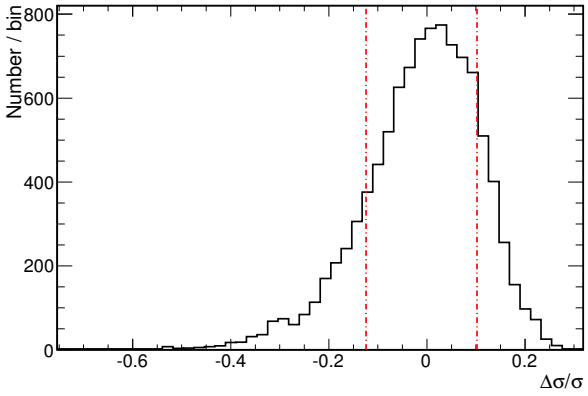

Figure 5.13: Distribution of fractional change in cross-section after modification of flux. The final uncertainty is found to be +10.2%, −12.4%.

where $\sigma_{\text{sim,nom}}$ is the nominal cross-section using $N_{\text{sim}}^{\text{obs}}$ as the number of selected events, and $\sigma_{\text{sim,i}}$ is the cross-section calculated using the same value of $N_{\text{sim}}^{\text{obs}}$ from the nominal simulation, but with the modified values of efficiency, purity and flux.

The distribution of the fractional difference in cross-section is shown in Figure 5.13. The distribution is skewed due to the simultaneous variation of the three Gaussian-distributed variables and so the uncertainty is taken to be the central area in the case that each tail contains 16% of the throws; the final uncertainty is found to be +10.2%, −12.4%.

5.4.2 Interaction modelling uncertainties

The NEUT neutrino interaction generator contains parameters that affect each interaction process. These parameter values generally come from past experimental data. As discussed previously, neutrino cross-section data, especially at T2K energies, are quite sparse, so their uncertainties cannot be ignored and their effects on the final cross-section measurement need to be quantified.

The neutrino interaction generator is the first step in generating simulated data to compare to the real data. It is not feasible to actually modify these parameters and generate simulated data each time; instead, a reweighting tool has been implemented by T2K collaborators, which has been verified to give the same effect on the output distributions as varying the underlying parameters themselves [96].

Using the T2K simulation reweighting tool, each true $\bar{\nu}_\mu$ CC event and each selected

event is reweighted to emulate the effect of a variation of the underlying cross-section parameters according to the recommendations in [97] [96], which themselves were chosen based on external data. These are reproduced in Table 5.6.

The $M_{\mathrm{A}}^{\mathrm{RES}}$, NC1$\pi^0$ normalisation and CC1π $\mathrm{E}_\nu < 2.5\,\mathrm{GeV}$ normalisation parameters are correlated. Therefore, for the systematic uncertainty evaluation the covariance matrix encoding these correlations is used to vary all parameters simultaneously. A multi-dimensional Gaussian is generated for each of the 2000 throws, and these numbers are used to reweight every event in the selection, and every true signal event. In the same way as for the flux systematic uncertainty calculation, the effect of each throw on the cross-section calculation is evaluated. Again $N_{\mathrm{sim}}^{\mathrm{obs}}$ is fixed, and the efficiency and purity of the selection is recalculated using the reweighted events. The width of the distribution is taken to be the systematic uncertainty, which, from Figure 5.14, can be seen to be 5.1%.

As only a few of the parameters are correlated, a cross-check of the method is made by varying the parameters in turn by $\pm 1\sigma$, with all other parameters remaining at their nominal values. This allows the effect of a modification of each parameter on the final cross-section to be understood. The percentage error from positive and negative parameter variations are shown in Figure 5.15. For each of the 19 parameters considered, the largest fractional error of the positive and negative variations is taken and these are summed in quadrature to give a value of 5.2% for the total error, in agreement with the previous method's results. It can be seen in Figure 5.15 that the largest contributor to the total cross-section systematic uncertainty comes from CC coherent pion production events. This is because, although these interactions only make up approximately 7% of the sample, a 100% error is applied to them. This error is applied due to results from two external experiments consistent with no coherent pion production at $\mathcal{O}\,(1\,\mathrm{GeV})$ [98].

5.4.3 Detector uncertainties

Detector systematic uncertainties arise due to imperfections in the simulation of the detector response, and are effectively manifest in the efficiency with which background events are removed whilst signal events are retained.

As explained in Section 5.3, the $\bar{\nu}_\mu$ CC selection has much in common with a previously completed analysis: the tracker ν_μ CC selection. Under the assumption that positive muons exhibit the same systematic differences in data and simulation to negative muons, many of the systematic uncertainties assigned to the selection

Parameter	Code	Nominal value	Fractional error
CCQE $E_\nu < 1.5$GeV norm.	ccqeE0	1.0	0.11
CCQE $1.5 < E_\nu < 3.5$GeV norm.	ccqeE1	1.0	0.3
CCQE $E_\nu > 3.5$GeV norm.	ccqeE2	1.0	0.3
CC1π $E_\nu < 2.5$GeV norm.	cc1piE0	1.0	0.32
CC1π $E_\nu > 2.5$GeV norm.	cc1piE1	1.0	0.4
CCCoh norm.	cccoh	1.0	1.0
CC other shape	dismpishp	0.0	0.4
CC ν_e norm.	ccnue	1.0	0.06
NC1$\pi^\pm$ norm.	nc1piE0	1.0	0.3
NC1π^0 norm.	nc1pi0E0	1.0	0.33
NCCoh norm.	nccoh	1.0	0.3
NC Other norm.	ncother	1.0	0.3
W shape	δmasswidth	87.7 MeV	0.52
Spectral function	sf	0 (Off)	1 (On)
P_f	pf	217 MeV/c	0.14
Binding energy	eb	217 MeV/c	0.36
1π E_ν shape	mbcc1pi	0.0	0.5 (Absolute)
M_A^{QE}	MaCCQE	1.21 GeV	0.37
M_A^{RES}	MaRES	1.21 GeV	0.18

Table 5.6: Varied interaction parameters. The code is a shortened name for the parameter, used in Figure 5.15.

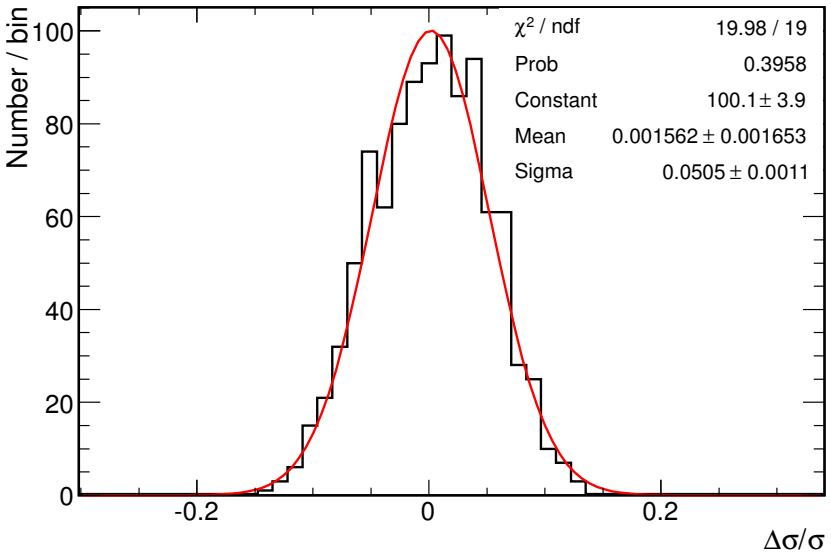

Figure 5.14: Distribution of fractional change in cross-section after modification of interaction parameters together.

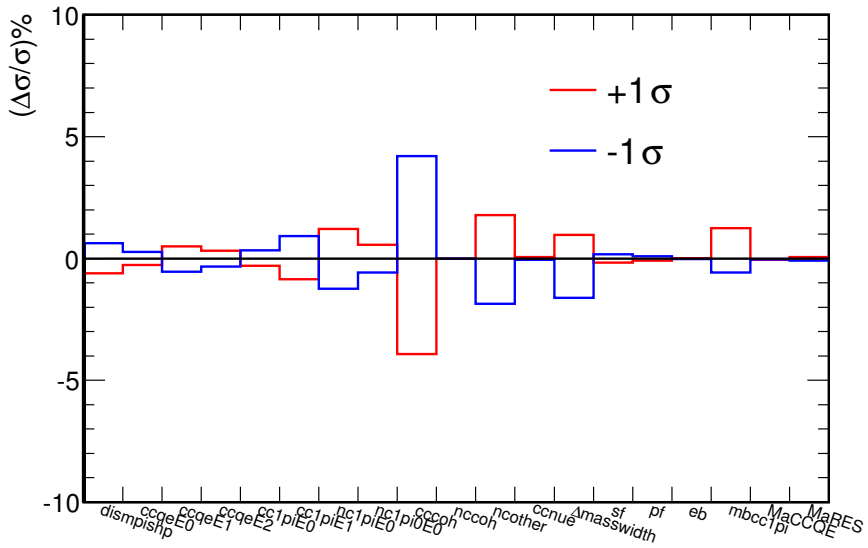

Figure 5.15: Fractional change on the calculated cross-section after variation of single interaction parameters. The interaction parameter name for each code is given in Table 5.6.

criteria for that analysis can also be used in this case. On top of these, the present analysis uses the ECal, so a study of the systematics associated with this will also be shown below.

Detector uncertainties from tracker ν_μ CC analysis

TPC cluster efficiency

The difference in the cluster efficiency between data and simulation was found to be very small [99]. As in the T2K tracker ν_μ analysis, it is assumed that this is the only source of systematic error associated with the track quality cut, and therefore this difference is not considered any further.

TPC track-finding efficiency

The track-finding efficiency in a single TPC is evaluated by verifying that a track was reconstructed in that TPC if the detectors immediately upstream and downstream both reconstructed a track, using a control sample of muons that traversed the entire ND280 [99]. No momentum dependence is visible and the data and simulation are both compatible with achieving a 100% efficiency within statistical uncertainties, so no systematic uncertainty is assumed.

FGD-TPC matching

The FGD-TPC matching systematic is evaluated similarly to the TPC track finding efficiency; the same muon control sample is used and in this case an FGD1-TPC2 reconstructed track is expected if there were reconstructed components in both TPC1 and TPC2. Any lack of this reconstructed multi-subdetector track for these events is regarded as a matching inefficiency.

The efficiency difference between data and simulation increases at very low momenta [99], so the systematic is given in three momentum bins, as shown in Table 5.7.

As explained in Section 5.3, the track selected as the muon candidate in each bunch is the highest momentum positively charged track. It is in principle possible that, if the highest momentum track had been discarded, the second-highest momentum track would have passed all the cuts instead, contributing to either the signal or

Mom. (GeV)	0–0.1	0.1–0.2	> 0.2
Data−sim. (%)	15	0.4	0.2

Table 5.7: FGD-TPC matching absolute efficiency percentage difference between data and simulation.

background in the selection. For this reason, a study was conducted in which it was noted whether the second highest momentum track of the bunch would have passed the selection, for all events in which the highest momentum track had itself passed. As only 4.7 events out of the 7593 selected had such a second highest momentum track, it was concluded that this potential complication could be safely ignored.

To propagate the FGD-TPC matching systematic, random selected events were discarded in the simulation to mimic an FGD-TPC matching failure. Each event's probability of being discarded was equal to the data simulation difference in the true candidate muon's momentum bin. As this is an efficiency-based systematic, the mean of the fractional change distribution is taken as the systematic uncertainty; this gives 2.1%.

TPC PID

A high purity muon sample is used to obtain the systematic uncertainty associated to the TPC PID. The underlying pull distributions used in the formation of the likelihood functions are compared between simulation and data. The systematic uncertainty is taken as the smearing required to correct the width of the simulation to that of real data. These smearing factors are calculated separately for TPC2 and TPC3, but both give values of 1.03 [93].

To propagate the systematic uncertainty, the likelihood functions are recalculated for every nominally selected simulation event using a smeared value of the underlying pull value. The likelihood functions are then re-evaluated to see if the event still passes the criteria, and the cross-section is recalculated. The quadratic sum of the offset and the width of the fractional change distribution shown in Figure 5.16 is taken as the systematic uncertainty, which gives 0.3%.

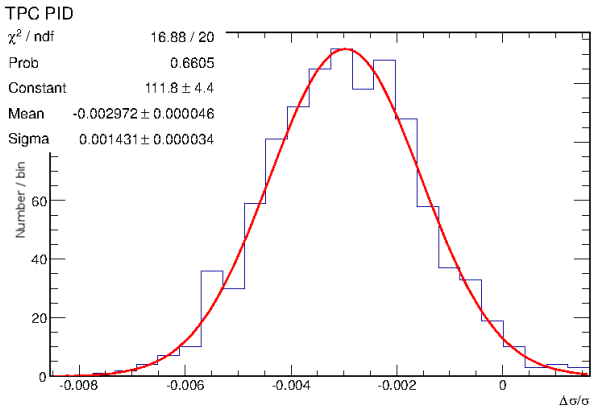

Figure 5.16: Distribution of fractional change in cross-section after propagation of TPC PID systematic uncertainty. The quadratic sum of the offset and the width of the distribution is taken as the systematic uncertainty.

TPC momentum resolution

The TPC momentum resolution systematic was studied by obtaining a control sample of muon-like tracks crossing (at least) two TPCs in beam-spill data and simulation. The momentum resolution is taken as the inverse momentum transverse to the magnetic field calculated in one TPC segment compared to that of the other (and corrected for energy loss in the intervening FGD). This distribution is approximately Gaussian with widths for both data and simulation between 10–20%. The difference in width between data and simulation is used to characterise the systematic uncertainty, which was found to be approximately 32% across all momenta [99].

Although this is a large difference, the present analysis uses momentum only in the MIP-likelihood TPC PID cut, and so its effect is expected to be minimal. Propagating the systematic uncertainty and taking the width of the fractional error distribution gives a value of 0.6%.

TPC charge misidentification

Similarly to the TPC momentum resolution systematic, this systematic relies on the information provided in data and simulation from multiple TPCs. The charge misidentification systematic is found by observing the number of events in which the charge evaluation from two TPCs gives the same sign and the number that give a different sign; the probability of giving the wrong charge sign is then calculated alge-

Mom. (GeV)	0–0.1	0.1–0.3	0.3–0.6	0.6–1.0
Data (%)	2.63±1.84	2.47±0.74	0.98±0.09	0.88±0.05
Sim. (%)	1.5±1.5	2.5±1.0	0.67±0.07	0.70±0.05
Data−sim. (%)	1.13±2.37	0.03±1.24	0.31±0.11	0.18±0.07
Mom. (GeV)	1.0–1.5	1.5–3.0	3.0–5.0	5.0–20.0
Data (%)	1.02±0.04	1.85±0.03	4.29±0.07	11.0±1.6
Sim. (%)	1.20±0.06	1.89±0.06	3.52±0.10	7.95±0.20
Data−sim. (%)	0.18±0.07	0.04±0.07	0.78±0.12	3.05±1.61

Table 5.8: Charge misidentification absolute percentage difference between data and simulation. Table modified from [99].

braically from these numbers [100]. As tracks become straighter at higher momenta, the charge misidentification probability will increase, and so the systematic is given in bins of momentum [99]. The difference in the percentage of charge misidentified tracks between data and simulation is taken as the systematic to propagate; these numbers are shown in Table 5.8.

Propagation of the systematic gives the uncertainty assigned to the TPC charge confusion to be 0.6%.

Out-of-fiducial-volume background

OOFV background comprises 17% of the selected events in the simulation. This background is categorised into several failure modes as shown in Table 5.9 and discussed in more detail below. For each failure mode, an associated uncertainty is assigned according to:

- how precisely the interaction rate is known;
- how differently the reconstruction algorithms perform between real and simulated data.

The first of these is only significant for events that originate outside the whole tracker region, as uncertainties in the rate of events originating within the tracker but outside the FGD FV (i.e. the first three categories in Table 5.9) are already taken into account in the interaction modelling uncertainty described in Section 5.4.2. For the remaining categories, a rate uncertainty of 20% was assigned based on studies in

the P0D, ECal and SMRD subdetectors comparing the NEUT and GENIE generator predictions [101].

The various failure categories are explained below and given in Table 5.9, which also shows the fraction of the total OOFV events contained in that category, the rate uncertainty associated to it, and the uncertainty from data-simulation differences in the reconstruction performance. Additionally, the momentum distribution of these events broken down by category is shown in Figure 5.17 and the particle make-up of each category is shown in Table 5.10.

- **Interactions in upstream tracker material *and* interactions in FGD but OOFV:** Events originating in the dead material upstream of the FGD FV, or those that fail to produce hits in the most upstream layers due to bar clipping or hit inefficiency, can be reconstructed as starting in the FV. These events are given the same 5% reconstruction systematic as those originating in the downstream tracker material.

- **Interactions in downstream tracker material:** Hadrons can travel backwards into the FGD from an interaction vertex in the dead area between the subdetectors, while other particles from the event can traverse the TPC, causing a single track to be reconstructed with a vertex in the FGD FV. A 5% reconstruction systematic has been measured in studies of this background [101].

- **Neutral particles:** A neutral particle produced in a neutrino interaction outside of the FGD may interact to produce charged tracks within it. This will look like a neutrino interaction inside the FGD and it is not possible for these to be identified as OOFV events. Many of the protons that pass the selection with a momentum around 1–2 GeV (see Figure 5.8) are knock-on protons from neutral particles. As it is never possible for these to be identified as OOFV events, there is no data-simulation reconstruction difference associated to this background, but a 20% rate uncertainty is included [101].

- **Backward-going tracks:** The $\bar{\nu}_\mu$ selected sample contains a substantial background at low momenta from negative muons (see Figure 5.8). Approximately half of these are backward-going from the ECal and magnet, which have been reconstructed as forward-going positively charged particles beginning in the FGD FV. The reconstruction software has no capability to distinguish backward- from forward-going tracks, so there is no reconstruction systematic related to these events; there is however a 20% rate uncertainty [101].

- **High-angle tracks:** The T2K software version used in the analysis can often

Background type	Fraction of OOFV (%)	Rate uncert. (%)	Recon. syst. (%)	Total error (%)
In FGD but OOFV	6.4	0	5	5
Int. upstream	2.9	0	5	5
Int. downstream	3.9	0	5	5
Neutral (grand)parent	26.7	20	0	20
Backward-going	13.2	20	0	20
High-angle	16.7	20	$^{+150}_{-100}$	$^{+151}_{-100}$
Double skipped layers	4.7	20	40	45
Layer 28 or 29	7.3	20	25	32
Other	18.2	20	$^{+150}_{-100}$	$^{+151}_{-100}$

Table 5.9: The various categories of reconstruction failure resulting in the selection of out-of-fiducial-volume events and their respective contribution and errors.

Failure mode / Particle (%)	μ^-	μ^+	π^-	π^+	$p+$	other
In FGD but OOFV	0.6	2.9	-	2.1	0.8	-
Int. upstream	0.3	0.5	-	1.6	0.6	-
Int. downstream	0.6	1.5	-	1.1	0.5	-
Neutral (grand)parent	-	1.1	0.1	4.7	20.8	-
Backward-going	11.9	-	0.9	0.5	-	-
High-angle	11.9	1.0	0.3	3.4	0.1	-
Double skipped layers	0.4	0.6	-	2.9	0.8	-
Layer 28 or 29	2.7	2.5	0.2	1.9	-	-
Other	1.9	1.9	0.1	10.6	3.6	0.2
Total	**30.3**	**12.0**	**1.6**	**28.8**	**27.2**	**0.2**

Table 5.10: The particle make-up of each out-of-fiducial-volume failure mode. Each element is the percentage of the total OOFV background.

fail in the matching of TPC hits to FGD hits for tracks that enter the FGD at angles approaching 90° to the beam axis. If some FGD hits are not included, a gap in the hits is seen by the track-finding software, and therefore a track starting in the FGD FV is constructed. A large systematic difference in this failure mode is seen in comparing data and simulation; a $^{+150}_{-100}$% reconstruction systematic is assigned [99]. The other half of the low-momentum wrong-sign muons fall into this category.

- **Double skipped layers:** A track from a single particle entering the FGD FV will be broken into two separate tracks if two consecutive layers in the FGD contain no hits. This causes the reconstruction software to assume a particle interaction within the FGD FV. As well as the 20% rate uncertainty, a 40% reconstruction systematic is assigned to this category.

- **Layer 28/29 failures:** A failure in the TPC x-coordinate reconstruction due to a problem in the drift velocity or time offset results in a match to the FGD hits in the YZ projection only. This causes the software to reconstruct the track as beginning in layer 28/29 whether it began OOFV or not. A 25% reconstruction systematic is added in quadrature to the 20% rate uncertainty assigned to this class of event.

- **Other:** This category contains all events that do not fall into any other, but do have a true vertex originating OOFV. These include particles that undergo hard elastic scatters and also various matching failures that are not included in the above. Conservatively, the same error as the largest from the other categories is assigned here.

These errors are propagated by reweighting the OOFV events in the simulation according to the total error associated to them. The total error for each category is taken to be the quadratic sum of the rate and reconstruction uncertainties, as shown in Table 5.9. The width of the cross-section fractional change distribution gives a systematic uncertainty of 4%, as shown in Figure 5.18.

OOFV backgrounds make up 17% of the analysis sample (Table 5.4) and this version of the analysis constrains these backgrounds only through simulation studies. It is expected that any future iteration of the analysis will constrain at least the two largest components of this background (Table 5.10), high-angle or backward-going muons, and knock-on protons from neutrons entering the FGD, using data-driven methods.

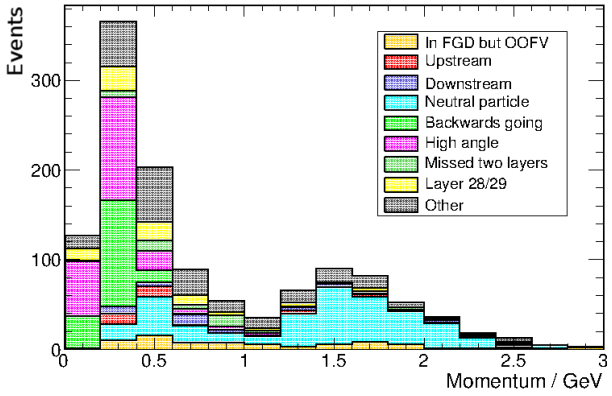

Figure 5.17: Momentum distribution of selected out-of-fiducial-volume events broken down by category.

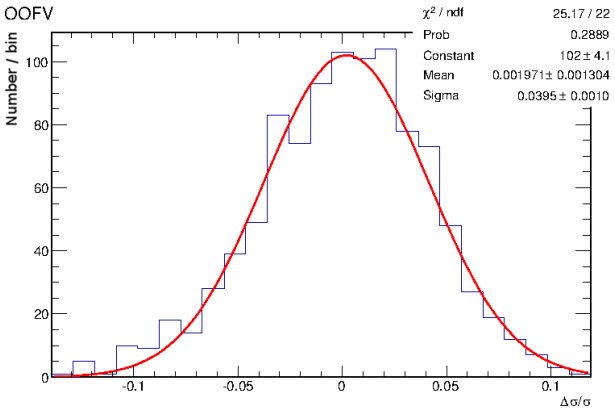

Figure 5.18: Distribution of fractional change in cross-section after propagation of out-of-fiducial-volume systematic. The width of the distribution is taken as the systematic uncertainty.

Other systematic uncertainties

TPC-ECal reconstruction and matching efficiency

This systematic accounts for any differences between real data and simulation in both the reconstruction of an ECal object and the matching of that object to the FGD-TPC track. The efficiency is defined as:

$$\frac{\text{Number of tracks entering the ECal with an ECal object attached}}{\text{Total number of tracks entering the ECal}}.$$

The systematic evaluation is split between that for the DsECal and that for the barrel ECal modules. Samples of muons starting in FGD1 and originating from beam-spill neutrino interactions were selected using the following selection criteria, based on the information from the track's most downstream TPC component, and applied to the highest momentum track in the bunch:

- at least 19 nodes;
- muon-like from TPC PID:
  - $-2 <$ muon pull < 2,
  - $\neg\ (-1 <$ electron pull $< 2.5)$.

In addition, the tracks had to be located within the acceptance of an ECal module. This requirement was achieved by putting criteria on the TPC exit position and angle. For tracks entering the DsECal these were:

- TPC exit position,
  - $-920 < x < 920\,\text{mm}$, $-910 < y < 930\,\text{mm}$, $z > 2665\,\text{mm}$;
- TPC exit angle,
  - $\theta < 40^\circ$ from the z-axis.

For the barrel selection, these criteria were:

- TPC exit position,
  - $-920 < x < 920\,\text{mm}$, $-910 < y < 930\,\text{mm}$, $z > 2665\,\text{mm}$;
- TPC exit angle,
  - $\theta < 40^\circ$ from the z-axis;

– $-160° < \phi < 160°$.

The azimuthal angle requirement was placed in order to remove those tracks that were escaping through the gap in the ECal modules where the magnet could be opened.

The data and simulation efficiencies were evaluated in bins of momentum from 0.3 GeV up to 5 GeV.[5] The difference in efficiency averaged across the whole momentum range, added in quadrature with the statistical uncertainty on the difference, is taken as the total systematic. This gives a value of 0.6% for the DsECal and 2.9% for the barrel modules [102].

The systematic uncertainty propagation was conducted by randomly rejecting 0.6% of all events with DsECal components and 2.9% of those with barrel ECal components. The mean of the fractional change in cross-section distribution was then taken as the systematic uncertainty, which was 1.2%.

ECal PID

A study of true muons in the ECals has revealed a data-simulation difference of 1% for a MIP-EM cut value of 0.0 [103]; this difference approaches zero at the cut value used in the current analysis. However, it should not be assumed that the control sample used for the systematic evaluation can exactly be transferred to the sample in the analysis. For this reason, a difference of 1% is used as the systematic to propagate.

Propagating the systematic and taking the fitted mean of the fractional change in cross-section distribution gives the systematic uncertainty associated to the ECal PID to be 1.6%.

Sand muon background

Particles from beam neutrino interactions in the area surrounding the ND280 are a source of background in the data sample that is not accounted for in the standard simulation. However, a dedicated sand muon sample, corresponding to 11.5×10^{20} POT of beam data, was generated during the production [92].

[5] Below 0.3 GeV the tracks are very heavily curved in the magnetic field. Many passing the requirement to be considered as entering an ECal module curve so aggressively that they do not in fact enter. Above 5 GeV the statistics are too low to consider.

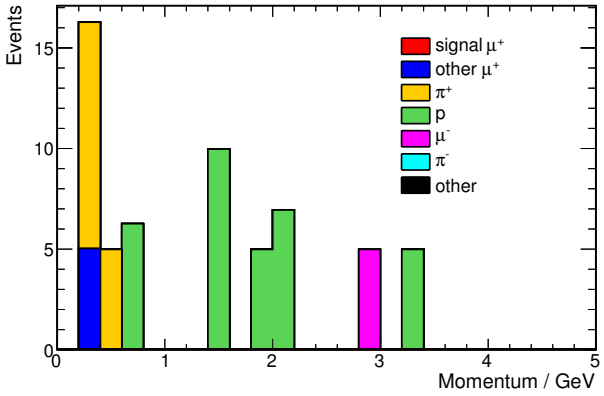

Figure 5.19: Momentum distribution of selected events in 11.5×10^{20} POT equivalent of sand muon simulation.

To compare the rate of sand muons that enter the near detector, a selection was made that required tracks to be entering from the upstream face of the P0D [99]. The sum of the contribution from sand and standard magnet simulation was compared to the rate in data, and the difference was measured to be approximately 10%.

The sand muon sample was processed through the $\bar{\nu}_\mu$ selection, and, after scaling by the total POT in the standard simulation (57.33×10^{20}), 59.4 events were selected, as shown in Figure 5.19. This is equivalent to 0.8% of the total number of selected events in that run period.

Taking the product of the difference in the rate of sand muon interactions between data and simulation, and the fraction of the selection that come from neutrino interactions outside of the ND280, the propagated systematic uncertainty from sand muon interaction rates is taken as 0.08%.

Pion secondary interactions

A charged pion exiting a target nucleus can undergo a secondary interaction with another nucleus in its path such that its charge is modified, or such that it does not continue beyond the secondary interaction at all. Although these are modelled in the simulation package of particles through matter, GEANT, it is known that there is both a large uncertainty on these cross-sections, and, for total absorption, a significant discrepancy between the model and data, as can be seen in Figure 5.20.

A simulation study was conducted that looked at the effect of the two most signif-

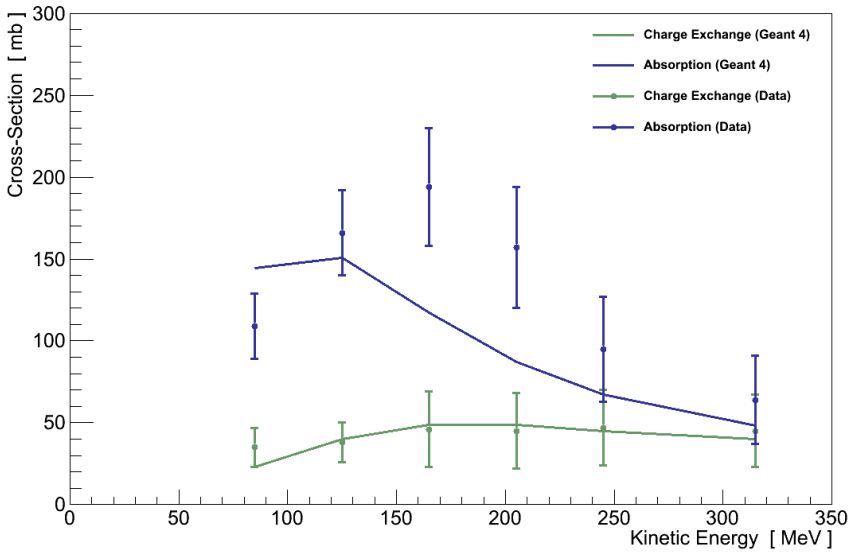

Figure 5.20: Data and simulation charge exchange and absorption cross-section comparisons for charged pions on carbon. Figure from [77].

icant pion interactions that could result in no signal in the TPC [77]. Using truth information, a sample of (single) pions created in FGD1 and heading towards TPC2 was selected. Each event was then classified according to its fate, as done in the original study [104], with the following categories:

- **Charge exchange:** The charged pion interacts with the nucleus, producing a neutral pion, which will almost immediately decay to photons and electromagnetically shower.
- **Absorption:** The pion gets absorbed totally during the secondary interaction, and no pion will enter the TPC.
- **Entered TPC2:** The pion successfully traverses the remainder of FGD1, and is recorded as entering TPC2 by the simulation.
- **Other:** Primarily, pions that interact in some way other than the above two, and are deflected so as not to go through TPC2. This includes elastic scatters.

Pion interaction cross-section data currently has a large uncertainty, as can be seen from the error bars in Figure 5.20. Event weights were calculated to simulate the effect of a cross-section that matched the top of these error bars. Further weights were then calculated in the same way to match up with the bottom of the bars.

To propagate the systematic, all true pion events in the analysis sample were given the weight corresponding to their initial kinetic energy-distance bin,[6] and the cross-section was reevaluated. The fractional difference in this cross-section from the nominal cross-section was then taken as the systematic uncertainty. This was observed to be 0.8% for the weights corresponding to a cross-section equal to the upper data error band, and 0.4% for the lower error band. The larger difference of 0.8% is taken as the systematic uncertainty.

The detector systematic uncertainties are summarised in Table 5.11. The contributions are summed in quadrature to give a total detector systematic uncertainty of 5.1%.

5.4.4 Number of target nucleons

The uncertainty on the number of target nucleons within the FGD1 FV has been calculated previously in the ν_μ inclusive CC cross-section analysis [97] [105]. The uncertainty was calculated to be:

$$\frac{\delta T}{T} = 0.67\%. \tag{5.5}$$

5.4.5 Simulation statistics

The efficiency and purity of the selection predicted by simulation could have been slightly different due to the finite statistics produced; this can cause a further systematic error on the final measurement. The systematic uncertainty due to simulation statistics is found by throwing 10000 alternative experiments where the simulation signal and background are varied according to the Poisson distribution. All other factors in the cross-section remain fixed, and the effect on the calculated cross-section is considered. The width of the cross-section fractional change distribution is taken as the systematic uncertainty. This is shown in Figure 5.21 to be 1%.

The systematic uncertainties are summarised in Table 5.12. The contributions are summed in quadrature to give a total systematic uncertainty of $+12.6\%,-14.4\%$.

[6] The interaction probability of the pion is dependent upon both its initial kinetic energy, and the distance it must travel through FGD1 before successfully reaching TPC2.

Source of uncertainty	Systematic uncertainty
FGD-TPC matching	2.1%
TPC PID	0.3%
TPC momentum resolution	0.6%
TPC charge confusion	0.6%
TPC-ECal matching	1.2%
ECal PID	1.6%
OOFV	4.0%
Sand muons	0.08%
Pion secondary interactions	0.8%
Total:	**5.1%**

Table 5.11: Summary of systematic uncertainties from detector effects.

Source of uncertainty	Systematic uncertainty
Flux	+10.2%,−12.4%
Interactions	5.1%
Detector	5.1%
Target nucleons	0.67%
Simulation statistics	1.0%
Total:	+12.6%,−14.4%

Table 5.12: Overall summary of systematic uncertainties.

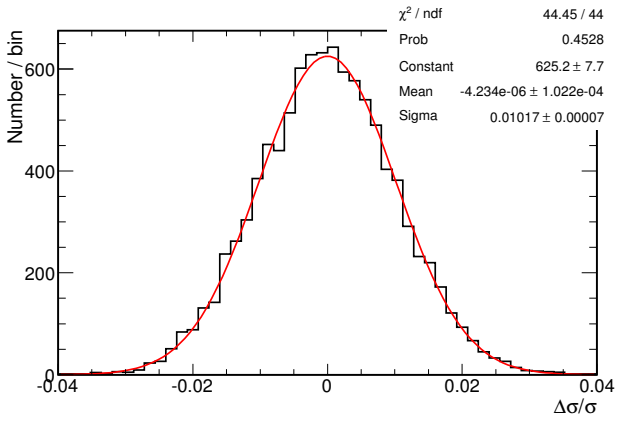

Figure 5.21: Effect of Poisson variation of simulation signal and background on the measured cross-section. The width of the distribution gives the systematic uncertainty from finite simulation statistics.

5.5 Cross-section calculation

This section describes the calculation of the cross-section measurement and comparison with previous data and neutrino interaction generator predictions.

5.5.1 Integrated flux

As explained in Section 5.2, flux tuning files for each T2K run period are used to weight the simulation in order that it matches more accurately the flux of a particular run configuration [95]. These contain predictions for the flux at the near detector site on the x, y plane within the magnet centred at the origin of ND280 coordinates. This is not identical with the plane of FGD1, but the difference is expected to be small [105]. The flux prediction histograms contained within these files are binned by neutrino energy, as shown in the left plot of Figure 5.12. Summing the bin contents gives the integrated flux per 10^{21} POT of data-taking across the full beam energy spectrum. Normalising each histogram by the total number of POT in the corresponding run as given in Table 5.1 results in a total integrated $\bar{\nu}_\mu$ flux of:

$$\phi_{\text{run2 + run3b/c + run4}} = 6.98 \times 10^{11}\,\text{cm}^{-2} \tag{5.6}$$

T2K run	Int. flux/ $10^{10}\,\mathrm{cm}^{-2}$
Run 2	9.58
Run 3b	2.90
Run 3c	16.63
Run 4	40.69
Total:	**69.80**

Table 5.13: The integrated $\bar{\nu}_\mu$ flux breakdown per T2K run.

with the breakdown of flux by run period given in Table 5.13.

5.5.2 Number of target nucleons

The calculation of the number of target nucleons in the FGD1 FV is given in full in [105] [97]. A simplification of this calculation, assuming a nucleon molar mass of 1 g/mol, gives the same result. This latter calculation will be outlined here.

The FV in this analysis is defined such that the outer five FGD1 bars in both the x- and y- directions are excluded and in the z-direction, the first layer is excluded. This leaves a FV, V_{ND}, of $9.49 \times 10^5\,\mathrm{cm}^3$. The density of the scintillator bars in the FV, $\rho_{\mathrm{scint.}}$, is calculated in [105] to be $0.963\,\mathrm{g/cm}^3$, giving a fiducial mass of $9.14 \times 10^5\,\mathrm{g}$.

For an inclusive selection, every nucleon within the FV is a potential interaction target, so the total number of nucleons is required. With the assumption of a 1 g/mol nucleon molar mass, this can be calculated by multiplying the fiducial mass by Avogadro's number, $6.022 \times 10^{23}\,\mathrm{mol}^{-1}$, giving:

$$T = 5.50 \times 10^{29}\,\text{nucleons}. \tag{5.7}$$

5.5.3 Result

Using the flux and number of targets calculated above, the efficiency and purity of the simulation given in Section 5.3 as 36.4% and 56.1% respectively, and the

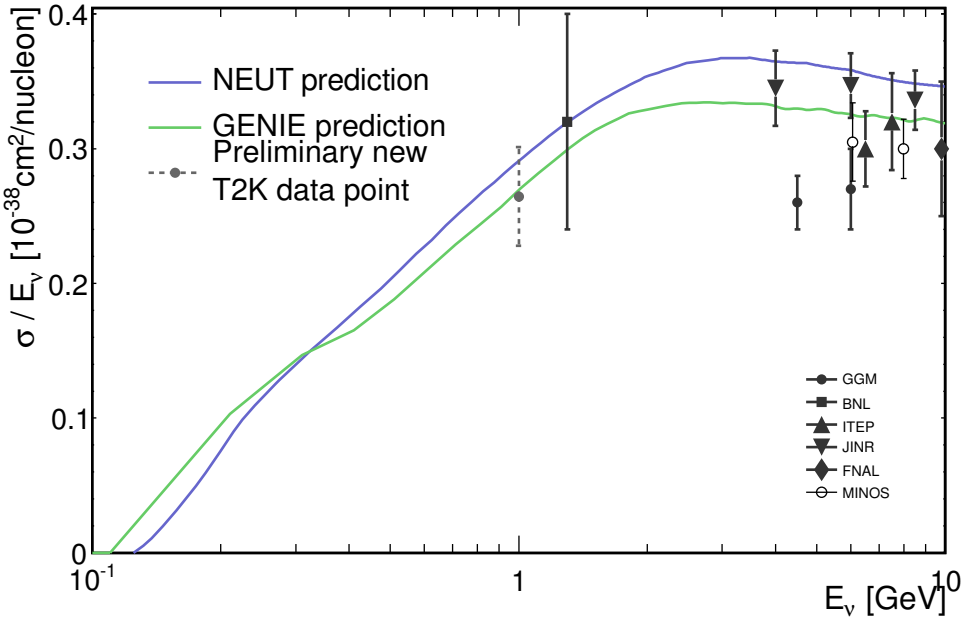

Figure 5.22: T2K preliminary data point, alongside current $\bar{\nu}_\mu$ inclusive CC measurements, with the NEUT and GENIE generator predictions.

systematic uncertainties studied in the previous section, the $\bar{\nu}_\mu$ inclusive CC cross-section is measured to be:

$$\langle \sigma_{\bar{\nu}_\mu} \rangle_\Phi = (2.72 \pm 0.03(\text{stat.})^{+0.28}_{-0.34}(\text{flux}) \pm 0.14(\text{int.}) \pm 0.14(\text{det.})) \times 10^{-39} \frac{\text{cm}^2}{\text{nucleon}}.$$

Figure 5.22 shows the preliminary T2K data point alongside current $\bar{\nu}_\mu$ inclusive CC measurements at low energy, and the NEUT and GENIE generator cross-section predictions. It can be seen that the data point agrees well with both generators at this energy, providing a valuable confirmation.

Chapter 6

Constraining the T2K Flux Using Neutrino-Electron Elastic Scattering

The neutrino beam in an accelerator-based experiment is generated by firing protons at a graphite target. The neutrinos themselves are formed in the decay of the produced pions and kaons (see Section 3.2.2), and so the total systematic uncertainty on the flux comes not only from uncertainties on the T2K beam itself: intensity, direction and target alignment, among others, but also on hadron production uncertainties, which are theoretically poorly understood.

Although the presence of a near detector in oscillation analyses partly cancels the systematic uncertainty due to the flux, no such cancelling factor can be used in the measurement of absolute cross-sections in the near detector, and, although T2K makes use of a dedicated experiment, NA61/SHINE [106], for the study of hadron production, the flux systematic still remains at a level greater than 10%. Indeed, at 12.4%, the main contribution to the systematic uncertainty in the muon antineutrino cross-section analysis described in Chapter 5 originated from the neutrino flux prediction.

This chapter presents a feasibility study of a new approach to better constrain neutrino flux uncertainties in cross-section measurements.

6.1 Neutrino-electron scattering

Neutrino interaction event rates observed by experiments are dependent on the flux, the interaction cross-section, the number of targets, and the efficiency of detection. Therefore an integrated flux normalisation constraint can be made using an interaction with a precisely known cross-section and the following relation:

$$\Phi = \frac{N}{T\sigma}, \tag{6.1}$$

where N is the number of inferred signal events, T is the number of interaction targets and σ is the cross-section. The number of inferred signal events is calculated using the number of events observed in the real data, N_{obs}, and the efficiency, ϵ, and purity, π, of selection achieved in the simulation:

$$N = \frac{\pi}{\epsilon} N_{\text{obs}}. \tag{6.2}$$

As a purely leptonic process, the cross-section for the elastic scattering of neutrinos off electrons is precisely known. Assuming that $q^2 \ll M_Z^2 c^2$ so that the simplified version of the propagator term (2.38) can be used, its spin-averaged scattering amplitude squared is [5]:

$$\langle \mid \mathcal{M} \mid^2 \rangle = 2 \left(\frac{g_Z E}{M_Z c^2} \right)^4 \left\{ (c_V + c_A)^2 + (c_V - c_A)^2 \cos^4 \frac{\theta}{2} \right\}. \tag{6.3}$$

In Equation (6.3), g_W and g_Z are numbers representing the coupling strengths, c_V and c_A are particle-dependent coefficients, and θ is the scattering angle. Fermi's Golden Rule can then be used to calculate the differential cross-section. For two-body scattering, in the centre of mass frame this states that [5]:

$$\frac{\mathrm{d}\sigma}{\mathrm{d}\Omega} = \left(\frac{\hbar c}{8\pi} \right)^2 \frac{\langle \mid \mathcal{M}^2 \mid \rangle}{(E_1 + E_2)^2} \frac{\mid \boldsymbol{p_f} \mid}{\mid \boldsymbol{p_i} \mid}, \tag{6.4}$$

where E_1 and E_2 are the energies of the incoming particles, $|\,\boldsymbol{p_i}\,|$ is the magnitude of the incoming momentum and $|\,\boldsymbol{p_f}\,|$ is the magnitude of the outgoing momentum of the particles. This gives a neutrino-electron elastic scattering differential cross-section of:

$$\frac{\mathrm{d}\sigma}{\mathrm{d}\Omega} = 2\left(\frac{\hbar c}{\pi}\right)^2 \left(\frac{g_Z}{4M_Z c^2}\right)^4 E^2 \left\{(c_V + c_A)^2 + (c_V - c_A)^2 \cos^4\frac{\theta}{2}\right\}. \tag{6.5}$$

In Equation 6.5, g_Z is dependent only on the well measured Weinberg angle, θ_W (see Section 2.5.1):

$$g_Z = \frac{e\sqrt{4\pi/\hbar c}}{\sin\theta_W \cos\theta_W}. \tag{6.6}$$

The coefficients c_V and c_A are also dependent only on the Weinberg angle (see Table 2.2), so that there are no unknown parameters in the cross-section.

For neutrino energies much larger than the electron mass, neutrino-electron scattering events are characterised by recoil electrons at very small angles to the neutrino beam direction. This can be seen by considering the two-body kinematics of the event, in which the electron mass can be safely neglected as the interaction is highly relativistic. Using the notation p_ν and p_e for the four-momentum of the incoming neutrino and electron respectively, and p'_ν and p'_e for the outgoing particles, the square of the four-momentum transfer, t, is [107]:

$$\begin{aligned} t &= (p_\nu - p'_\nu)^2 \\ &= -2p_\nu \cdot p'_\nu \\ &= -2E_\nu E'_\nu \left(1 - \cos\hat{\theta}\right) \\ &= -\frac{s}{2}\left(1 - \cos\hat{\theta}\right), \end{aligned} \tag{6.7}$$

where s is the squared invariant mass of the system, and $\hat{\theta}$ is the angle of the outgoing electron with respect to the incoming neutrino in the centre of mass frame.

This can be related to the fractional energy loss of the incoming neutrino, y. If we denote the electron energy as E, so that $p_e = (E, -\boldsymbol{p})$, then, in the centre of mass frame, the incoming neutrino momentum is $-\boldsymbol{p}$ so that:

$$\begin{aligned} y &= \frac{p_e \cdot (p_\nu - p'_\nu)}{p_e \cdot p_\nu} \\ &= \frac{(E, -\boldsymbol{p}) \cdot (0, \boldsymbol{p} - \boldsymbol{p'})}{(E, -\boldsymbol{p}) \cdot (E, \boldsymbol{p})} \\ &= \frac{|\boldsymbol{p}|^2 - \boldsymbol{p} \cdot \boldsymbol{p'}}{2E^2} \\ &= \frac{1}{2}\left(1 - \cos\hat{\theta}\right). \end{aligned} \tag{6.8}$$

Using (6.7), it follows that $t = -sy$.

Along with u, which is yet to be calculated, s and t make up the Mandelstam variables [108], which, in the case of a system of massless particles, obey the relation $s + t + u = 0$. As Lorentz invariant quantities, the Mandelstam variables can be written in any reference frame. Calculating u and writing in terms of the electron scattering angle in the lab frame, θ:

$$\begin{aligned} u &= (p_\nu - p'_e)^2 \\ &= -2(E_\nu, \boldsymbol{p_\nu}) \cdot (E'_e, \boldsymbol{p'_e}) \\ &= -2\left(E_\nu E'_e - |\boldsymbol{p_\nu}||\boldsymbol{p'_e}|\cos\theta\right) \\ &= -2E_\nu E'_e\left(1 - \cos\theta\right). \end{aligned} \tag{6.9}$$

Using $s + t + u = 0$, and substituting for $t = -sy$:

$$\begin{aligned} s\left(1 - y\right) + u &= 0 \\ u &= -2m_e E_\nu\left(1 - y\right) \\ 2E_\nu E'_e\left(1 - \cos\theta\right) &= 2m_e E_\nu\left(1 - y\right) \\ E'_e\left(1 - \cos\theta\right) &= m_e\left(1 - y\right). \end{aligned} \tag{6.10}$$

Using the small angle approximation for $\cos\theta$, this becomes:

$$E'_e\theta^2 = 2m_e\,(1-y)\,. \tag{6.11}$$

As y can only take values between 0 and 1, the constraint exists that $E'_e\theta^2 < 2m_e$. So, for example, for an incoming neutrino of energy 1 GeV, the outgoing electron is constrained to be ejected within approximately 2° to the initial neutrino direction. This is a very important result as it can be exploited when attempting to isolate these events.

6.2 Isolating a neutrino-electron scattering sample

Unfortunately, the neutrino-electron elastic scattering cross-section is on the order of $10^{-42}\,\mathrm{cm}^2$ [109]. This is 10^3–10^4 times lower than neutrino-nucleon interactions. Indeed, the neutrino-electron scattering cross-section is so low that the NEUT generator does not simulate it; in this study, GENIE [110],[1] an alternative neutrino event generator used often by T2K and many other neutrino physics experiments, will be used. Due to the low interaction rate, and to the final state electron kinematic constraint calculated in Section 6.1, the ideal detector for the isolation of this signal must strike a balance between target mass on the one hand, and angular and energy resolution on the other. The ND280 P0D (see Section 3.3.3) has a fiducial mass of $5393.22 \pm 0.56\,\mathrm{kg}$ [111] (providing approximately three times as many target electrons as both FGDs combined). Additionally, though it is less fine-grained than the FGDs, the triangular bars of the P0D ensure that the angular resolution remains at a reasonable level; the electron angular resolution has been found to be approximately 2.5° [112]. This bar shape makes it less likely for a particle to hit just a single column of bars. If neighbouring bars are hit, the ratio of charges deposited in the bars can be used to aid in hit position resolution. These characteristics, along with the 15–16% electron energy resolution provided by the P0D [113], make it the subdetector of choice for this study.

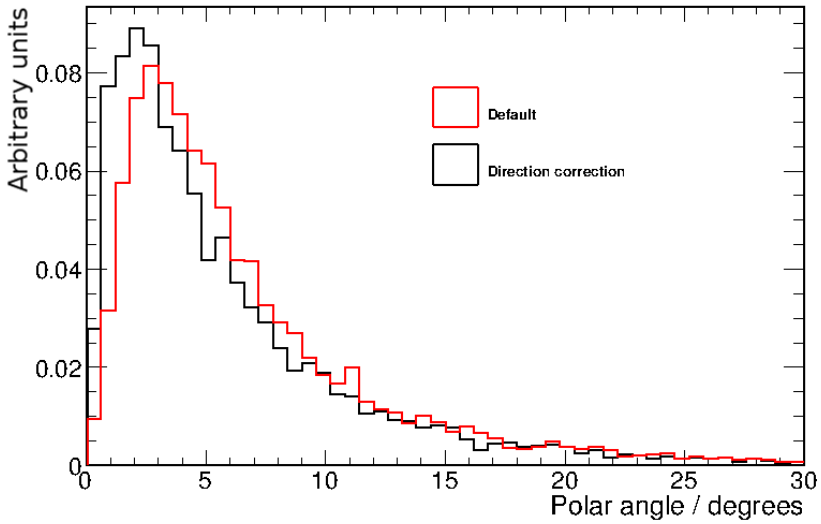

Figure 6.1: Effect of the correction for the difference between the ND280 z-axis definition and the true neutrino direction peak on neutrino-electron elastic scattering events.

6.2.1 Neutrino direction correction

Before continuing, it should be noted that a small correction is made prior to the analysis. In the ND280 coordinates, the z-axis is defined along the central axis of the detector. However, as the ND280 is off-axis, we know that the neutrino beam is slightly askew from this. For many analyses this effect will be negligible. For the current analysis, however, the signal is characterised by very small polar angles, as noted in Section 6.1, and, as will be seen, this characteristic is utilised in the selection. The neutrino beam direction distribution peaks at approximately 1.7° from the z-axis [77].[2] We therefore correct all angles used in the analysis from this point onwards; angles are measured with respect to the true neutrino beam peak, rather than the z-axis of the detector. The effect of this correction on the reconstructed polar angle of signal events is shown in Figure 6.1.

6.2.2 Multivariate analysis

Consideration of the low signal event rate amongst a much larger background determined that a multivariate analysis (MVA) would be the most viable option in

[1] Generates Events for Neutrino Interaction Experiments.
[2] For neutrinos within the FGD1 fiducial volume as defined in Chapter 5.

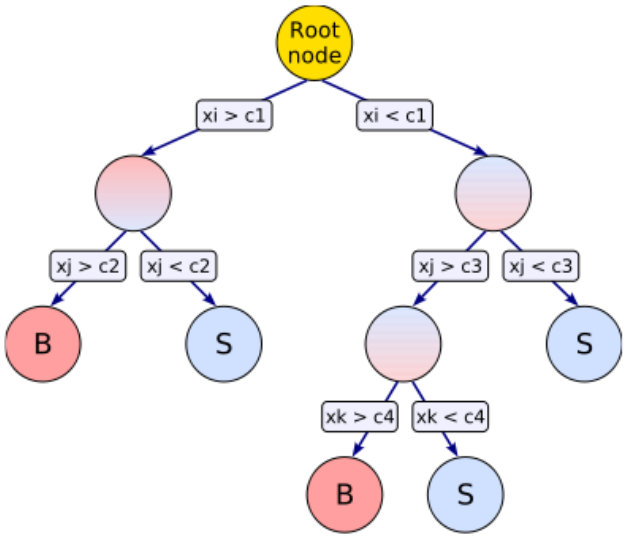

Figure 6.2: Example of the creation of a single decision tree. At the root node the data is split into signal and background enhanced regions using the most powerful separating variable, x_i. The split occurs at the optimal value, c_1, to best enhance the signal or background in each region. The same analysis is then carried out on the data within each of these regions separately, and the method is repeated until 'leaves' of signal dominated and background dominated regions are formed. Image from [115].

isolating neutrino-electron elastic scattering events. Whereas the standard rectangular cuts-based analysis removes background by looking at the distribution of events in a single variable at a time, and then separating along a certain value of that variable, the multivariate technique can consider all variables simultaneously. By doing this functions of the variables, even non-linear functions, can be used in place of rectangular cuts, which is far more effective when correlations exist between variables. Additionally, MVA techniques are extremely useful when the separation between signal and background is small: a 'boosting' method can be implemented in which the MVA analysis technique can be repeated on a reweighted sample of events, where the weights originate from the results of previous iterations of the technique. In this way, a majority-vote decision can be made on whether each event should be classified as signal or background. The method of boosted decision trees falls into this latter category [114], and, as part of the ROOT TMVA framework [115], is the MVA technique employed in the current analysis.

Boosted decision trees

A single decision tree is created by making successive splits on a sample of data one variable at a time, as can be seen in Figure 6.2. The user inputs a training sample of signal and background events, each of which has a certain value in each of the intended separating variables, x_α. By scanning all possible split values for each of the variables, the variable with the best separation power (according to a certain performance measure, or figure of merit) is found. This variable (x_i in Figure 6.2) and its optimum cut value (c_1) make up the first split in the data, or the 'root node', leaving one region enriched with signal and one with background. For the signal and background regions that this separation produces independently, the next best separating variable is calculated and the same procedure is followed, resulting in two signal and two background enriched regions. This is repeated until a certain stopping criterion is fulfilled[3] and the training sample contains regions, known as leaves, dominated by signal or background.

To increase the algorithm performance, in addition to making it more robust against statistical fluctuations, the training sample can be 'boosted', or reweighted based on the outcome of the decision tree, and a repeat of the method performed. There are many boosting algorithms, but the most popular, and the one used in the current analysis, is AdaBoost (adaptive boost) [116]. Using this algorithm, all those events that were misclassified previously have an increased weight applied in the generation of the new decision tree. The boost weight, α, is defined as:

$$\alpha = \frac{1 - err}{err}, \tag{6.12}$$

where err increases with a greater misclassification rate in the tree and is restricted to be within the range $0 < err \leq 0.5$.[4] The reweighted sample results in different optimal separation values (assuming the variable had some separation power in the first place), so that some of the misclassified events will this time be classified correctly. In this way, boosting can occur many times over, producing a forest of single decision trees.

[3] This can be that there are a minimum number of events in the region, that the region contains purely signal or background events, or that a specific user-defined set of separations have already been placed.

[4] err is calculated as the sum of the misclassified event weights divided by the sum of all the event weights.

The real data in the analysis are passed through every tree in the forest created during training. The final classifier value is given by:

$$y\left(\mathbf{x}\right) = \frac{1}{N_{trees}} \sum_{i}^{N_{trees}} \ln\left(\alpha_i\right) h_i\left(\mathbf{x}\right) \tag{6.13}$$

where $h\left(\mathbf{x}\right)$ is the result from each tree,[5] and is equal to $+1$ for signal leaves and -1 for background leaves.

6.2.3 Projected event numbers

The expected number of true[6] signal interactions in the P0D fiducial volume by the end of the T2K full data-taking period can be found by integrating the product of the integrated flux and the known cross-sections across true neutrino energy, and multiplying by the number of interaction targets:

$$N = N_{\mathrm{T}} \int \Phi(E_\nu)\sigma(E_\nu)\mathrm{d}E_\nu. \tag{6.14}$$

Based on the proposal of five years of T2K data-taking with the J-PARC accelerator operating at its design power of 750 kW, it is predicted that a total of 7.8×10^{21} POT will be delivered [117]. Flux histograms per 10^{21} POT are provided by the T2K beam group [91]; by integrating these and taking into account the total projected POT the integrated fluxes of the various neutrino flavours during the proposed T2K running time can be calculated. These are given in Table 6.1.

Neutrino-electron scattering cross-sections, as purely leptonic interactions, are very precisely known. These are shown for each neutrino flavour in Table 6.1. Electron neutrinos have by far the largest cross-section; this is due to the additional charged-current Feynman diagram that results in the same final state as the neutral-current scatters, as shown in Figure 6.3.

The number of target electrons, N_{T}, can be estimated as follows. The number of nucleons in the fiducial volume can be found by multiplying the fiducial mass by

[5] $\mathbf{x}$ is the input variable vector.
[6] i.e. before the efficiency of selection is taken into account.

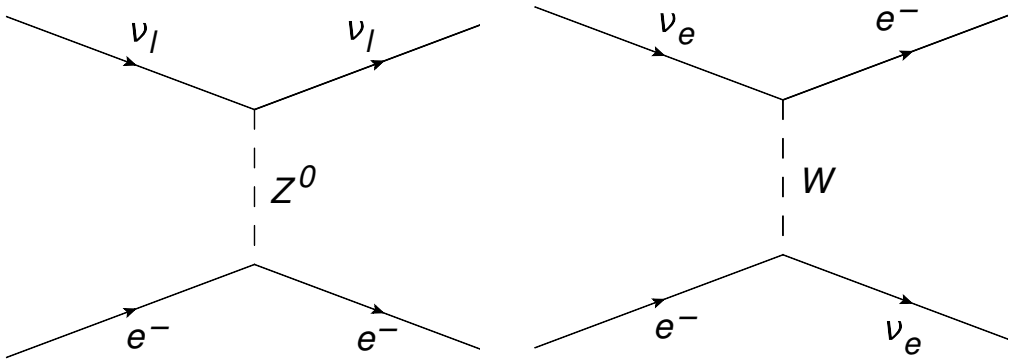

(a) (b)

Figure 6.3: Feynman diagrams depicting (a) neutral-current neutrino elastic scattering from electrons, and (b) the additional Feynman diagram available to electron neutrinos.

Neutrino flavour	Cross-section $[\times 10^{-42}\text{cm}^2\,(E_\nu/1\,\text{GeV})]$	Total integrated flux $[\times 10^{12}\text{cm}^{-2}]$	Expected no. events
ν_e	9.5	1.79	37
$\bar{\nu}_e$	4.0	0.24	3
ν_μ	1.6	151	335
$\bar{\nu}_\mu$	1.3	9.48	20
			Total: 395

Table 6.1: Neutrino-electron scattering cross-sections for each neutrino flavour, the integrated flux at the near detector after the total expected T2K exposure of 7.8×10^{21} POT, and the number of signal interactions in the P0D fiducial volume that this is expected to produce.

Avogadro's number, giving 3.25×10^{30} nucleons. Making the simplifying assumption that half of these are protons, the number of electrons in the fiducial volume is estimated to be 1.62×10^{30}. A full calculation of the number of electrons in the P0D fiducial volume would require detailed information on the make-up of the detector components, and will not be attempted for this feasibility study.

Putting these numbers into Equation (6.14) gives the expected event numbers shown in Table 6.1. It can be seen that close to 400 signal events are expected over the full projected running time of T2K. At the time of analysis completion, 6.39×10^{20} POT has been delivered to the target station resulting in an expected signal count in the available data set of approximately 32 events.

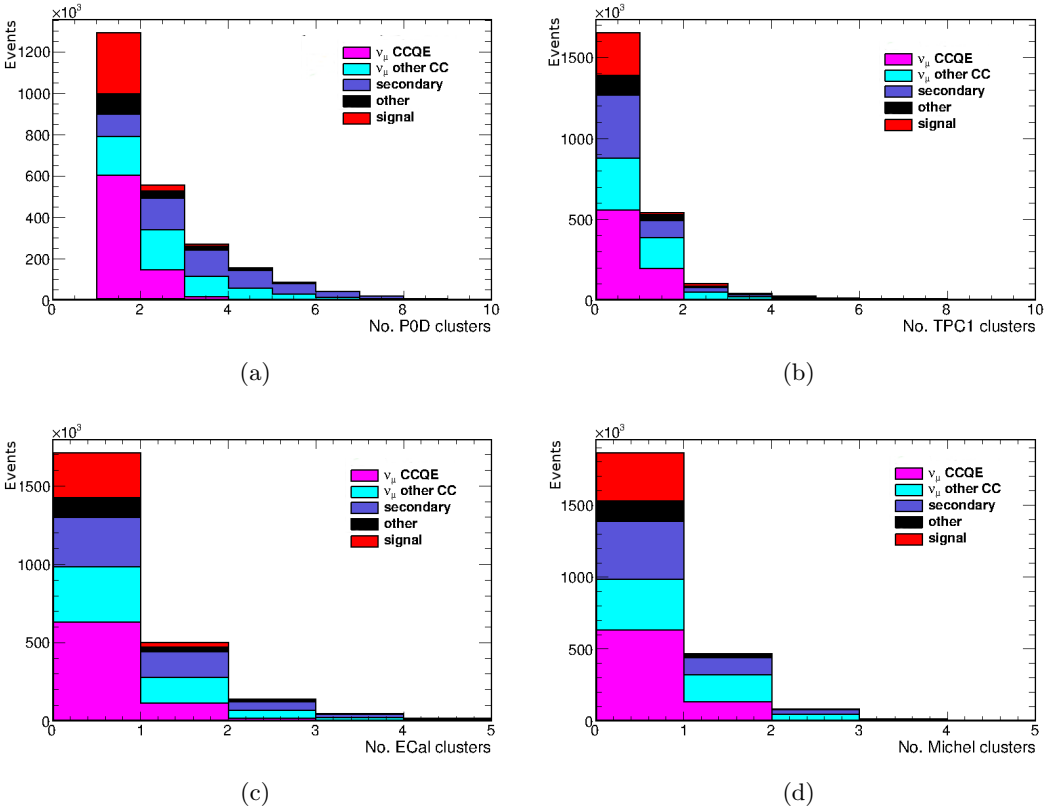

Figure 6.4: Analysis preselection criteria. No cuts have been placed on distributions. Signal has been increased by a factor of 500 for visibility.

6.2.4 Event selection

Multivariate analyses require a large statistics training sample. For this analysis, the GENIE-based event generation driver [118] was used to generate 10000 neutrino-electron scattering events in the P0D fiducial volume, according to the predicted neutrino flux at the off-axis near detector. These events were then combined with approximately 5×10^{21} POT equivalent of full-spill T2K simulation to create the training sample.

In order to enter the multivariate selection, a set of initial pre-selection criteria must be satisfied:

- **Data quality:** The full spill must have both a good ND280 data quality and a good beam data quality flag. See Section 5.3 for more details.
- **Bunching:** The selection then runs on each of the eight T2K bunches separately. See Section 5.3 for more details.

Edge	x (mm)	y (mm)	z (mm)
Max.	764.0	869.0	-1264.0
Min.	-836.0	-871.0	-2969.0

Table 6.2: Positions of the P0D fiducial volume edges, as used in [119].

- **Track selection:** There must be a reconstructed track that originates in the P0D fiducial volume, where this is defined in Table 6.2. Additionally, there must only be a single object with a component in the P0D, as shown in Figure 6.4(a).
- **TPC1 veto:** Signal electrons produce electromagnetic showers, and the vast majority of these do not enter the TPC immediately downstream of the P0D. Muon events, however, are much more likely to enter the TPC, as shown in Figure 6.4(b). Therefore, it is required that there is an absence of any objects with components in TPC1.
- **ECal veto:** There must not be any reconstructed clusters in any of the ECal modules. The electron candidate must be wholly contained within the P0D. This requirement ensures that events that begin in the ECal and enter the P0D through the side are not included. See Figure 6.4(c).
- **Michel electron cluster veto:** There must not be any Michel electron clusters. A Michel electron cluster is assumed by the P0D reconstruction if there are two or more delayed hits of at least 4.5 photon equivalent units (PEU) in a cylinder surrounding the reconstructed object [119]. See Figure 6.4(d).

Events that satisfy all of the above criteria are then passed in to the MVA selection stage.

6.2.5 Input variables

In order to train and evaluate the MVA, the following variables are used.

- $\mathbf{E\theta^2}$: As explained in Section 6.2, signal interactions are limited to small values of this variable. This is shown in Figure 6.5(a). The energy is reconstructed assuming an electromagnetic shower. This is estimated by summing the attenuation-corrected charge of the object nodes.
- **Vertex activity:** Signal events are purely leptonic and therefore have a very

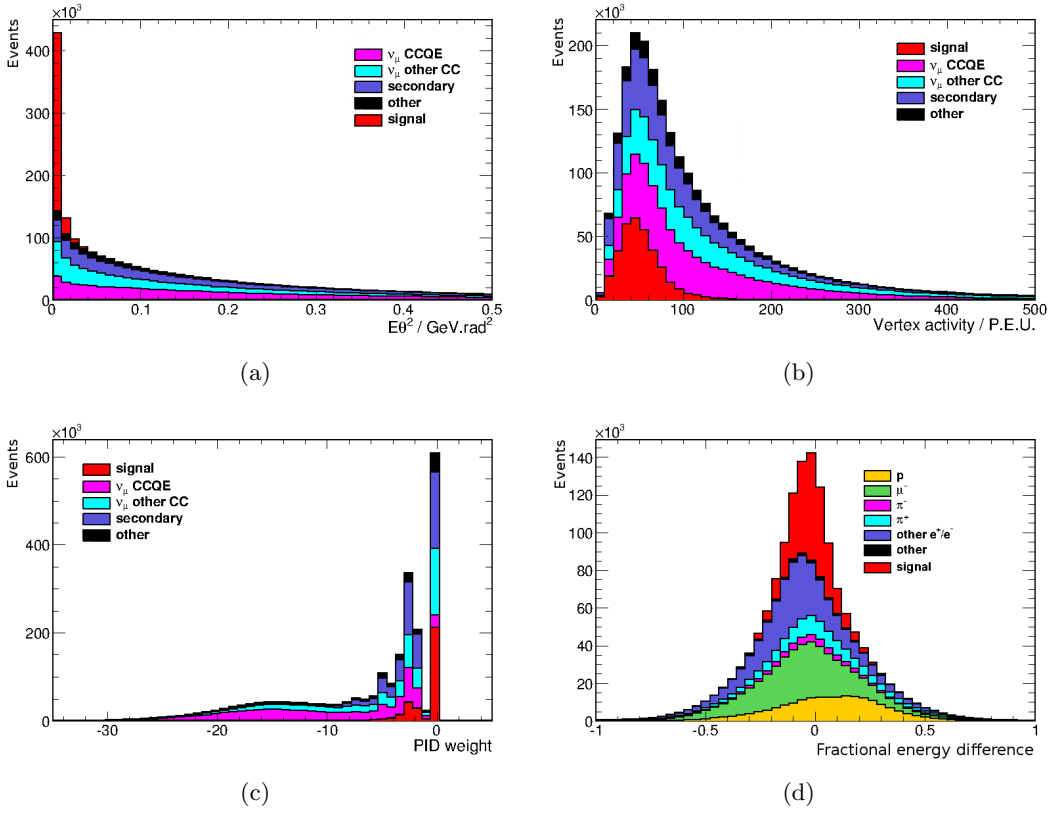

(a) (b)

(c) (d)

Figure 6.5: Distributions included in the MVA method. No cuts have been placed on distributions. Signal has been increased by a factor of 500 for visibility. Note that (d) is stacked by particle type in order to show the separation power.

clean interaction vertex. On the other hand, many background events will contain clumps of charge around the vertex due to hadronic interactions. The T2K software saves single hit information for the first two hits in the reconstructed track; this variable estimates the activity around the interaction vertex by summing the charges of these two hits. The vertex activity distribution in PEU is shown in Figure 6.5(b).

- **PID weight:** The P0D reconstruction processes all three-dimensional tracks and determines the most likely original particle. This is done by a Kalman filter which assesses the likelihood of a track originating from a photon or electron, a light track (typically, a muon) and a heavy track (a proton). Tracks are also processed by a parametric fitter and the likelihood of being some 'other' particle hypothesis is calculated [120]. The PID weight variable is then constructed by taking the difference between the log likelihood of being a photon or an electron and the log likelihood of being some 'other' particle [120], and is shown in Figure 6.5(c).

- **Fractional energy difference:** P0D showers are composed of three or more contributing clusters. A variable based on deposited energy that has some separation between photons or electrons, muons, and protons is then produced by looking at the fractional energy difference between the first and last clusters in the shower:

$$\frac{\text{last cluster energy deposit - first cluster energy deposit}}{\text{total shower energy deposit}}. \tag{6.15}$$

MIP-like particles that leave the detector deposit energy uniformly along the length of the track, leading to a fractional energy difference variable centred at zero. Stopping particles deposit a significant amount of energy at the end of the track leading to a positive value of the fractional energy difference, whereas electron showers deposit more energy at the front resulting in a value less than zero, as shown in Figure 6.5(d).

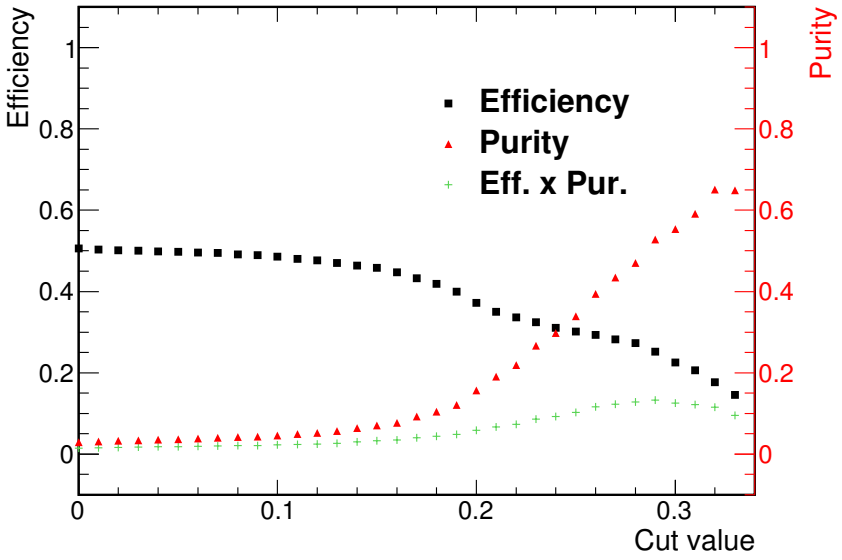

Figure 6.6: Optimisation of the output BDT variable cut value. Square black markers show the efficiency of selection, red triangles the purity, and green crosses indicate the figure of merit at that cut value, which is taken to be the product of efficiency and purity.

6.3 Performance

The efficiency and purity of selection are defined as follows:

$$\epsilon \equiv \frac{\text{selected true } \nu\text{-}e^- \text{ elastic scattering interactions occurring within P0D FV}}{\text{all true } \nu\text{-}e^- \text{ elastic scattering interactions occurring within P0D FV}},$$

$$\pi \equiv \frac{\text{selected true } \nu\text{-}e^- \text{ elastic scattering interactions occurring within P0D FV}}{\text{all selected interactions}}. \tag{6.16}$$

The separation value on the BDT output was optimised to maximise the product of efficiency and purity, as shown in Figure 6.6. At the cut value of 0.29, which gives the highest figure of merit ($\epsilon \times \pi$), the efficiency and purity of selection are predicted to be $\epsilon = (25.2 \pm 0.3)\%$ and $\pi = (52.8 \pm 1.0)\%$ respectively, giving approximately 100 expected signal events in a sample of approximately 190 events. The background in

Particle	Fraction
Signal	52.8%
Other $e^{\pm}$	43.1%
$\mu^{\pm}$	3.3%
Other	$< 1\%$

Table 6.3: Composition of final simulated data sample by particle type.

Interaction	Fraction
Signal	52.8%
Secondary $e^{\pm}$	30.7%
ν_e CCQE	9.1%
ν_e other CC	1.7%
ν_μ CCQE	2.5%
ν_μ other CC	$< 1\%$
$\bar{\nu}_e/\bar{\nu}_\mu$	$< 1\%$
OOFV (non $e^{\pm}$)	$< 1\%$
Other	$< 1\%$

Table 6.4: Composition of final simulated data sample by interaction.

the selected sample is composed almost entirely of electrons from interactions other than neutrino-electron elastic scattering; many of these are electrons coming from photon conversion, as shown in Tables 6.3 and 6.4.

6.4 Predictions of systematic uncertainties on total flux

A measurement of Φ, the total integrated flux of all neutrino flavours, or flux normalisation, can be extracted using the following:

$$\Phi = \frac{N^{\text{obs}}\pi}{\epsilon T} \sum_i \frac{1}{\sigma_i f_i} \tag{6.17}$$

where i runs over the neutrino flavours in the T2K beam. In this equation, N^{obs} is the observed number of events, ϵ and π are the efficiency and purity of signal selection respectively and T is the number of target electrons. σ_i is the theoretical calculation of the cross-section of a single neutrino flavour, and f_i is the fraction of the total flux that comes from that flavour. This equation gives the total flux, the sum of contributions from all neutrino flavours. This means that in the calculation the sum over the product of cross-section components and their relative beam fraction is required.

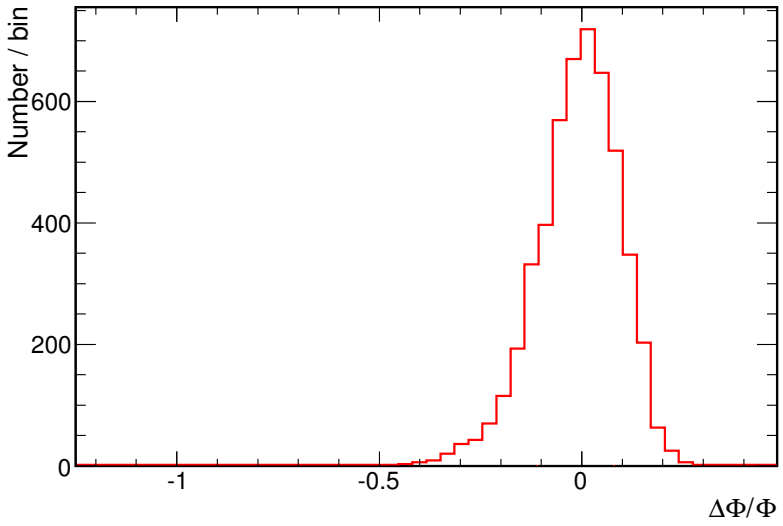

Figure 6.7: Effect on the flux normalisation of varying the contributing fluxes.

6.4.1 Flux

The flux fractions, f_i, in Equation (6.17) have an associated uncertainty, so a flux systematic uncertainty has to be assigned. Similarly to the $\bar{\nu}_\mu$ analysis presented in Chapter 5, the uncertainty due to the T2K flux predictions is evaluated by throwing flux weights 5000 times. For each throw, 25 weights are generated, each weight applying to all events in a single neutrino flavour, energy bin (see Section 5.4.1) and therefore corresponding to a slightly increased or decreased flux for that particular neutrino flavour component in the energy range of that bin. The weights are generated in accordance with the flux covariance matrix provided by the T2K beam group [95], and are applied to each signal and each selected event so that the efficiency, ϵ, and purity, π, of selection can be recalculated every time a throw is completed. Additionally, as the purpose of this systematic is to emulate the effect of a change in flux on the measurement, each neutrino flux fraction, f_i (Equation (6.17)), must be recalculated for each throw. It can be seen that these appear multiplied by the cross-section, which are functions of energy. These are found, therefore, for each throw, by summing all neutrino energy bin weights for each neutrino flavour, multiplying by the cross-section at the central point of that energy bin and normalising so that the sum of fractions is equal to one.

The fractional difference from the nominal flux normalisation value is plotted for every throw, and the width of the resulting distribution, shown in Figure 6.7, is

taken as the systematic uncertainty. The distribution is slightly asymmetric, with upper and lower values $+10.1, -10.7\%$. The largest of the two values, 10.7%, is taken as the systematic uncertainty.

6.4.2 Interaction modelling

Although the neutrino-electron scattering cross-section is very precisely known, the selected sample will consist of approximately 50% events for which cross-sections are far less well known. As with the NEUT generator, GENIE uses parameters in the modelling of interactions, and uncertainties associated with these parameters have also been provided, based most often on comparisons with experimental data or on the differences between two sets of experimental data [121]. These parameters can generally be divided into several categories: form factors, or similar parameters affecting the fundamental neutrino cross-section models; parameters dealing with intranuclear rescattering within the nucleus, which are termed final state interactions; and those affecting hadronisation and decays of intermediate particles. The parameters considered in this analysis that have a non-negligible effect on the total interaction modelling uncertainty are shown in Table 6.5.

The systematic is evaluated using the same reweighting tool as was used in the previous chapter (see Section 5.4.2). Each true signal event and each selected event is weighted so that the total sample appears the same as if the underlying parameters had had a different value. In this way, the parameters are varied individually by $\pm 1\sigma$ and the effect of the differing purity and efficiency of this new physics sample on the flux constraint, Equation (6.17), is found.[7] These variations are shown in Figure 6.8. The largest of the positive and negative variations on the flux constraint is taken as the systematic uncertainty due to that parameter.

In addition to known model systematic errors, there are indications in the data that ill-understood nuclear processes are also active. These are not included in the GENIE model, but could have an effect on sensitive variables such as vertex activity. There is some evidence from the MINERνA experiment that an extra low energy proton is ejected in approximately 25% of interactions with neutron targets [122]. The effect on the vertex activity due to the possible addition of another particle cannot be studied by a reweighting method, so a further systematic study has been conducted to ensure that this has a minimal effect on the analysis. An estimate of

[7] Note, for this systematic, the fractions of each neutrino flavour, f_i, are taken from the fluxes given in Table 6.1, and are not varied. In addition, the cross-sections, σ_i, are assumed to be known exactly, and are not varied.

Parameter	GENIE code	Nominal value	Fractional error
Axial mass in CCQE axial form factor	GXSec_MaCCQE	0.99	0.25
Choice of CCQE vector form factor (BBA05/Dipole)	VecFFCCQEShape	BBA05	Alternate model
Scale for the CC $\nu p 1\pi$ non-resonant background	GXSec_RvpCC1pi	1.0	0.5
Scale for the CC $\nu p 2\pi$ non-resonant background	GXSec_RvpCC2pi	1.0	0.5
Scale for the CC $\nu n 1\pi$ non-resonant background	GXSec_RvnCC1pi	1.0	0.5
Scale for the NC $\nu n 1\pi$ non-resonant background	GXSec_RvnNC1pi	1.0	0.5
Scale for the NC $\nu n 2\pi$ non-resonant background	GXSec_RvnNC2pi	1.0	0.5
Pion Feynman-x PDF for N states in AGKY (hadronisation model)	GHadrAGKY_xF1pi	1.0	0.2
Pion transverse momentum PDF for N states in AGKY (hadronisation model)	GHadrAGKY_pT1pi	1.0	0.3
Hadron formation zone length	GHadrNucl_FormZone	0.34	0.5
Nucleon mean free path (total rescattering probability)	GINuke_MFP_N	1.0	0.2
Pion charge exchange probability	GINuke_FrCEx_pi	1.0	0.5
Pion elastic scattering probability	GINuke_FrElas_pi	1.0	0.1
Pion inelastic scattering probability	GINuke_FrInel_pi	1.0	0.4
Pion absorption probability	GINuke_FrAbs_pi	1.0	0.2
Nucleon charge exchange probability	GINuke_FrCEx_N	1.0	0.5
Nucleon elastic scattering probability	GINuke_FrElas_N	1.0	0.3
Nucleon inelastic scattering probability	GINuke_FrInel_N	1.0	0.4
Nucleon absorption probability	GINuke_FrAbs_N	1.0	0.2
Pion production probability for nucleons	GINuke_FrPiProd_N	1.0	0.2
CCQE Pauli suppression (via changes in Fermi level)	CCQEPauliSupViaKF	1.0	0.35

Table 6.5: GENIE interaction parameters that contribute to the systematic uncertainty associated with the analysis.

the detector response to single protons was made using CCQE interactions occurring in the P0D; half of the activity was assumed to be coming from the outgoing proton, so that the event-by-event vertex activity values could be halved to give the proton response. The MINERνA study concluded that approximately 25% of interactions on neutrons may eject an additional proton, so for 12.5% of the events on nucleon targets,[8] a random number distributed according to the proton response estimate was generated and added to the nominal vertex activity. The effect of adding this response to the nominal vertex activity is shown in Figure 6.9. The analysis sample was then retrained with the modified vertex activity and the selection performance reevaluated. The modified analysis resulted in a selection efficiency and purity of $(25.2 \pm 0.3)\,\%$ and $(53.2 \pm 1.0)\,\%$ respectively, leading to a fractional change in the flux measurement, $\frac{\Delta\Phi}{\Phi} = (0.8 \pm 1.0)\,\%$. Being consistent with zero, this possible uncertainty is ignored in the calculation of the total systematic uncertainty.

The total interaction modelling uncertainty is found by quadratically summing the uncertainty from each simulation parameter, giving 2.9%.

6.4.3 Detector systematics

Detector systematics cover the lack of total understanding of the detectors used in physics analyses; that is, these systematics cover the differences in selection performance between real data and simulation, and will therefore be software dependent. As this software continually improves it is unrealistic for a feasibility study of an analysis to be conducted at the end of T2K data taking to study detector systematics as they are at present. It is almost certain that any current issues in the reconstruction algorithms will be corrected, and the detector will be better understood. It will therefore suffice at this stage to use the detector systematics already found in another P0D analysis, as a very conservative estimate of what can be achieved in the current analysis in the future. A selection of ν_μ charged-current events, completed in August 2013 with data from T2K runs 1 and 2, estimates a detector systematic difference of 2.3% [123], and this value will be used here.

Using these estimates of the systematic uncertainties, combined with the statistical uncertainty based on the expected number of events, the total uncertainty on a future measurement of the total T2K flux amounts to 13.5%. This information is summarised in Table 6.6.

[8] The assumption is that half of the nucleon targets are neutrons.

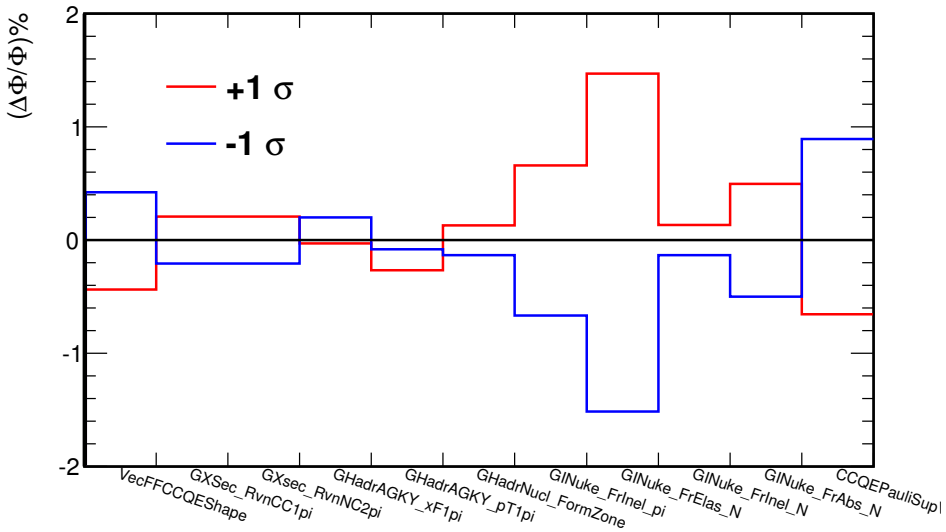

Figure 6.8: Effect on the flux normalisation of varying underlying interaction parameters. Parameters whose variation give a smaller than 0.1% effect on the flux are not shown for clarity.

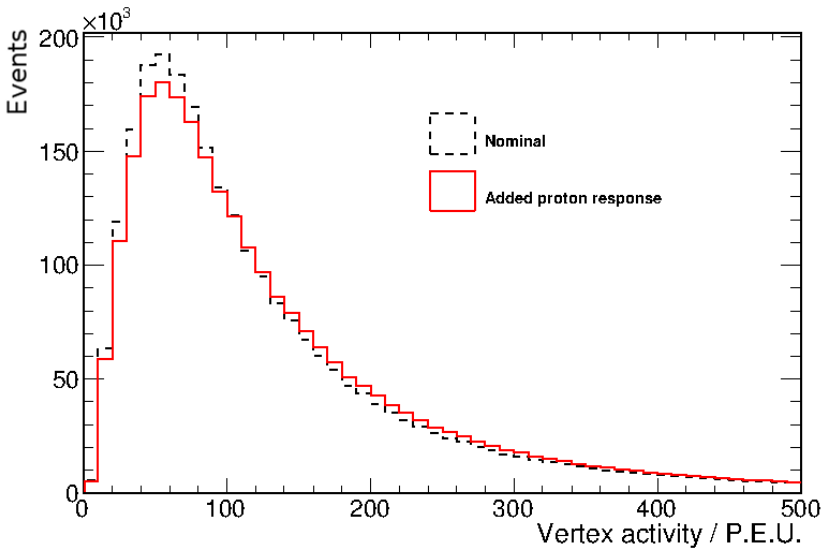

Figure 6.9: Effect on the vertex activity of adding the estimated response from an additional ejected proton to 25% of interactions on neutron targets. The figure shows all background events in the selection sample.

Source	Uncertainty (%)
Statistics	7.3
Flux	10.7
Interactions	2.9
Detector	2.3
Total:	**13.5**

Table 6.6: Contributions to the total flux measurement uncertainty.

6.5 Constraining the $\bar{\nu}_\mu$ flux

The largest systematic uncertainty in the analysis outlined in Chapter 5 originates in the T2K $\bar{\nu}_\mu$ flux prediction, so a constraint on this particular component of the flux would be very useful for that measurement. Individual flux components can be constrained by exploiting the correlations between the flux parameters.

A likelihood fit to the flux weight parameters was implemented to see how much the flux components could be constrained using the results found in Section 6.4. As can be seen from Equation (6.17), the observed number of events in this analysis is dependent on the flux bin fractions, f_i, the total flux normalisation, and the efficiency and purity of selection. The expected observed number of events was calculated using the prefit central values of the flux bin weights. The fit then maximised the likelihood by simultaneously varying the flux bin fractions such that they obeyed their correlations within the flux covariance matrix. The total flux normalisation was allowed to float within the error found in Section 6.4, and the efficiency and purity could vary within their statistical errors, resulting in fitted values for the flux bins. Five hundred throws were then made using the postfit flux weight parameters contributing to each flux component to calculate the error on that component.

6.5.1 Fit stability

In order to verify that the fitter was performing as expected, the fit was repeated 500 times with the observed number of events varying according to Poisson statistics. The pull distributions of all 25 of the flux parameters were then plotted. For a stable and unbiased fit, a pull distribution should by construction be a symmetric

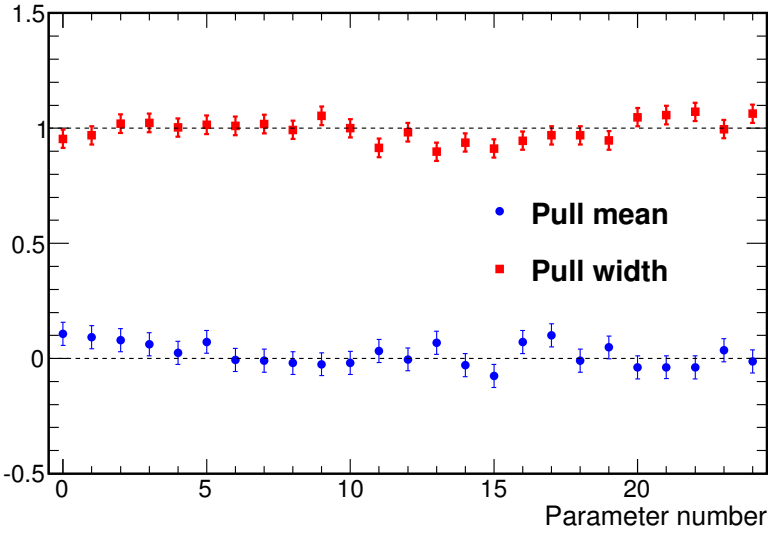

Figure 6.10: Fitted pull parameters of the 25 flux weight distributions after 500 throws of the fitter.

Gaussian with a mean at zero and a width of one. As can be seen in Figure 6.10, where the fitted mean and widths of all 25 pull distributions are summarised, these are indeed consistent with the values expected, implying that the fit is performing well with no bias. A selection of the original pull distributions are also given in Figure 6.11.

6.5.2 Results

Table 6.7 shows the constraints that can be placed on the flux component uncertainties using this fitter. It can be seen that, assuming 7.8×10^{21} delivered POT, the $\bar{\nu}_\mu$ flux uncertainty can be reduced by a factor of two. Moreover, as the neutrino-electron elastic scattering analysis predominantly selects muons originating from ν_μ (as this is the largest flux component of the T2K beam, see Table 6.1) there is a higher sensitivity to this component, and the work conducted suggests that a reduction of the flux uncertainty to a quarter of its current level can be achieved.

These results can be propagated through the calculation of the $\bar{\nu}_\mu$ inclusive CC cross-section measurement presented in Chapter 5. Using the nominal flux covariance matrix, the correlation matrix was created by dividing each element by the relevant parameter prefit standard deviations. By then multiplying each element by the relevant new parameter standard deviations (i.e. the parameter constraints

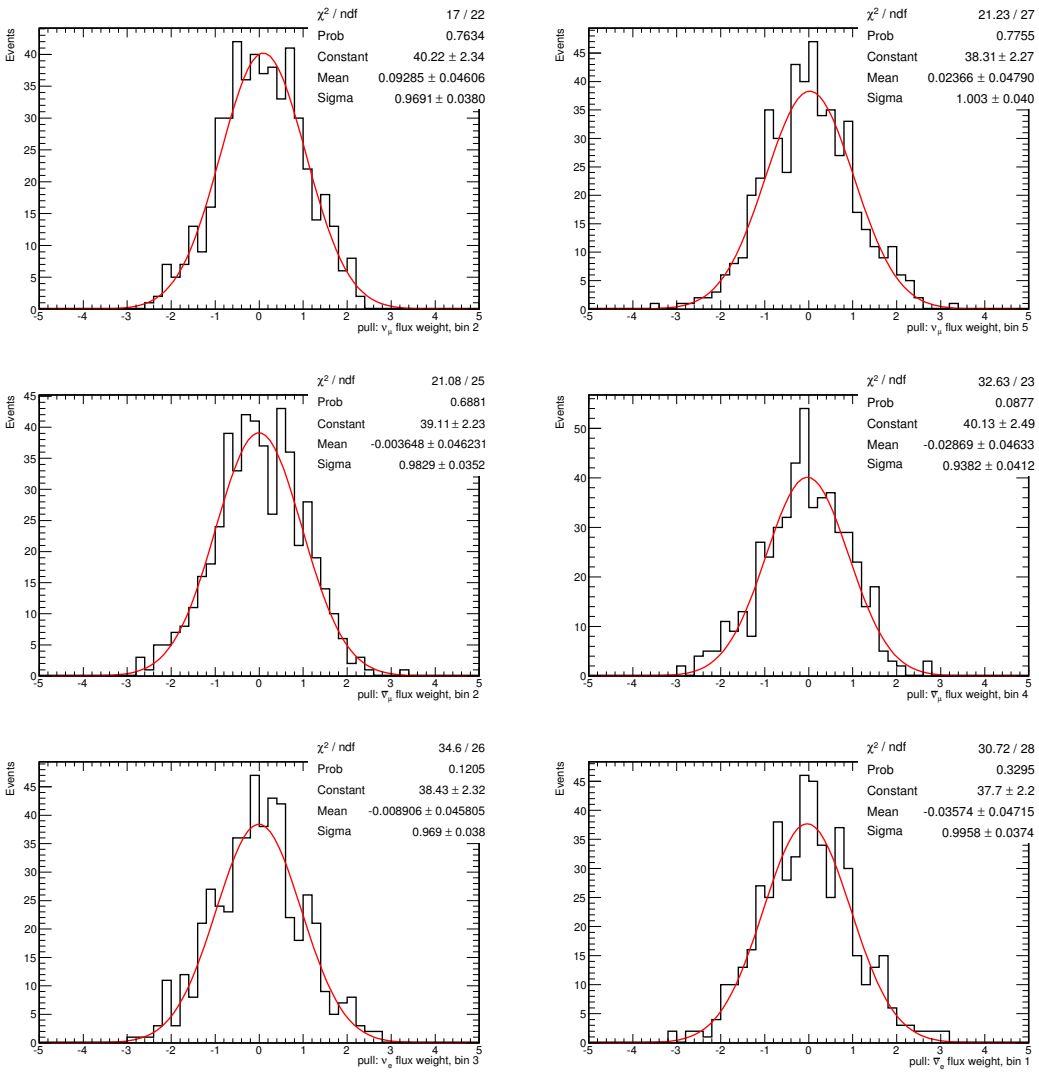

Figure 6.11: Fitted pull distributions of 500 throws of a selection of the flux parameters.

Flux component	Prefit uncert. (%)	Postfit uncert. (%)
ν_μ	12.1	3.3
$\bar{\nu}_\mu$	11.8	6.1
ν_e	11.1	3.6
$\bar{\nu}_e$	15.8	12.2

Table 6.7: Flux component uncertainty reduction due to a fit to the number of observed neutrino-electron elastic scattering events. The fit assumes a delivery of 7.8×10^{21} POT

found in the current study), a covariance matrix that incorporates the new constraints on the flux parameters was constructed. The improved flux systematic uncertainty is calculated by repeating the method outlined in Section 5.4.1. A 25-dimensional Gaussian is generated with correlations set by the modified covariance matrix. For each of 10000 throws a dataset is generated according to this Gaussian, and these points are used to reweight every selected event and every true $\bar{\nu}_\mu$ CC event. The flux weights themselves are also saved and used, in order to calculate the total simulated $\bar{\nu}_\mu$ flux of that throw. The flux, the efficiency and purity of the modified simulation are then used to extract the fractional change in the cross-section measurement.

The distribution of the fractional difference in $\bar{\nu}_\mu$ inclusive CC cross-section is shown in Figure 6.12. As in the original analysis, the uncertainty is taken to be the widths such that each tail contains 16% of the throws. These widths are -4.5% and $+5.3\%$, and the largest of the two is taken as the systematic uncertainty. This can be compared to the 12.4% uncertainty found in the nominal analysis, indicating that an improvement of greater than a factor of two can be expected.

6.6 Conclusion

It has been shown that a selection of neutrino-electron elastic scattering events can be successfully carried out using the P0D. A purity and efficiency of 52.8% and 25.2% respectively give a total of 100 signal events expected in a data set of 190 events using the projected official final POT. As it uses an interaction with a precisely known cross-section, this analysis is an attractive candidate to constrain the large

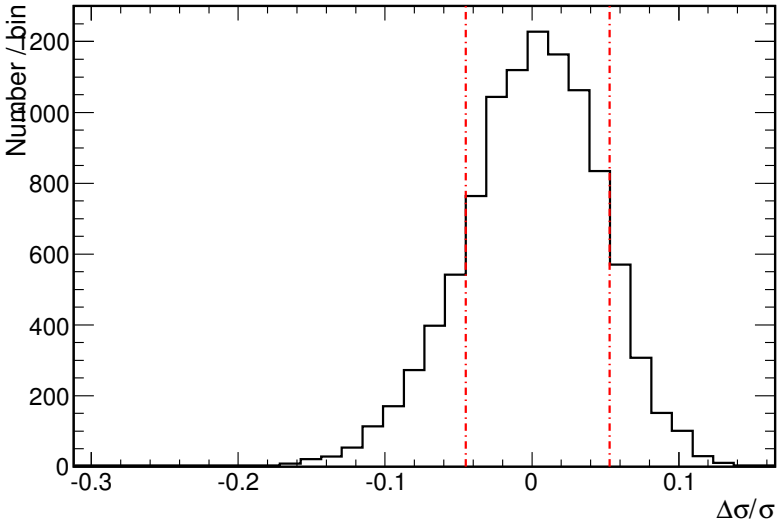

Figure 6.12: Distribution of fractional change in $\bar{\nu}_\mu$ inclusive CC cross-section after flux variation within the errors constrained using the fitter detailed in Section 6.5. The widths are found to be +5.3%, −4.5%.

flux systematic uncertainty involved in other ND280 measurements.

The uncertainty on the total flux using this method is estimated to be approximately 13.5%. Due to the flux component correlations, a fit to the number of observed events can also constrain the flux components individually. A fitter has been constructed and has been shown to perform with no biases. The fit indicates that at the end of T2K data-taking, the $\bar{\nu}_\mu$ flux uncertainty may be reduced from 11.8% to 6.1%. The $\bar{\nu}_\mu$ cross-section measurement documented in Chapter 5 is dominated by a flux systematic uncertainty of 12.4%. Propagating the expected future flux uncertainty of 6.1% through the calculation of that measurement, it has been shown that this could be reduced from 12.4% to 5.8% using the method described here.

Chapter 7

Conclusion

With the discovery of neutrino oscillations and the possibility that $\mathcal{CP}$ violation in the lepton sector can account for the baryon asymmetry observed in the universe, precise knowledge of neutrino interaction cross-sections on nuclear targets has been critical. However, currently the data is still sparse. The work presented in this thesis makes a significant contribution to broadening this knowledge.

A flux-integrated muon antineutrino charged-current inclusive cross-section measurement per nucleon using the carbon target of the ND280 FGD1 was presented. The analysis concluded with a result of:

$$\langle \sigma_{\bar{\nu}_\mu} \rangle_\Phi = (2.72 \pm 0.03(\text{stat.})^{+0.28}_{-0.34}(\text{flux}) \pm 0.14(\text{int.}) \pm 0.14(\text{det.})) \times 10^{-39} \frac{\text{cm}^2}{\text{nucleon}}$$

at a mean muon antineutrino energy of 1 GeV.

It was shown in Figure 5.22 that this is the first measurement spanning this energy.

The uncertainty on the measurement is dominated by those associated with the neutrino flux. A possible method of improving the flux uncertainty was investigated. The feasibility study indicated that at the end of the expected T2K data-taking period, the uncertainty can be reduced from 12.4% to 5.8%.

T2K will continue to provide useful measurements in this area for the neutrino physics community in the future. The polarity of the experiment's magnetic horns has recently been reversed, enabling a far greater sample of muon antineutrino interactions to be recorded. A future antineutrino analysis will therefore contain enough statistics to measure an inclusive energy-dependent differential cross-section,

an even more useful measurement for neutrino interaction generators, aiding the next generation of analyses.

A CCQE enhanced analysis will also be possible by T2K in the future. This 'golden channel' will be most directly useful for the study of $\mathcal{CP}$ violation. Additionally, it is expected that nucleon-nucleon correlations, mentioned in Section 2.5.2, affect neutrino and antineutrino CCQE interactions differently [65]. This is an area of neutrino physics that is not yet fully understood. As $\mathcal{CP}$ violation studies require comparison of neutrino and antineutrino behaviour, a good understanding of differences between the two cross-sections arising independently of $\mathcal{CP}$ violating effects is a crucial step in studying the possibility of this phenomenon in the lepton sector. This is something that, among other experiments, T2K can make important contributions to in the future.

Appendix A

Investigation of method of cross-section extraction

A.1

An interaction cross-section is a measure of the probability of interaction of an incoming particle with a target, defined as follows:

$$\sigma_{true} \equiv \frac{N}{\phi T}, \tag{A.1}$$

where N is the number of signal interactions in the target material, ϕ is the flux, the rate of incoming particles per unit area, and T is the number of target nucleons for which the interaction can occur.

In practice, the flux from a neutrino beam is a function of energy. In this analysis, the total number of interactions across the whole incoming neutrino energy spectrum is included, giving a flux-integrated cross-section.

Particle physics experiments select a number of events with a certain efficiency. In practice, only a subset of these events will be from the interaction being studied. Therefore, the number of signal events that occurred in the target, N, must be inferred from the number observed, corrected for by the simulation of the experiment; from now on this will be denoted by N^{inf}. There are multiple ways of using the simulation for this correction.

The effect of systematic uncertainties on both the final uncertainty and bias on the cross-section calculated will differ between methods; which to use is dependent upon the relative magnitude of the component errors. In this appendix, two methods are studied in order to find the most appropriate for the analysis presented in Chapter 5: the background subtraction method and the purity correction method.

The background subtraction method uses only the selected background in the simulation explicitly:[1]

$$N_{\text{bkg}}^{\text{inf}} \equiv \frac{N^{\text{obs,data}} - N^{\text{bkg,MC}}}{\epsilon}, \tag{A.2}$$

where $N^{\text{obs,data}}$ is the number of observed events in the real data, $N^{\text{bkg,MC}}$ is the number of background events selected in simulation, normalised to the data POT, and ϵ is the predicted efficiency of signal selection from the simulation, defined in Equation (5.1).

On the other hand, the purity correction method retains the simulation of the signal in the calculation, by using the predicted purity, π, as defined in Equation (5.1):

$$N_{\text{pur}}^{\text{inf}} \equiv \frac{N^{\text{obs,data}}\pi}{\epsilon}. \tag{A.3}$$

In general, the background subtraction method is preferred as it does not depend explicitly on the model for the signal. However, in order to be justified in using this method, the absolute normalisation of the background must be trusted to a high degree; the best way to achieve this would be to produce sideband samples of all selected backgrounds (or at least the significant ones). The purity correction method should be considered if the background is not well understood and no such sidebands can be found, especially if the systematic errors are highly correlated between signal and background. A combination of the two can also be used, as in the MiniBooNE neutral-current elastic differential cross-section calculation [124], where sideband analyses were used to subtract out the beam unrelated and dirt backgrounds prior to performing a purity correction. The bias these methods can create in a cross-section calculation requires a preliminary study of the systematic

[1] The signal also appears, but only as a ratio of selected to initial in the efficiency.

errors involved in the particular analysis.

To illustrate how these methods can bias the cross-section calculation through the inferred number of events, a study has been conducted in which the extracted number of selected signal events is plotted as a function of the actual number of signal events selected in data, and for various values of actual background events selected in data.[2] The extracted number of signal events is defined by the numerator of Equations (A.2) and (A.3); this study neglects the efficiency of selection as it appears in both methods and by doing this, a perfect method will result in the function following exactly the line $y = x$, where the extracted number of signal events is always equal to the actual number of signal events selected in data. The predicted purity of the hypothetical selection in these plots is taken to be 50%, which is approximately equal to that achieved in the analysis presented in Chapter 5, and the selection contains 200 signal and 200 background events.

In these plots the black line shows the extracted signal given by the background subtraction method, the red line that from the purity correction, and the simulation predicted signal of 200 events is highlighted with a dashed line. In addition, the line $y = x$ is plotted.

In Figure A.1(a), the actual background selected is equal to the predicted background. As expected, by using background subtraction, the extracted signal always exactly follows the actual signal. However, using the purity correction, the extracted signal is biased towards the predicted signal. Indeed, if no signal events are in fact selected, this method still returns a value of 100.

However, in practice a real particle physics experiment may have significant uncertainties in background estimates. In Figure A.1(b), the actual background is half that predicted from the simulation. In this scenario, the background subtraction method has a constant bias away from the actual signal and is outperformed by the purity correction method for all values of actual signal up to the point where the actual signal is 1.5 times the expected value.

In Figure A.1(c), the actual background is instead twice that predicted. In this case the background subtraction method is outperformed for most likely values of actual signal selected, and will only perform better if the actual signal is four times that predicted (not shown on plot).

[2]To be clear, the sum of the actual signal and actual background events selected in data give the observed number of events from Equations (A.2) and (A.3), $N^{\text{obs,data}}$.

The above study has given indications as to when each method is the appropriate one to use. If the background events in the selection can be predicted with high precision, then the background subtraction method should be used. However, if this is not the case, but the systematic uncertainties on the signal and background are highly correlated, such that an upwards deviation in selected signal is accompanied by a similar deviation in background (leaving aside statistical fluctuations), then the purity correction method should be used.

Of course, any real analysis will not be so clear-cut, and in order to evaluate the best method to use in a particular analysis, it is not sufficient to simply scan the whole range of possible selected signal and background events; instead the likelihood that a particular number of signal or background events is selected must be taken into account. This distribution of likely numbers is clearly dependent on the systematic uncertainties affecting the selection, and can in general be (anti-)correlated to a greater or lesser extent between signal and background.

In this study, 1000 possible experiment scenarios are thrown with differing numbers of selected signal and background (i.e. different $N^{obs,data}$). These numbers are obtained by applying the flux and cross-section weights[3] (see Sections 5.4.1 and 5.4.2) to the nominal simulation events in the same way as is done in the systematic uncertainty evaluation, which is our best estimate of the likely variation in selected signal and background. This distribution is shown in Figure A.2. It can be seen that the correlation from the systematic uncertainties is then taken into account.

For the actual systematic uncertainty evaluation the nominal number of events selected in simulation is used for $N^{obs,data}$. In this investigation, on the other hand, 1000 possible experiment scenarios where $N^{obs,data}$ is given differing values are considered. The method of evaluating the actual systematic uncertainty is then repeated 1000 times for each of the 1000 experimental scenarios. That is, the simulation numbers ϵ, $\pi/N^{bkg,MC}$, and in the case of the flux uncertainty, ϕ, are varied and the effect on the cross-section is plotted. For each of the 1000 fractional change in cross-section distributions for each method, the mean value is taken; this is a measure of the most likely offset from the real cross-section. These means are then plotted to form a distribution of the biases that occur in 1000 likely experiment scenarios. This distribution for both the purity correction and the background subtraction method are shown in Figure A.3. It can be seen that there is both a smaller spread, and less offset (meaning a smaller likely bias) when using the purity correction method.

[3]Detector systematic uncertainties are not accounted for in this study

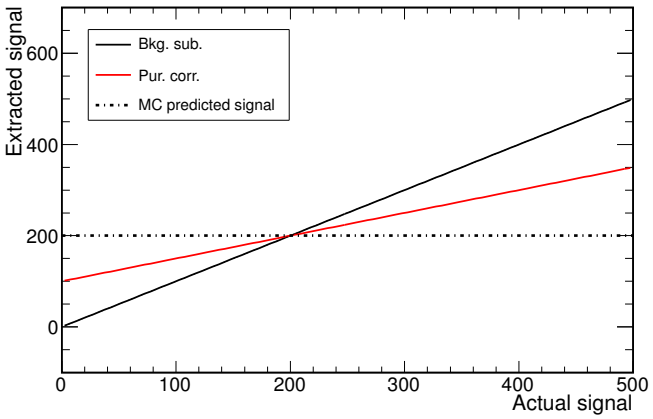

(a) Actual background = Predicted background

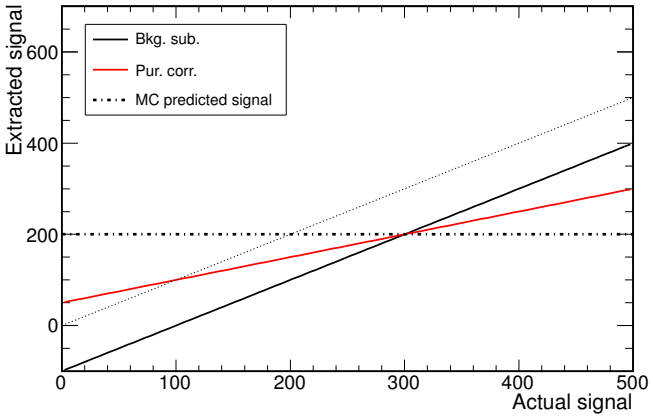

(b) Actual background = Half predicted background

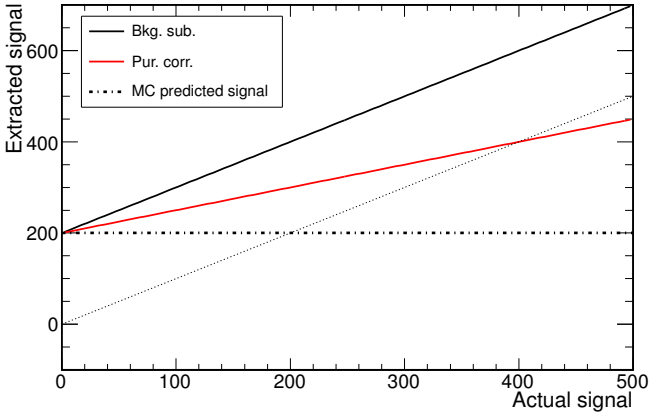

(c) Actual background = Twice predicted background

Figure A.1: The extracted number of selected signal events as a function of the actual number of signal events selected in data, and for various values of actual background events selected in data.

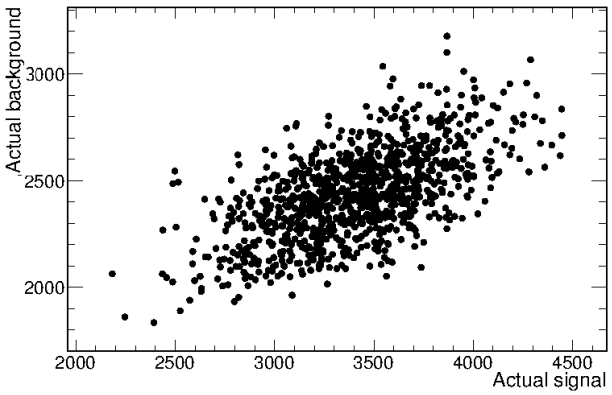

Figure A.2: Selected signal and background for 1000 experiment scenarios. The correlation between the two is dictated by varying these based on the flux covariance matrix.

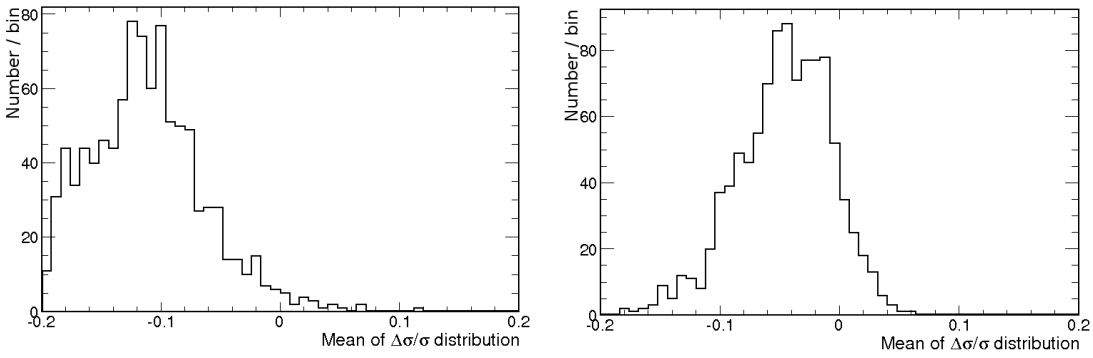

Figure A.3: Distribution of the means of 1000 fractional change in cross-section distributions for (left) background subtraction, and (right) purity correction.

Bibliography

[1] G. Aad et al. Observation of a new particle in the search for the Standard Model Higgs boson with the ATLAS detector at the LHC. *Phys. Lett.*, B716: 1–29, 2012.

[2] S. Chatrchyan et al. Observation of a new boson at a mass of 125 GeV with the CMS experiment at the LHC. *Phys. Lett.*, B716:30–61, 2012.

[3] Source: AAAS. Popular physics theory running out of hiding places. `http://www.bbc.co.uk/news/science-environment-20300100`.

[4] F. Close. Neutrino, Chapter 1. Oxford University Press, 2010.

[5] D. Griffiths. Introduction to Elementary Particles, Chapters 1, 6 & 9. Wiley and Sons, Moerlen-bach, Germany, 1987.

[6] H. Bethe and R. Peierls. The Neutrino. *Nature*, 133(532), 1934.

[7] F. Reines, C. L. Cowan, F. B. Harrison, A. D. McGuire, and H. W. Kruse. Detection of the Free Antineutrino. *Phys. Rev.*, 117:159–173, 1960.

[8] G. Danby et al. Observation of High-Energy Neutrino Reactions and the Existence of Two Kinds of Neutrinos. *Phys. Rev. Lett.*, 9:36–44, 1962.

[9] M. Perl et al. Evidence for Anomalous Lepton Production in $e^+ - e^-$ Annihilation. *Phys. Rev. Lett.*, 35:1489–1492, 1975.

[10] K. Kodama et al. Observation of tau neutrino interactions. *Phys. Lett.*, B504: 218–224, 2001.

[11] A. Chavarria. Solar Neutrinos in 2011. 2012. arXiv:1201.6311 [astro-ph.SR].

[12] J. N. Bahcall, W. A. Fowler, Jr. Iben, I., and R. L. Sears. Solar neutrino flux. *Astrophys. J.*, 137:344–346, 1963.

[13] B. T. Cleveland et al. Measurement of the solar electron neutrino flux with the Homestake chlorine detector. *The Astrophysical Journal*, 496(1):505, 1998.

[14] K. Hirata et al. Observation of ^{8}B solar neutrinos in the Kamiokande-II detector. *Phys. Rev. Lett.*, 63:16–19, Jul 1989.

[15] Q. R. Ahmad et al. Direct evidence for neutrino flavor transformation from neutral current interactions in the Sudbury Neutrino Observatory. *Phys. Rev. Lett.*, 89:011301, 2002.

[16] K. S. Hirata et al. Experimental Study of the Atmospheric Neutrino Flux. *Phys. Lett.*, B205:416, 1988.

[17] D. Casper et al. Measurement of atmospheric neutrino composition with the IMB-3 detector. *Phys. Rev. Lett.*, 66:2561–2564, May 1991.

[18] W. W. M. Allison et al. Measurement of the atmospheric neutrino flavor composition in Soudan-2. *Phys. Lett.*, B391:491–500, 1997.

[19] Y. Fukuda et al. Study of the atmospheric neutrino flux in the multi-GeV energy range. *Phys. Lett.*, B436:33–41, 1998.

[20] Atmospheric neutrinos. `http://hep.bu.edu/superk/atmnu/`, .

[21] B. Kayser. On the quantum mechanics of neutrino oscillation. *Phys. Rev.*, D24:110–116, 1981.

[22] S.P. Mikheyev and A.Yu. Smirnov. Resonant amplification of ν oscillations in matter and solar-neutrino spectroscopy. *Il Nuovo Cimento*, C9(1):17–26, 1986.

[23] L. Wolfenstein. Neutrino Oscillations in Matter. *Phys. Rev.*, D17:2369–2374, 1978.

[24] L. H. Whitehead. A Measurement of the Electron Neutrino Component of the T2K Beam using the Near Detector. Ph.D. Thesis, University of Warwick, UK, 2012.

[25] Boris Kayser. Neutrino Oscillation Phenomenology. 2008. arXiv:0804.1121 [hep-ph].

[26] F. Capozzi et al. Status of three-neutrino oscillation parameters, circa 2013. *Phys. Rev.*, D89:093018, 2014.

[27] M. C. Gonzalez-Garcia, M. Maltoni, J. Salvado, and T. Schwetz. Global fit

to three neutrino mixing: critical look at present precision. *JHEP*, 1212:123, 2012.

[28] D. V. Forero, M. Tortola, and J. W. F. Valle. Global status of neutrino oscillation parameters after Neutrino-2012. *Phys. Rev.*, D86:073012, 2012.

[29] J. Cao. Daya Bay neutrino experiment. *Nucl. Phys. Proc. Suppl.*, 155:229–230, 2006.

[30] F. P. An et al. Improved Measurement of Electron Antineutrino Disappearance at Daya Bay. *Chin. Phys.*, C37:011001, 2013.

[31] Y. Abe et al. Reactor electron antineutrino disappearance in the Double Chooz experiment. *Phys. Rev.*, D86:052008, 2012.

[32] J. Ahn et al. Observation of Reactor Electron Antineutrinos Disappearance in the RENO Experiment. *Phys. Rev. Lett.*, 108:191802, 2012.

[33] P. Adamson et al. Electron neutrino and antineutrino appearance in the full MINOS data sample. *Phys. Rev. Lett.*, 110(17):171801, 2013.

[34] K. Abe et al. The T2K experiment. *Nuclear Instruments and Methods in Physics Research*, A659:106–135, 2011.

[35] K. Abe et al. Observation of Electron Neutrino Appearance in a Muon Neutrino Beam. *Phys. Rev. Lett.*, 112:061802, 2014.

[36] A. D. Sakharov. Violation of CP Invariance, C Asymmetry, and Baryon Asymmetry of the Universe. *Soviet Journal of Experimental and Theoretical Physics Letters*, 5:24, 1967.

[37] M. Trodden. Baryogenesis and leptogenesis. *eConf*, C040802:L018, 2004.

[38] P. Di Bari. An introduction to leptogenesis and neutrino properties. *Contemp. Phys.*, 53(4):315–338, 2012.

[39] S. F. King and C. Luhn. Neutrino Mass and Mixing with Discrete Symmetry. *Rept. Prog. Phys.*, 76:056201, 2013.

[40] G. J. Barker et al. The Future of Neutrino Mass Measurements: Terrestrial, Astrophysical, and Cosmological Measurements in the Next Decade. Highlights of the NuMass 2013 Workshop. Milano, Italy, February 4–7, 2013.

[41] J. Bonn et al. The Mainz neutrino mass experiment. *Nuclear Physics B - Proceedings Supplements*, 91(1-3):273–279, 2001. URL

http://www.sciencedirect.com/science/article/pii/S0920563200009518. Neutrino 2000.

[42] V. N. Aseev et al. An upper limit on electron antineutrino mass from Troitsk experiment. *Phys. Rev.*, D84:112003, 2011.

[43] J. Wolf. The KATRIN neutrino mass experiment. *Nuclear Instruments and Methods in Physics Research Section A: Accelerators, Spectrometers, Detectors and Associated Equipment*, 623(1):442–444, 2010. 1st International Conference on Technology and Instrumentation in Particle Physics.

[44] III Avignone, F. T., S. R. Elliott, and J. Engel. Double Beta Decay, Majorana Neutrinos, and Neutrino Mass. *Rev. Mod. Phys.*, 80:481–516, 2008.

[45] E. Majorana and L. Maiani. A symmetric theory of electrons and positrons. In GiuseppeFranco Bassani, editor, *Ettore Majorana Scientific Papers*, pages 201–233. Springer Berlin Heidelberg, 2006. ISBN 978-3-540-48091-4.

[46] M. Agostini et al. Results on Neutrinoless Double-β Decay of ^{76}Ge from Phase I of the GERDA Experiment. *Phys. Rev. Lett.*, 111:122503, Sep 2013.

[47] J.J. Gomez-Cadenas, J. Martin-Albo, J. Munoz Vidal, and C. Pena-Garay. Discovery potential of xenon-based neutrinoless double beta decay experiments in light of small angular scale CMB observations. *JCAP*, 1303:043, 2013.

[48] J.B. Albert et al. Search for Majorana neutrinos with the first two years of EXO-200 data. *Nature*, 510:229–234, 2014.

[49] S. Schael et al. Precision electroweak measurements on the Z resonance. *Phys. Rept.*, 427:257–454, 2006.

[50] P. A. R. Ade et al. Planck 2013 results. XVI. Cosmological parameters. 2013. arxiv:1303.5076 [astro-ph.CO].

[51] A. Aguilar-Arevalo et al. Evidence for neutrino oscillations from the observation of anti-neutrino(electron) appearance in a anti-neutrino(muon) beam. *Phys. Rev.*, D64:112007, 2001.

[52] C. Athanassopoulos et al. Evidence for muon-neutrino to electron-neutrino oscillations from pion decay in flight neutrinos. *Phys. Rev.*, C58:2489–2511, 1998.

[53] K. N. Abazajian et al. Light Sterile Neutrinos: A White Paper. 2012. arXiv:1204.5379 [hep-ph].

[54] C. Giunti and M. Laveder. Statistical Significance of the Gallium Anomaly. *Phys. Rev.*, C83:065504, 2011.

[55] R. B. Patterson. The NOνA Experiment: Status and Outlook. *Nucl. Phys. Proc. Suppl.*, 235-236:151–157, 2013.

[56] Messier, M. for the NOνA collaboration. Extending the NOνA Physics Program. 2013. URL `http://if-neutrino.fnal.gov/whitepapers/messier-nova.pdf`.

[57] S. K. Agarwalla, S. Prakash, S. K. Raut, and S. U. Sankar. Potential of optimized NOνA for large $\theta(13)$ and combined performance with a LArTPC and T2K. *JHEP*, 1212:075, 2012.

[58] G. Tzanankos et al. MINOS+: a Proposal to FNAL to run MINOS with the medium energy NuMI beam. 2011. URL `http://lss.fnal.gov/archive/test-proposal/1000/fermilab-proposal-1016.shtml`.

[59] J. Evans. The MINOS experiment: results and prospects. *Adv. High Energy Phys.*, 2013:182537, 2013.

[60] K. Abe et al. Letter of Intent: The Hyper-Kamiokande Experiment — Detector Design and Physics Potential —. 2011. arXiv:1109.3262 [hep-ex].

[61] C. Adams et al. The Long-Baseline Neutrino Experiment: Exploring Fundamental Symmetries of the Universe. 2013. arXiv:1307.7335 [hep-ex].

[62] T. Lee and C. Yang. Question of Parity Conservation in Weak Interactions. *Phys. Rev.*, 104:254–258, Oct 1956.

[63] C. Wu et al. Experimental Test of Parity Conservation in Beta Decay. *Phys. Rev.*, 105:1413–1415, Feb 1957.

[64] J. Beringer et al. Review of Particle Physics. *Phys. Rev.*, D86:010001, 2012.

[65] J. A. Formaggio and G. P. Zeller. From eV to EeV: Neutrino Cross Sections Across Energy Scales. *Rev. Mod. Phys.*, 84:1307, 2012.

[66] J. L. Hewett et al. Fundamental Physics at the Intensity Frontier. 2012. arXiv:1205.2671 [hep-ex].

[67] C. H. Llewellyn Smith. Neutrino Reactions at Accelerator Energies. *Phys. Rept.*, 3:261–379, 1972.

[68] A. Bodek, S. Avvakumov, R. Bradford, and H. S. Budd. Extraction of the axial nucleon form-factor from neutrino experiments on deuterium. *J. Phys. Conf. Ser.*, 110:082004, 2008.

[69] Laura Fields. Neutrino Cross Sections. pages 190–198, 2012. arXiv:1212.0060 [hep-ex], 32nd International Symposium on Physics in Collision (PIC 2012).

[70] Y. Hayato. Neut. *Nuclear Physics B - Proceedings Supplements*, 112(1-3):171–176, 2002. URL `http://www.sciencedirect.com/science/article/pii/S0920563202017590`.

[71] Private communication with A. Furmanski of the University of Warwick. 2013.

[72] H. Nakamura, M. Sakuda, T. Nasu, and O. Benhar. Inclusive electron spectrum in the region of pion production in electron-nucleus scattering and the effect of the quasi-elastic interaction. *Phys. Rev.*, C76:065208, 2007.

[73] A. M. Ankowski and J. T. Sobczyk. Construction of spectral functions for medium-mass nuclei. *Phys. Rev.*, C77:044311, 2008.

[74] R. Acciarri et al. Measurements of Inclusive Muon Neutrino and Antineutrino Charged Current Differential Cross Sections on Argon in the NuMI Antineutrino Beam. *Phys. Rev.*, D89:112003, 2014.

[75] IHEP. `http://www.ihep.ac.cn/kejiyuandi/zhishi/050225-sanlie/sanlie-index.htm`.

[76] V. Galymov. Neutrino flux predictions for the T2K long baseline neutrino oscillation experiment. Ph.D. Thesis, York University, Toronto, Ontario, 2012.

[77] D. Scully. Neutrino Induced Coherent Pion Production. Ph.D. Thesis, University of Warwick, UK, 2013.

[78] N. Abgrall et al. Neutrino flux prediction for the 2010a analysis. T2K-TN-038. URL `http://www.t2k.org/docs/technotes/038`.

[79] K. Abe et al. T2K neutrino flux prediction. *Phys. Rev.*, D87(1):012001, 2013.

[80] T2K official plots. `http://www.t2k.org/docs/plots/`, .

[81] P. A. Amaudruz et al. The T2K fine-grained detectors. *Nuclear Instruments and Methods in Physics Research A*, 696:1–31, December 2012.

[82] D. Allan et al. The Electromagnetic Calorimeter for the T2K Near Detector ND280. *JINST*, 8:P10019, 2013.

[83] T2K photographs. `http://www.t2k.org/docs/photos/nd280/`.

[84] K. Abe et al. Indication of Electron Neutrino Appearance from an Accelerator-produced Off-axis Muon Neutrino Beam. *Phys. Rev. Lett.*, 107:041801, 2011.

[85] A. Carver. Electron identification in and performance of the ND280 Electromagnetic Calorimeter. Ph.D. Thesis, University of Warwick, UK, 2010.

[86] L. Durieu, M. Martini, and A. S. Muller. Optics studies for the T9 beam line in the CERN PS East Area secondary beam facility. In *Particle Accelerator Conference, 2001. PAC 2001. Proceedings of the 2001*, volume 2, pages 1547–1549 vol.2, 2001.

[87] L. Landau. On the energy loss of fast particles by ionization. *J. Phys.(USSR)*, 8:201–205, 1944.

[88] The T2K ND280 UK/ECAL Group. T2K 2010a Analysis ND280 DsECAL Status Report. T2K-TN-018. URL `http://www.t2k.org/docs/technotes/018`.

[89] S. Agostinelli et al. GEANT4: A simulation toolkit. *Nucl. Instrum. Meth.*, A506:250–303, 2003.

[90] C. Cerri et al. Testbeam area and detector magnet. Technical report. URL `http://www.hep.princeton.edu/~mcdonald/nufact/uL@CERN.pdf`.

[91] The T2K beam group. Neutrino flux release. `http://www.t2k.org/beam/NuFlux/FluxRelease`.

[92] Kowalik, K. and Lagoda, J. The simulation of beam neutrino interactions outside the ND280 detector. T2K-TN-077. URL `http://www.t2k.org/docs/technotes/077`.

[93] The ND280 ν_μ group. CCQE-like and CC-non-QE-like ν_μ event selections in the ND280 tracker using Run 1+2 data. T2K-TN-093. URL `http://www.t2k.org/docs/technotes/093`.

[94] Hadley, D. and the T2K Warwick group. Second Generation Particle ID with the ND280 Tracker ECALs. T2K-TN-111. URL `http://www.t2k.org/docs/technotes/111`.

[95] Abgrall, N. and others. Flux inputs for the 2012a oscillation analysis. T2K-TN-099. URL http://www.t2k.org/docs/technotes/099.

[96] P. de Perio et al. Implementation of the NIWG cross section parameterisation. T2K-TN-113. URL http://www.t2k.org/docs/technotes/113.

[97] K. Abe et al. Measurement of the inclusive ν_μ charged current cross section on carbon in the near detector of the T2K experiment. *Phys. Rev.*, D87(9): 092003, 2013.

[98] de Perio, P. and others. Cross section parameters for the 2012a oscillation analysis. T2K-TN-108. URL http://www.t2k.org/docs/technotes/108.

[99] The ND280 ν_μ group. CC-multiple-pion ν_μ event selections in the ND280 tracker using Run 1+2+3+4 data. T2K-TN-152. URL http://www.t2k.org/docs/technotes/152.

[100] The ND280 ν_e group. Charge misidentification in local and global reconstruction. T2K-TN-048. URL http://www.t2k.org/docs/technotes/048.

[101] Dufour, F. and Lindner, T. and Oser, S. Systematics on Out-of-Fiducial-Volume Backgrounds in the ND280 Tracker. T2K-TN-098. URL http://www.t2k.org/docs/technotes/098.

[102] Smith, B. ECal Systematics. T2K Barcelona Workshop Presentation (2013). URL http://www.t2k.org/nd280/physics/nu-mu/meetings/2013/barcaapril2013/talks/Frid5th/ecalsystematics/view.

[103] The ND280 ν_e group. Measurement of the electron neutrino beam component in the ND280 tracker for 2013 analyses. T2K-TN-149. URL http://www.t2k.org/docs/technotes/149.

[104] Myslik, J. Determination of pion secondary interaction systematics for the ND280 tracker ν_μ analysis. T2K-TN-125. URL http://www.t2k.org/docs/technotes/125.

[105] Salzgeber, M. Ravonel. Measurement of the flux averaged muon neutrino inclusive charged current cross-section at the near detector. T2K-TN-117. URL http://www.t2k.org/docs/technotes/117.

[106] S. Murphy. The NA61/SHINE hadron production measurements for T2K: Update and recent results. *J. Phys. Conf. Ser.*, 375:042071, 2012.

[107] Park, J. Neutrino-Electron Scattering in MINERνA for Constraining the NuMI Neutrino Flux. MinerνA Technical Note No. 41.

[108] S. Mandelstam. Determination of the pion - nucleon scattering amplitude from dispersion relations and unitarity. General theory. *Phys. Rev.*, 112:1344–1360, 1958.

[109] J. Peltoniemi. Cross sections. `http://cupp.oulu.fi/neutrino/nd-cross.html`.

[110] C. Andreopoulos et al. The GENIE Neutrino Monte Carlo Generator. *Nucl. Instrum. Meth.*, A614:87–104, 2010.

[111] K. Gilje. P0D Geometry and Mass. T2K-TN-073. URL `http://www.t2k.org/docs/technotes/073`.

[112] Jo, J. P0D NuE Analysis: Systematics/Reconstruction Study. Work presented to T2K ND280 NuE group (2013).

[113] Jo, J. and others. Measurement of the CCν_e interaction rate on water with the P0D. T2K-TN-150. URL `http://www.t2k.org/docs/technotes/150`.

[114] B. P. Roe et al. Boosted decision trees, an alternative to artificial neural networks. *Nucl. Instrum. Meth.*, A543:577–584, 2005.

[115] A. Hoecker et al. TMVA - Toolkit for Multivariate Data Analysis. 2007. arXiv:physics/0703039 [physics.data-an].

[116] Y. Freund. Experiments with a new boosting algorithm. *Proc. ICML-1996*, 1996. URL `http://ci.nii.ac.jp/naid/10008654485/en/`.

[117] The T2K Collaboration. Physics Potential and Sensitivities of T2K. Report to J-PARC PAC. URL `http://http://www.t2k.org/comm/ec/pacreport2013`.

[118] C. Andreopoulis et al. A GENIE-based Event Generation Driver for T2K and MDC0-era Issues. T2K-TN-006. URL `http://www.t2k.org/docs/technotes/006`.

[119] Ruterbories, D. Measurement of NCE Production with the T2K Pi0 detector (P0D). T2K-TN-131. URL `http://www.t2k.org/docs/technotes/131`.

[120] Gilje, K. Track PID efficiency in the π^0 detector in the ND280 basket. T2K-TN-200. URL `http://www.t2k.org/docs/technotes/200`.

[121] Andreopoulis, C. and others. Neutrino Generator (GENIE) Uncertainties and

2010a ν_μ-Disappearance / ν_e-Appearance Oscillation Analysis Systematics. T2K-TN-035. URL `http://www.t2k.org/docs/technotes/035`.

[122] G. A. Fiorentini et al. Measurement of Muon Neutrino Quasielastic Scattering on a Hydrocarbon Target at $E_\nu \sim 3.5\,\mathrm{GeV}$. *Phys. Rev. Lett.*, 111(2):022502, 2013.

[123] Clifton, A. and others. Analysis of ν_μ charged current inclusive events in the P0D in run 1+2. T2K-TN-080. URL `http://www.t2k.org/docs/technotes/080`.

[124] A. A. Aguilar-Arevalo et al. Measurement of the Neutrino Neutral-Current Elastic Differential Cross Section on Mineral Oil at $E_\nu \sim 1$ GeV. *Phys. Rev.*, D82:092005, 2010.